POLISH ACADEMY OF SCIENCE
COMMITTEE FOR ELECTRONICS AND TELECOMMUNICATIONS

ELECTRONICS AND TELECOMMUNICATIONS QUARTERLY

KWARTALNIK ELEKTRONIKI I TELEKOMUNIKACJI

VOLUME 55 – No 4

WARSAW 2009

ELECTRONICS AND TELECOMMUNICATIONS QUARTERLY
Quarterly of Polish Academy of Sciences

INTERNATIONAL PROGRAMME COMMITTEE

Marek AMANOWICZ
Military University of Technology, Poland

Daniel J. BEM
Wroclaw University of Technology, Poland

Franco DAVOLI
University of Genowa, Italy

Gilbert DE MEY
Ghent University, Belgium

Stefan HAHN
Warsaw University of Technology, Poland

Włodzimierz JANKE
Koszalin University of Technology, Poland

Viktor KROZER
Technical University of Denmark, Denmark

Andrzej MATERKA
Technical University of Łódź, Poland

Józef MODELSKI
Warsaw University of Technology, Poland

Adam MORAWIEC
European Electronic Chips & Systems Design Initiative, Gieres, France

Antoni ROGALSKI
Military University of Technology, Poland

Herman ROHLING
Technical University of Hamburg, Germany

Ryszard ROMANIUK
Warsaw University of Technology, Poland

Henry SELVARAJ
University of Nevada, Las Vegas NV, USA

Radomir S. STANKOVIĆ
University of Niš, Serbia

Wojciech SZPANKOWSKI
Purdue University, USA

Marek TŁACZAŁA
Wroclaw University of Technology, Poland

Marek TUROWSKI
CFD Research Corporation, USA

Wiesław WOLIŃSKI
Warsaw University of Technology, Poland

Svetlana YANUSHKEVICH
University of Calgary, Canada

Jacek M. ŻURADA
University of Louisville, Louisville KY, USA

EDITOR-IN-CHIEF

Tadeusz ŁUBA
Warsaw University of Technology, Poland
luba@tele.pw.edu.pl
tel. +48 22 234 7330

TOPICAL EDITORS

Marek DOMAŃSKI
Poznań University of Technology, Poland
domanski@et.put.poznan.pl

Michał MROZOWSKI
Gdańsk University of Technology, Poland
mim@pg.gda.pl

Andrzej NAPIERALSKI
Technical University of Łódź, Poland
napier@dmcs.p.lodz.pl

Jan SZMIDT
Warsaw University of Technology, Poland
J.Szmidt@elka.pw.edu.pl

Tadeusz WIĘCKOWSKI
Wrocław University of Technology, Poland
Tadeusz.Wieckowski@pwr.wroc.pl

Tomasz WOLIŃSKI
Warsaw University of Technology, Poland
wolinski@if.pw.edu.pl

Józef WOŹNIAK
Gdańsk University of Technology, Poland
jowoz@eti.pg.gda.pl

TECHNICAL EDITOR

Grzegorz BOROWIK
Warsaw University of Technology, Poland
G.Borowik@tele.pw.edu.pl
tel. +48 22 234 7349; +48 22 234 7330

LANGUAGE VERIFICATION

Janusz KOWALSKI

RESPONSIBLE SECRETARY

Danuta OJRZEŃSKA-WÓJTER
Warsaw University of Technology, Poland
DWojter@tele.pw.edu.pl
tel. +48 22 234 7654; +48 22 234 7330

SECRETARY

Izabela IGNACZAK
Warsaw University of Technology, Poland
tel. +48 22 234 7330

Address of Editorial Office
Nowowiejska Street 15/19, 00-665 Warsaw, Poland
Institute of Telecommunications, room 484, 472

Email: etq@tele.pw.edu.pl
tel. +48 22 234 7330

Ark. Wyd. 12,75 Ark. druk. 10,125	Podpisano do druku w listopadzie 2009 r.
Papier offset, kl. III 80 g. B-1	Druk ukończono w listopadzie 2009 r.

Publishing
Warszawska Drukarnia Naukowa PAN
00-656 Warszawa, ul. Śniadeckich 8
Tel./fax 628-87-77

IMPORTANT MESSAGE FOR THE AUTHORS

The Editorial Board during their meeting on the 18th of January 2006 authorized the Editorial Office to introduce the following changes:

1. **PUBLISHING THE ARTICLES IN ENGLISH LANGUAGE ONLY**

Starting from No 1'2007 of E&T Quarterly, all the articles will be published in English only.

Each article prepared in English must be supplemented with a thorough summary in Polish (e.g. 2 pages), including the essential formulas, tables, diagrams etc. The Polish summary must be written on a separate page. The articles will be reviewed and their English correctness will be verified.

2. **COVERING THE PUBLISHING EXPENSES BY AUTHORS**

Starting from No'2007 of E&T Quarterly, a principle of publishing articles against payment is introduced, assuming non-profit making editorial office. According to the principle the authors or institutions employing them, will have to cover the expenses in amount of 760 PLN for each publishing sheet. The above amount will be used to supplement the limited financial means received from PAS for publishing; particularly to increase the capacity of next E&T Quaterly volumes and verify the English correctness of articles. It is neccessary to increase the capacity of E&T Quarterly volumes due to growing number of received articles, which delays their publishing.

In case of authors written request to accelerate the publishing of an article, the fee will amount to 1500 PLN for each publishing sheet.

In justifiable cases presented in writing, the editorial staff may decide to relieve authors from basic payment, either partially or fully. The payment must be made by bank transfer into account of Warsaw Science Publishers The account number: Bank Zachodni WBK S.A. Warszawa Nr 94 1090 1883 0000 0001 0588 2816 with additional note: "For Electronics and Telecommunications Quarterly".

Editors

Dear Authors,

Electronics and Telecommunications Quarterly continues tradition of the "Rozprawy Elektrotechniczne" quarterly established 53 years ago.

The E&T Quarterly is a periodical of Electronics and Telecommunications Committee of Polish Academy of Science. It is published by Warsaw Science Publishers of PAS. The Quarterly is a scientific periodical where articles presenting the results of original, theoretical, experimental and reviewed works are published. They consider widely recognised aspects of modern electronics, telecommunications, microelectronics, optoelectronics, radioelectronics and medical electronics.

The authors are outstanding scientists, well-known experienced specialists as well as young researchers -- mainly candidates for a doctor's degree.

The articles present original approaches to problems, interesting research results, critical estimation of theories and methods, discuss current state or progress in a given branch of technology and describe development prospects. The manner of writing mathematical parts of articles complies with IEC (International Electronics Commision) and ISO (International Organization of Standardization) standards.

All the articles published in E&T Quarterly are reviewed by known, domestic specialists which ensures that the publications are recognized as author's scientific output. The publishing of research work results completed within the framework of *Ministerstwo Nauki I Szkolnictwa Wyższego* GRANTs meets one of the requirements for those works.

The periodical is distributed among all those who deal with electronics and telecommunications in national scientific centres, as well as in numeral foreign institutions. Moreover it is subscribed by many specialists and libraries.

Each author is entitled to free of charge 20 copies of article, which allows for easier distribution to persons and institutions domestic and abroad, individually chosen by the author. The fact that the articles are published in English makes the quarterly even more accessible.

The articles received are published within half a year if the cooperation between author and the editorial staff is efficient. Instructions for authors concerning the form of publications are included in every volume of the quarterly; they may also be obtained in editorial office.

The articles may be submitted to the editorial office personally or by post; the editorial office address is shown on editorial page in each volume.

Editors

M

R

S.
J.

I.

S.

F.

A
A
P.
R
J.
Y
T

CONTENTS

ELECTRONICS AND TELECOMMUNICATIONS QUARTERLY, 2009, 55, no 4, pp. 549–562

Two-Dimensional Analytical Model for Channel Length Modulation in Lightly-Doped DG FETs

MICHAELA WEIDEMANN*‡, ALEXANDER KLOES* , MIKE SCHWARZ* and BENJAMIN INIGUEZ†

* *University of Applied Sciences Giessen-Friedberg, Giessen, Germany*
†*University Rovira i Virgili, Tarragona, Spain*
‡*e-mail: michaela.weidemann@gmail.com*

Received 2009.09.22
Authorized 2000.11.17

With this paper we publish a possibility to calculate the shortening of the channel in SOI DoubleGate FETs operating in saturation with a 2D analytical solution of Poisson's equation. The model inherently includes 2D effects by solving the differential equation with conformal mapping technique and does not introduce unphysical fitting parameters. Also these fitting parameters have only a minor influence on the model results. We compared our model to numerical data based on TCAD Sentaurus simulations and it is in good agreement with the results.

Keywords: DG, Channel-length-modulation, 2D Poisson, High-field region, Analytical closed form

1. INTRODUCTION

Since standard single gate bulk MOSFET show several short channel effects (SCE) in sub-*45nm* technology development focuses on MultiGate structures. A scale down to the sub-*10nm* range is possible with so called DoubleGate FETs (DG FETs), FinFETs or GateAllAround-FETs (GAA-FETs). The enhanced area of the gates gives more electrostatic control of the channel. Nevertheless, short channel effects (SCE) take still place [1]. Most models for DG FETs use a conventional bulk MOSFET model to include the channel length shortening effect [2], [3]. In this approach we use conformal mapping technique [4] to calculate 2D Poisson's equation in an analytical closed form. This idea was already applied to several problems of DG FETs and MultiGate FETs [5], [6]. Also we published an approach for bulk MOSFETs in [7] and [8].

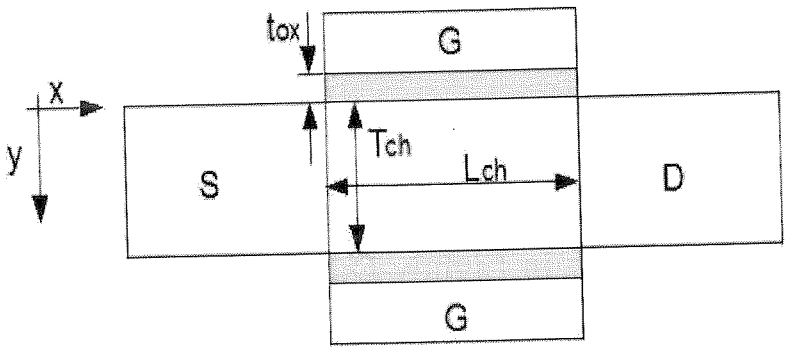

Fig. 1. Simplified structure of a DG FET as used in this approach

In here we solve 2D Poisson in high field saturation region of the device to calculate channel length shortening. For this we use the 4-corner approach by Fjeldly published in [5] and derive a threshold voltage model from this. This V_T model is a simplification of the 3D FinFET model published in [6], whereby the Fin is very high and the influence of the top gate is not present.

A 4-corner structure is more precise, nevertheless due to mathematical reasons very complex. In strong inversion we split the device and only use the high field saturation region to solve 2D Poisson's equation by applying Schwarz-Christoffel method to a 2-corner structure.

For our considerations we use a simplified structure of a DG FET as shown in Fig. 1. The gray parts represent the gate silicon-oxide with the gate on top and bottom. On the left and right are the source and drain region attached. The channel has the thickness T_{ch} and L_{ch}. We assume a gate having no work function difference to the silicon channel, and quantum effects on inversion charge formation are neglected. For simplicity we only focus on a double gate device having the same oxide thickness of 2nm for both top and bottom gates with a fictive permittivity of $\varepsilon_{ox} = 7\ \varepsilon_0$.

2. DEFINITION OF THE SATURATION POINT

Considering the output characteristics of a DG FET still short channel effects (SCE) take place, as shown in Fig. 2. These results were simulated with TCAD Sentaurus FEM simulator [9] for a geometry of $L_{ch} = 50nm$ and $T_{ch} = 10nm$ and without quantum confinement.

After reaching saturation voltage the output characteristics in Fig. 2 show a linear increase, which indicates SCE. Fig. 3 shows the e-current density distribution within the device with an applied $V_{ds} = 1.4V$ and $V_{gs} = 1V$. At source end the channel emerges underneath the gate oxide, as expected. Also the channel becomes smaller, while approaching drain end. On a certain point the charge is not longer located directly underneath the gate, instead it is spread equally over the whole channel. This point we

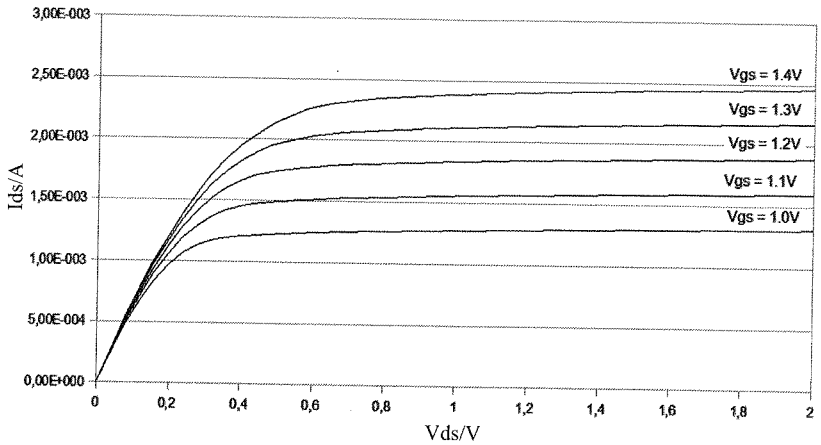

Fig. 2. Drain-Source voltage vs. drain current for a DG FET with L_{ch} = *50nm* and T_{ch} = *10nm*. After reaching saturation voltage, short channel effects can be noticed

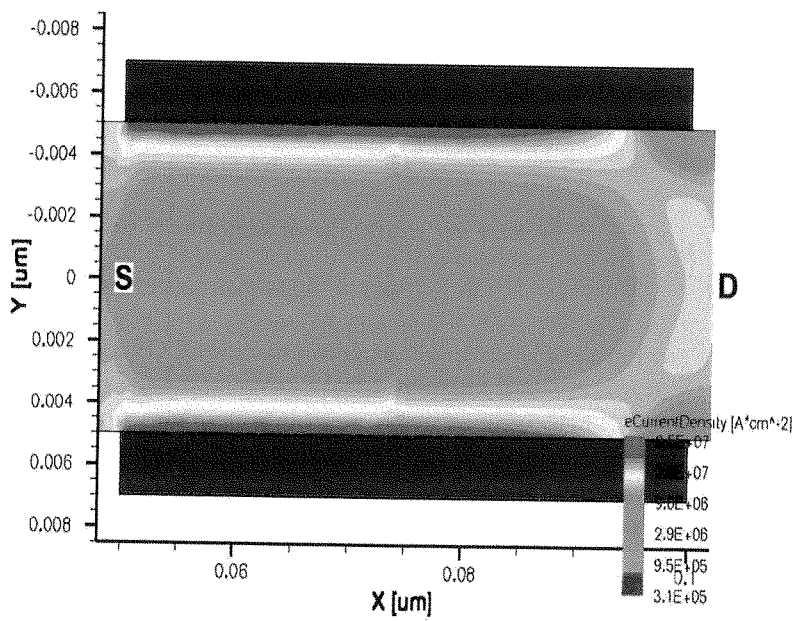

Fig. 3. E-current density distribution within channel region and gate oxide of DG FET with an applied V_{ds} = 1.4*V* and V_{gs} = 1*V*. Drain and source region are cut out as well as the gate material

define at saturation point. Looking at the electric potential distribution in Fig. 4 we see that the contours of the electric potential are straight at saturation point.

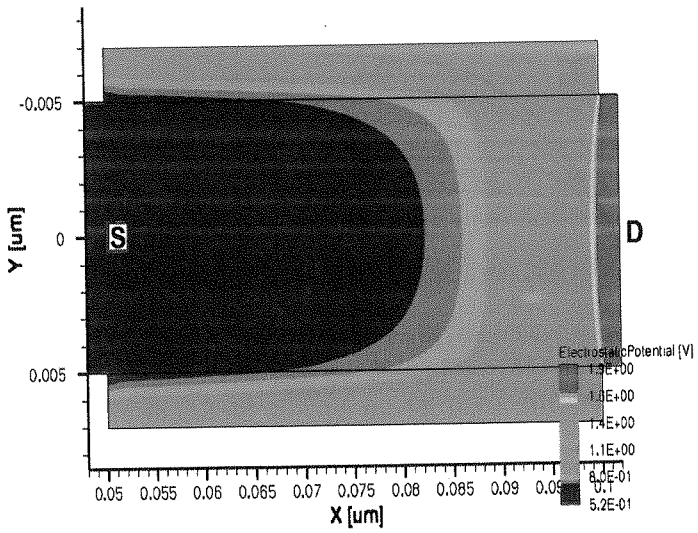

Fig. 4. Electric potential distribution within channel region and gate oxide of DG FET with an applied $V_{ds} = 1.4V$ and $V_{gs} = 1V$. Drain and source region are cut out as well as the gate material

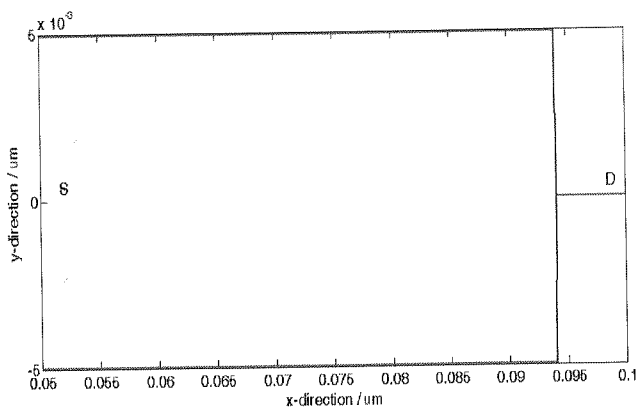

Fig. 5. Path of the electric potential maximum (red line) within cross section of a DG FET operating in saturation mode. Coming from the source end (left side) the maximum is underneath the gate oxide. After reaching the saturation point the electric potential maximum moves suddenly to the middle of the channel

Analyzing the path of the electric potential maximum along the channel (refer to Fig. 5), we see that this electric potential maximum, drawn in red lines, is located underneath both gate oxides at source end. Following the path along the channel with a sudden move the maximum changes location from the gate oxide interfaces into the

middle of the channel. We consider that point as saturation point. After hitting this point the whole channel appears to be in saturation.

3. SOLVING 2D POISSON

Considering a lightly doped device, we have no depletion charge $Q_{dep} \approx 0$. We need to solve Poisson equation in the high field saturation region of the device. From the analyses of the device,

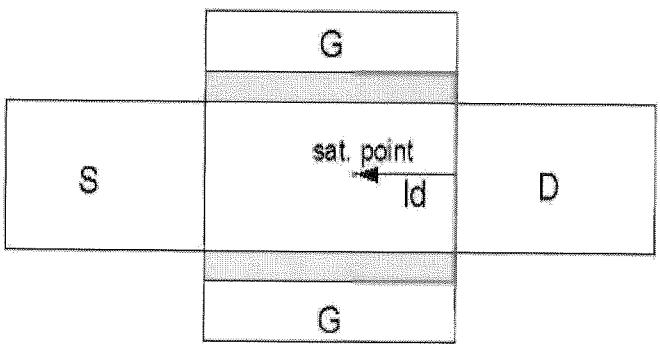

Fig. 6. High field saturation region wherein 2D Poisson is solved. It includes the oxide and lays inbetween saturation point and drain junction, as marked in red. The rectangle has the length *ld*

we neglect the channel charge in this region and assume $Q_{inv} \approx 0$. Poisson defines

$$\Delta\Phi_{2D} = -\frac{\rho}{\epsilon} = -\frac{Q_{dep} + Q_{inv}}{\epsilon}. \tag{1}$$

With the above mentioned assumptions we receive

$$\Delta\Phi_{2D} \approx 0. \tag{2}$$

This leads to a 2D Laplacian problem. Schwarz-Christoffel can be used to solve our 2D problem in an analytical closed form by using linear conformal mapping technique. Before using Schwarz-Christoffel method we need to define the area wherein we solve 2D Laplacian. We solve 2D Laplacian in the region in between saturation point and drain junction and include the oxide. In Fig. 6 we have drawn the specified area in red lines. The rectangle has the length *ld*, which is the length of the saturation region.

In order to keep the approach for the conformal mapping technique as simple as possible the discontinuity of the electric field caused by the two different permittivities of the materials must be avoided [8]. This can be done by scaling the oxide according to the relationship of the permittivity of the silicon-oxide and the silicon:

$$\tilde{t_{ox}} = \frac{\epsilon_{Si}}{\epsilon_{ox}} \cdot t_{ox}. \tag{3}$$

With this 2-corner structure we have a way to transform any point from z-plane, $z = x + jy$, into upper half of the w-plane, $w = u + jv$, and backwards by using

$$F(z) = \cosh\left(\frac{\pi \cdot z}{\Delta y}\right); \qquad z = F^{-1}(w) = \arccos h(z)\frac{\Delta y}{\pi}. \tag{4}$$

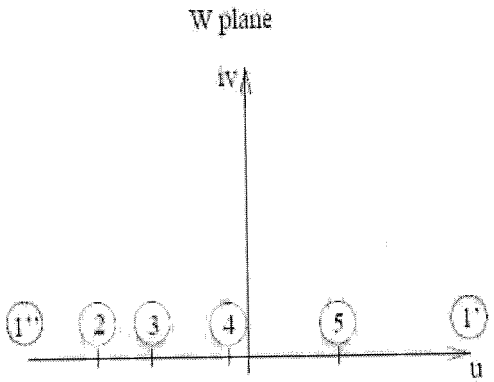

Fig. 7. Area wherein 2D Laplacian is solved transformed with Schwarz-Christoffel upon w-plane. All points are now located on the real axis

with $\Delta y = W + 2t_{ox}^{\sim}$. To calculate the potential in any point in the w-plane the integral

$$\Phi_{u,v} = \frac{1}{\pi}\int_{-\infty}^{+\infty} \frac{v}{(u-\bar{u})^2 - v^2}\Phi(\bar{u})\,d\bar{u}, \tag{5}$$

is to solve, whereby the rules of Schwarz-Christoffel have to be taken into account. Fig. 7 shows that with this approach all points in w-plane lay on the real axis. This simplifies the integration system and the equations can be solved in an analytical closed form. At last a transformation backwards is needed.

In Fig. 8(a) we cut out the region and mirror the same structure on the other side. As next we define the coordinates in there. The lower left corner we set as origin. So with point $z = (T_{ch} + 2 \cdot t_{ox}^{\sim}) + j\ (2\ ld)$ we span the rectangle. The oxide in Fig. 8(a) is represented by dotted lines. In y-direction we have the ending of the oxide $t_{ox}^{\sim}$ at the dotted lines. Then we enter channel region, which has the thickness T_{ch}. Therefore the next dotted lines in y-direction give the point $T_{ch} + t_{ox}^{\sim}$ and the rectangle area finishes with $T_{ch} + 2t_{ox}^{\sim}$. Going in x-direction we have the important point ld and 2 ld, when the rectangle ends.

The mirroring of the high field saturation region with the same boundary conditions create a 4-corner problem. This has the advantage that we force an electrical field of 0 at the saturation point. However, since our 4-corner problem is symmetric, we only need to solve half of the structure. By marking several important points along the boundary (see Fig. 8(b)), we can define different parts and split our boundary conditions. Point 1'represents the distance between drain junction and saturation point. With point 2 we

define the upper corner $T_{ch} + 2t_{ox}^{\sim}$ and the end of the oxide $T_{ch} + t_{ox}^{\sim}$ is given by point 3. Point 4 is the end of the channel $t_{ox}^{\sim}$. Point 5 is the origin of the coordinate plane. At last we give the saturation point the number 6. After applying conformal mapping technique, we transformed everything to w-plane as shown in Fig. 8(c). All the points are now located on the real

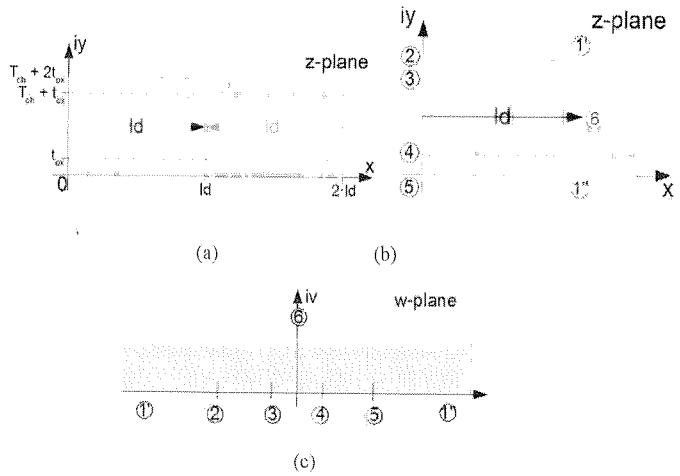

Fig. 8. (a.) Cutout of the region wherein 2D Poisson is solved. This region is mirrored in order to receive an electrical field of 0 in the saturation point. Drain end is now located on both sides as well as $V_{ds} + V_{bi}$ is applied to both sides. (b.) Half of the region shown above has to be solved due to symmetric reasons. Several important points are numbered and the saturation point with number 6. (c.) The before shown geometry in z-plane is now mapped with Schwarz-Christoffel in the upper half of w-plane. All points lay on the real axis except for the saturation point, which is located on the imaginary axis

axis u except the saturation point, which we find on the imaginary axis v. Our applied boundary conditions themselves do not consider the threshold voltage or the drain induced barrier lowering (DIBL). We include this by choosing appropriate values for the saturation voltage and the electric field in the saturation point. Hence, the device length is not included in the boundary conditions. Instead this parameter affects the saturation voltage as well as the electric field. The longer the device, the higher the saturation voltage.

In conformal mapping technique the law of superposition still holds. The mirrored geometry as described above has the electric field of 0 at saturation point. By splitting up the 2D Laplace equation,

$$\Delta\Phi_{2D} = \Delta\varphi_{2D} + \Delta\phi_{1D} \tag{6}$$

we can imprint an additional electrical field Ep at saturation point, which is explained in details in section IV, in the 1D part of the boundary conditions.

As basic approach we define a voltage depending on ld and E_p,

$$V_{d'} = ld \cdot \varepsilon_p + V_{gs} - V_{fb}. \tag{7}$$

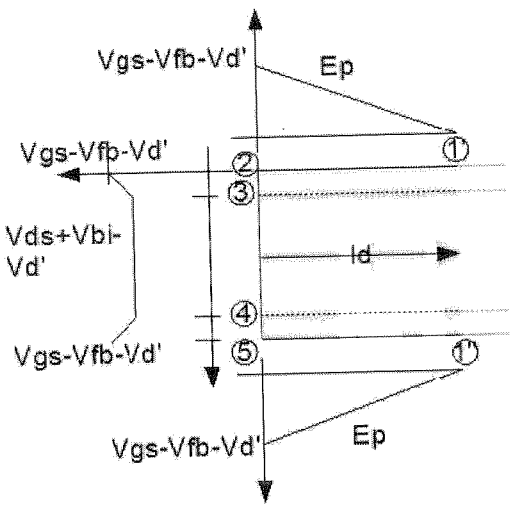

Fig. 9. Boundary conditions along the area wherein 2D Laplacian $\Delta\varphi$ 2D = 0 is solved

The flatband voltage is Vfb and Vgs is the gate to source voltage. So, we replace the 1D part of the Laplacian in (6) by

$$\phi_{1D} = V_{d'} - \varepsilon_p \cdot x. \tag{8}$$

As mentioned above we de?ne for each section of the boundary conditions different equations. From Eqn. (6) we transform $\Delta\varphi 2D = \Delta\Phi 2D - \Delta\phi 1D$. This is shown in Fig. 9.

1) *From 1 to 2:* Along the gate we have a constant voltage of $V_{gs} - V_{fb}$. Calculating the boundary condition

$$\varphi_{2D}(x, y = T_{ch} + 2 \cdot t_{ox}^{\sim}) = V_{gs} - V_{fb} - \phi_{1D}(x) = \varepsilon_p \cdot (x - ld) \tag{9}$$

for the Laplacian. Putting this into the integration system Eqn. (5)

$$\Phi_1(u, v) = \frac{1}{\pi} \int_{x=ld}^{x=0} \frac{v}{v^2 + (u - \bar{u})^2} \cdot \varepsilon_p \cdot \left(arc\cosh(\bar{u}) \frac{\Delta y}{\pi} - ld \right) \tag{10}$$

For the case 5 to 1" we have the same boundary conditions, for this we have to solve the same equation system. So we multiply this solution by 2.

2) From 2 to 3: Along boundary 2 to 3 we have the same results as for 4 to 5. For this we multiply this result by 2. Therefore we calculate for 4 to 5 through the oxide with a linear voltage drop

$$\varphi_{2D}(x = 0, y) = V_{gs} - V_{fb} - \frac{V_{gs} - V_{fb} - V_{ds} - V_{bi}}{t_{ox}^{\sim}} \cdot y - \phi_{1D}(x = 0). \tag{11}$$

It leads to

$$\Phi_2(u,\upsilon) = \frac{1}{\pi}\int_{y=t_{ox}^{\sim}}^{y=0} \frac{\upsilon}{\upsilon^2+(u-\bar{u})^2}\cdot\left(\frac{V_{gs}-V_{fb}-V_{ds}-V_{bi}}{t_{ox}^{\sim}}\cdot \arccos h(\bar{u})\frac{\Delta y}{\pi} - \varepsilon_p\cdot ld\right). \quad (12)$$

3) From 3 to 4: Along the drain junction we need to take into account $V_{ds} + V_{bi}$ with

$$\varphi_{2D}(x=0,y) = V_{ds} + V_{bi} - \phi_{1D}(x=0). \quad (13)$$

$$\Phi_3(u,\upsilon) = \frac{1}{\pi}\int_{y=T_{ch}+t_{ox}^{\sim}}^{y=t_{ox}^{\sim}} \frac{\upsilon}{\upsilon^2+(u-\bar{u})^2}\cdot\left(V_{ds}+V_{bi}-\varepsilon_p\cdot ld\right) \quad (14)$$

This integration system can be solved by,

$$\Phi_3 = -\frac{1}{\pi}\cdot\left(V_{ds}+V_{bi}-\varepsilon_p\cdot ld\right)\cdot(\arctan(-a+u)/\upsilon) - \arctan((-b+u)/\upsilon). \quad (15)$$

For a and b the upper and lower boundary of the integration system are used,

$$a = \cosh\left(\pi\cdot\frac{ld + j\cdot(2\cdot t_{ox}^{\sim}+T_{ch})}{2\cdot t_{ox}^{\sim}+T_{ch}}\right) \quad (16)$$

and

$$b = \cosh\left(\pi\cdot\frac{ld + j\cdot(t_{ox}^{\sim})}{2\cdot t_{ox}^{\sim}+T_{ch}}\right). \quad (17)$$

The integral system in Eqn. (10) and (12) cannot be solved in analytical closed form due to the arc hyperbolic cosine term. Essentially this term can be replaced by a Taylor series. Nevertheless, looking at the transformed boundary conditions from z-plane to w-plane, means the function $\Phi(u)$, as shown in Fig. 10, we see that constant boundary conditions stay constant by transforming those from z-plane to w-plane, whereby linear shaped functions in z-plane become a cosine hyperbolic function, which can be substituted by a parabolically shaped function. Looking at our results in Fig. 11 for a channel length of *50nm* and a channel width of *10nm* we have a maximum *ld* of *9nm*. In a small range like this an arc hyberbolic cosine function can be replaced by a square-root approximation. The inaccuracy increases with a higher *ld* and $t_{ox}^{\sim}$.

With *ld* = *9nm* we have a difference between integral along the function and the approximation of less than 1%. Since our oxide even when transformed into $t_{ox}^{\sim}$ is less than *5nm* the results have no noticeable difference.

Basically we can use for both equations the same solution with different parameters. For the solution we see, that Eqn. (10) and (12) consist of a constant part and the arc hyperbolicus cosine term hyperbolicus cosine term, which are split in

$$\Phi_{1,2} = sol_1 + sol_2. \quad (18)$$

The constant part can be solved easily,

$$sol_1 = -\frac{1}{\pi} \cdot \varepsilon_p \cdot ld \cdot (\arctan(-a+u)/v) - \arctan((u+1)/v). \tag{19}$$

For Eqn. (10) the parameter a is

$$a1 = \cosh\left(\pi \cdot \frac{ld + j \cdot (2 \cdot t_{ox}^{\sim} + T_{ch})}{2 \cdot t_{ox}^{\sim} + T_{ch}}\right) \tag{20}$$

and for Eqn. (12)

$$a2 = \cosh\left(\pi \cdot \frac{ld + j \cdot (t_{ox}^{\sim} + T_{ch})}{2 \cdot t_{ox}^{\sim} + T_{ch}}\right) \tag{21}$$

Replacing in Eqn. (10) and (12) the arccosh term with

$$\varphi_{2D}(\bar{u}) = \cdot \sqrt{\frac{x - \cosh\left(\frac{j \cdot \Delta y \cdot \pi}{\Delta y}\right)}{p}}, \tag{22}$$

the solution for this part is

$$\begin{aligned} sol_2 = {} & \frac{1}{4 \cdot \pi} \cdot (1/p)^{(1/2)} \cdot \left(4 \cdot \arctan\left(\left(2 \cdot (a1+1)^{(1/2)} + K_+(u,v)\right)/K_-(u,v)\right) \cdot v^2\right. \\ & \left. -4 \cdot \arctan\left(\left(-2 \cdot (a1+1)^{(1/2)} + K_+(u,v)\right)/ + K_-(u,v)\right) \cdot v^2\right)/v/K_-(u,v) \end{aligned} \tag{23}$$

with

$$K(u,v) \pm = \left(2 \cdot \left(u^2 + 2 \cdot u + v2 + 1\right)^{(1/2)} \pm 2 \cdot u \pm 2\right)^{(1/2)}. \tag{24}$$

Again we have to use for a the both above mentioned equations for $a1$ and $a2$, respectively.

Both square-root approximations have different derivative, whereby for Eqn. (10) the parameter

$$p1 = \frac{\cosh\left(\frac{(ld + j \cdot \Delta y) \cdot \pi}{\Delta y}\right) - \cosh\left(\frac{j \cdot \Delta y \cdot \pi}{\Delta y}\right)}{\left(\varepsilon_p \cdot ld\right)^2} \tag{25}$$

and for Eqn. (12)

$$p2 = -\frac{\cosh\left(\frac{(0 + j \cdot \Delta y) \cdot \pi}{\Delta y}\right) - \cosh\left(\frac{j \cdot (T_{ch} + t_{ox}^{\sim}) \cdot \pi}{\Delta y}\right)}{\left(V_{gs} - V_{fb} - V_{ds} - V_{bi}\right)^2}. \tag{26}$$

To come to the potential in the saturation point we have to add the solution for Eqn. (10), (12) and (14).

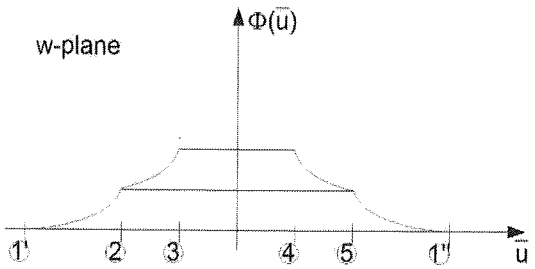

Fig. 10. Qualitative characteristics of the transformed boundary potential _(u). It is shown that constant boundary conditions stay constant by transforming those from z-plane to w-plane, whereby linear shaped functions in z-plane become a cosine hyperbolic function, which can be substituted by a parabolically shaped function

4. SATURATION VOLTAGE AND ELECTRICAL FIELD

For the calculation of the electric field at saturation point E_p and the voltage at saturation point V_{dsat}, we go back to Fig. 4. It shows that the channel is right underneath the oxide and vanishes when saturation point is reached. We make the assumption that up to saturation point each gate controls half of the channel and the influence of the gate is one-dimensional. So at saturation point we have

$$V_{gs} - V_{fb} = V_{ox} + \phi_i + V_{dsat}, \tag{27}$$

whereby V_{ox} is the voltage across the oxide and V_{fb} is the flatband voltage. The inversion potential at saturation point is given by ϕ_i. Since we define in high field saturation region no charge, we have no charge underneath the gate oxide. Therefore no voltage drop across the oxide appears, $V_{ox} = 0$. So we have the expression

$$V_{dsat} = V_{gs} - V_{fb} - \phi_i, \tag{28}$$

To calculate E_p we can describe the current in the saturation point as [10]

$$I_{dsat} = q_i \cdot T_{ch} \cdot W \cdot \mu_0 \frac{\varepsilon_p}{1 + \frac{\varepsilon_p}{\varepsilon_c}}. \tag{29}$$

q_i is the inversion charge per unit volume while assuming that the charge in pinch-off region is uniformly distributed along the film thickness, μ_0 the mobility of the electrons and E_c the critical electric field. This equation only calculates the current in the saturation point. In this point $V_{ox} = 0$, so mobility μ_0 indepent from the gate bias is used. The inversion charge is

$$q_i = q \cdot \frac{n_i^2}{N_B} \cdot \exp\left(\frac{\phi_i}{V_t}\right). \tag{30}$$

The elementary charge is given by q and V_t is the thermal voltage. Furthermore we can define the current in the saturation point with [10]

$$I_{dsat} = \frac{\mu_{eff} \cdot C_{ox} \cdot 2 \cdot W}{L\left(1 + \frac{V_{dsat}}{L \cdot \varepsilon_c}\right)} \cdot \left(V_{gs} - V_{th} - \frac{Vdsat}{2}\right) \cdot V_{dsat}. \tag{31}$$

C_{ox} represents the gate oxide capacitance per unit area, L is the gate length and the effective mobility μ_{eff} is given by [10]

$$\mu_{eff} = \frac{\mu_0}{1 + \theta \cdot \left(V_{gs} - V_{th}\right)} \tag{32}$$

With Eqn. (29) = Eqn. (31),

$$\varepsilon_p = \frac{1}{\frac{1}{\frac{\mu_{eff} \cdot C_{ox}}{q_i \cdot \frac{T_{ch}}{2} \cdot \mu_0 \cdot L\left(1 + \frac{V_{dsat}}{L \cdot \varepsilon_c}\right)} \cdot \left(V_{gs} - V_{th} - \frac{V_{dsat}}{2}\right) \cdot V_{dsat}} - \frac{1}{\varepsilon_c}} \tag{33}$$

we can calculate E_p depending on V_{ds} and V_{gs}. This is necessary because the saturation voltage is calculated independently of V_{ds}. With increasing drain-source voltage the saturation point moves source-wards. Keeping V_{dsat} at saturation point still constant the electric field E_p has to increase. To include this effect in the model, we need to calculate the electric field at described above.

After the definition of our V_{dsat} and E_p we can calculate *ld*. For this we vary our geometry with the boundary conditions from section 3. with the here calculated E_p included in the boundary conditions. When the potential Φ2D matches the defined $V_{dsat} + \phi_i$ the length *ld* of the geometry is the length of the high field saturation region.

5. RESULTS

In Fig. 11 and 12 are shown *ld* as function of V_{ds} for various V_{gs} for different devices. Fig. 11 has a channel length of $L = 50nm$ and a channel thickness of $T_{ch} = 10nm$, Fig. 12 has a channel length of $L = 20nm$.We compare our model to TCAD Sentaurus software and extract *ld* in the way as explained before. Our model is drawn in black lines and the TCAD Sentaurus in symbols.

We have used a critical electric field $E_c = 10^6 V/cm$ for both plots. With E_c the curves can be shifted in y-direction of the graphs in Fig. 11 and Fig. 12. It has no influence on the slope of the curves. So it was set to a reasonable value. The inversion potential is with

$$\phi_i = 2 \cdot V_t \ln\left(\frac{N_B}{n_i}\right) + \Delta\phi_{fit} \tag{34}$$

a good starting point for the fitting. It still needs some adjustment with $\phi_{fit} = -0.141V$ for $L = 50nm$ and $\phi_{fit} = -0.125V$ for $L = 20nm$. This value has the same influence

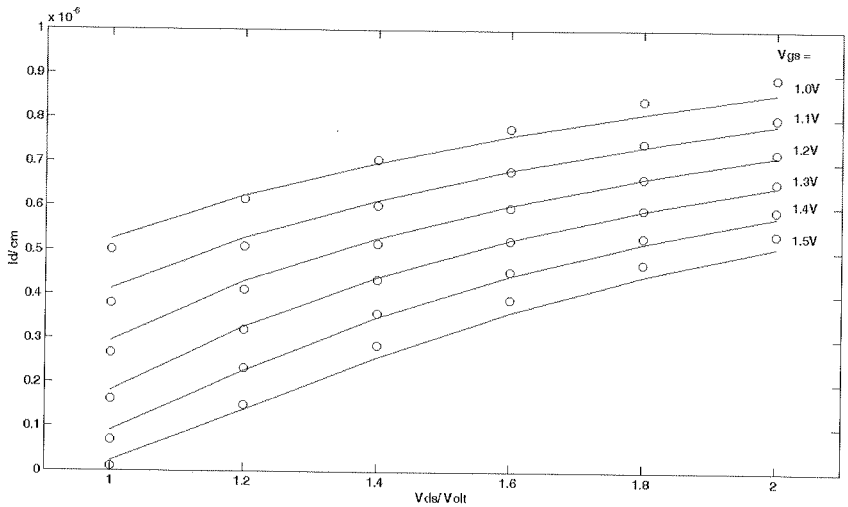

Fig. 11. Results for Id vs. V_{ds} for various V_{gs} calculated with a geometry with $L = 50nm$ and $T_{ch} = 10nm$. The lines represent model and the symbols the results from TCAD Sentaurus

as E_c a shift of the curves in y-direction. Again, we have no influence on the shape of the curve.

With the mobility model in Eqn. (32) we can influence the distance between all curves. The mobility μ_0 itself has no influence, since Eqn. (29) = Eqn. (31). Nevertheless, θ in Eqn. (32) for the influence of V_{gs} is set to 0.01 for $L = 50nm$ and 0.5 for $L = 20nm$.

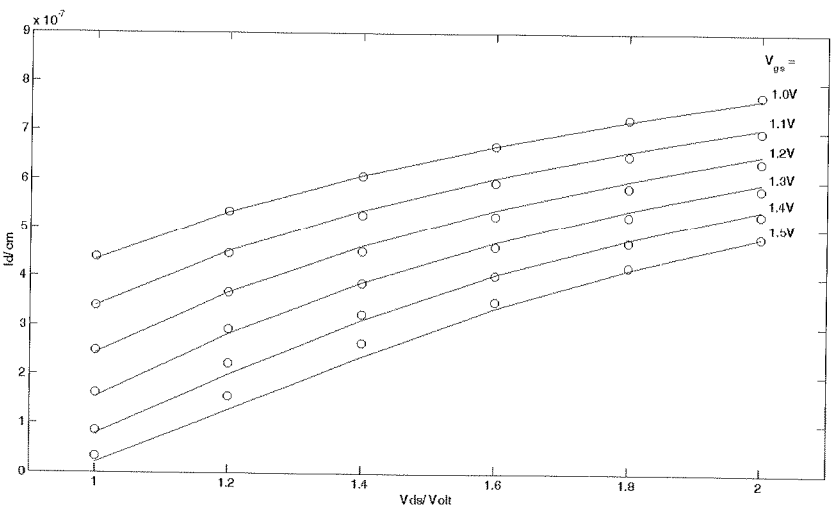

Fig. 12. Results for Id vs. V_{ds} for various V_{gs} calculated with a geometry with $L = 20nm$ and $T_{ch} = 10nm$. The lines represent model and the symbols the results from TCAD Sentaurus

Our model is in good agreement with the simulation results. Also with $V_{gs} = 1V$ to $1.5V$ with a $V_T \approx 0.45V$ we cover with our results up to almost *10nm* channel length modulation. Fig. 11 and Fig. 12 show quite similar values for channel length shortening. Indeed channel length shortening depends mainly on drain site of the device. Only with very short devices the source end starts to affect the channel length shortening and the distance between drain junction and saturation point becomes shorter.

6. CONCLUSION

In the paper we presented a model for the calculation of the saturation point for DoubleGate FETs. We solved 2D Poisson equation in an analytical closed form. This model does not introduce any unphysical fitting parameters. Furthermore the fitting parameters, mobility and inversion potential, have minor influence on the shape of the curves as shown in Fig. 11 and 12. We compared out model with simulation results from TCAD Sentarus for a device size of $T_{ch} = 10nm$ and $L = 50nm$ and $L = 20nm$ with a lightly doped channel. To compare those results we introduced a new definition for the saturation point. We define the saturation point reached, when the electric potential maximum moves rapidly from underneath the gate oxide to the middle of the channel of the DG FET.

REFERENCES

1. J.-W. Han, C.-H. Lee, D. Park, and Y.-K. Choi: *Quasi 3-d velocity saturation model for multiple-gate mosfets*, IEEE Trans., vol. 54, no. 5, pp. 1165–1170, 2007.
2. G. Pei and E. C. C. Kan: *A physical compact model of dg mosfet for mixed-signal circuit applications -part ii: Parameter extraction*, IEEE Trans., vol. 50, no. 10, pp. 2144–2153, 2003.
3. G. Pei, W. Ni, A. V. Kammula, B. A. Minch, and E. C. C. Kan: *A physical compact model of dg mosfet for mixed-signal circuit applications-part i: model description*, IEEE Trans., vol. 50, no. 10, pp. 2135–2143, 2003.
4. Weber: *Electromagnetic Fields*, 3rd ed. Wiley, 1950.
5. B. Iniguez, T. A. Fjeldly, A. Lazaro, F. Danneville, and M. J. Deen: *Compact-modeling solutions for nanoscale double-gate and gate-all-around mosfets*, IEEE Trans., vol. 53, no. 9, pp. 2128–2142, 2006.
6. A. Kloes, M. Weidemann, D. Goebel, and B. T. Bosworth: *Three-dimensional closed-form model for potential barrier in undoped finfets resulting in analytical equations for V_T and subthreshold slope*, IEEE Trans., vol. 55, no. 12, pp. 3467–3475, Dec. 2008.
7. M. Weidemann, A. Kloes, and B. Iniguez: *Compact model of output conductance in nanoscale bulk mosfet based on 2d analytical calculations*, Solid-State Electronics, vol. 52, no. 11, pp. 1722–1729, 2008.
8. A. Kloes and A. Kostka: *A new analytical method of solving 2d poisson's equation in mos devices applied to threshold voltage and subthreshold modeling*, Solid-State Electronics, vol. 39, no. 12, pp. 1761–1775, 1996.
9. *TCAD Sentaurus*, X-2005.10 ed., Synopsys, Inc., 2005.
10. N. Arora: *MOSFET Models for VLSI Circuit Simulation*. Springer-Verlag/ Wien, 1993.

ELECTRONICS AND TELECOMMUNICATIONS QUARTERLY, 2009, 55, no 4, pp. 563–575

A Behavioral Model for Sigma Delta Fractional PLL and Applications to Circuit Dimensioning

RUI DUARTE, JORGE R. FERNANDES

INESC-ID Lisboa, Portugal / Instituto Superior Técnico – T.U. Lisbon, Portugal
e-mail: rui.duarte@ieee.org ; jorge.fernandes@inesc-id.pt

Received 2009.09.22
Authorized 2009.11.17

This paper presents an accurate high level model for the design of sigma-delta fractional Phase locked loop (PLL) architectures. High level models provide simulation speedups of about two orders of magnitude when compared to transistor level simulation. When compared to other models presented in the literature the proposed model has the advantage of having the frequency instead of phase as the output of the VCO. This approach greatly simplifies the implementation of the PLL blocks and results in an increase of the overall model performance. Several nonlinear phenomenons's such as cycle slipping, spurious signals and phase noise are also accurately modelled. Finally, this paper combines genetic algorithms with the proposed behavioral model to optimize the PLL parameters and reduce the impact of the sigma-delta phase noise.

Keywords: PLL; RF; High level simulation of analog circuits, Genetic algorithms, Design automation

1. INTRODUCTION

Recent developments in CMOS technologies allow the integration of many functions in a single chip. Today, it is possible to combine powerful low power processors with advanced radio frequency (RF) transceivers. This combination has been the driving force behind many of today's popular wireless hand held devices such as cellular phones, PDA, smart phones and wireless LAN appliances. To deal with the increasing need for wireless links, many advanced wireless communications protocols have been developed targeting the unregulated and almost universal ISM bands (Instrumental, Scientific, and Medical). These protocols rely on synthesizers with high spectral

purity, small frequency steps and frequency hopping mechanisms to ensure secure communications.

To achieve the stringent requirements of these frequency synthesizers new techniques have been developed. One of such techniques relies on the use of a sigma delta modulator [1][2][3] to switch the PLL feedback divider so that in average a fractional divide ratio can be obtained. This technique has been proven to be successful in achieving high resolution frequency synthesizers with fast settling times. Another advantage of the sigma delta fractional PLL is that it requires practically no architecture changes to the conventional PLL, it only adds a sigma delta to the overall circuit.

However, the use of sigma delta modulation in the PLL introduces spurious signals and noise due to the divider switching, which can seriously compromise system performance. To ensure proper circuit operation, it is therefore extremely important to analyze and simulate the sigma delta influence on the PLL behavior.

The simulation of fractional PLL synthesizers is a very difficult task because there are time constants with very different orders of magnitude present in the synthesizer, requiring long simulation times with small time steps to capture all its effects. Transistor level simulations become impractical due to the complexity of the models used.

To solve these problems many behavioral models [4][5] [6][7] [8] have been developed in specialized high level languages such as Verilog, VHDL, MATLAB and even in C++. The precision of such models depends on the behavioral detail included, which is sometimes sacrificed for speed of simulation. In the proposed behavioral model, a careful selection of the PLL variables to model at each node, and a correct choice of behavior detail to include, allow us to obtain a very precise sigma delta PLL behavior model. The main difference between the proposed model and the typical models found in the literature resides in the fact of using a frequency output instead of phase, this choice simplifies the voltage controlled oscillator (VCO) and the divider model which contribute to the overall simulation performance.

There are many applications for high performance PLL simulation, a very important one is the ability to combine behavioral models with genetic algorithms and automate the dimensioning and optimization of circuit parameters. Genetic algorithms require the evaluation of many PLL circuits with different combinations of parameter in order for the algorithm to converge. With transistor level simulations this approach takes an impractical amount of time. However, with a fast behavioral model the automatic dimensioning of the PLL can now be feasible. This work takes on this approach to minimize one of the most serious drawbacks of sigma delta fractional PLL, the sigma delta generated phase noise.

The material presented in this paper is organized as follows; Section 2 describes the operation of a sigma delta PLL; Section 3 presents the PLL behavioral model; Section 4 provides the model for the several noise sources that can be found in a PLL; Section 5 combines genetic algorithms and the behavioral model to automatically tune the PLL parameters and minimize the sigma delta generated phase noise; Finally the conclusions are presented in section 6.

2. SIGMA-DELTA PHASE-LOCKED LOOP

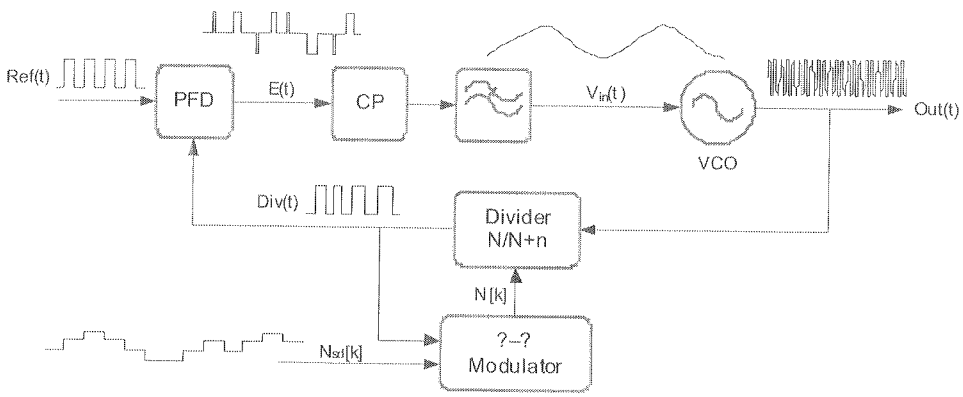

Fig. 1. Sigma-Delta Phase-locked Loop

A PLL can be considered as a feedback system that controls the frequency and phase of the output signal according to a reference signal at its input. Fig. 1 shows the block diagram of a sigma delta fractional PLL with all its relevant wave forms represented. Normally the output signal is sinusoidal and therefore has a defined output phase at any time instant. The reference signal, however, is normally a square wave and we can only determine its phase at the rising or falling edges. We can consider the reference signal as a discrete time phase signal and the output of the VCO as a continuous time phase signal. To make it possible to compare these two signals in the phase and frequency detector (PFD) we have to sample the VCO output and turn it into a discrete time phase sequence similar to the reference. Both these operations are performed in the feedback frequency divider. The feedback divider is also responsible for imposing a fixed ratio between the reference and the output frequencies. In the PFD the two discrete phase signals are compared and a discrete phase error signal is generated. This phase error signal is then converted to a current by the charge pump (CP) and processed by a continuous time filter. The PLL loop filter softens the discrete time phase error pulses by averaging, generating a continuous time phase error signal. The continuous time phase error signal is fed to the VCO so that its output can correct the phase difference. Fractional PLL synthesizers often use a sigma delta to switch randomly the divider modulus, so that in average a fractional divide ratio is obtained. The use of a sigma delta provides the advantage of filtering the divider switching noise causing most of it to appear at high frequencies. Careful dimensioning of sigma delta order and loop filter bandwidth can relocate most of the divider switching noise out of the loop filter bandwidth where its effects are greatly attenuated.

3. PLL MODELLING

The proposed model for the PLL has 3 distinct parts consisting of an initialization script; a parameterized model; and a processing script. Fig. 2 shows the organizational diagram of the PLL model and briefly describes each of the model steps.

The initialization script is the user interface to the model. Here, the user can specify the SD PLL parameters and define the simulation conditions, such as the sampling frequency and frequency resolution of the PLL internal signals.

The parameterized model is the core of the proposed PLL model, it models the PLL behavior and it is the most computational intensive part of the model. The main objective of the parameterized model is to provide a flexible and accurate behavioral description of the PLL that can be simulated fast enough to improve the design cycle and architectural study of fractional sigma delta PLLs. This is not an easy task, since accurate behavioral modeling implies detailed voltage level description, on the other end, fast simulation times normally can only be achieved with simplified and less accurate PLL descriptions. To accommodate these two requirements the proposed model is the result of a careful study of the PLL internal nodes and the PLL non-idealities, so that only the most critical nodes and the most problematic non-idealities are modelled with full detail.

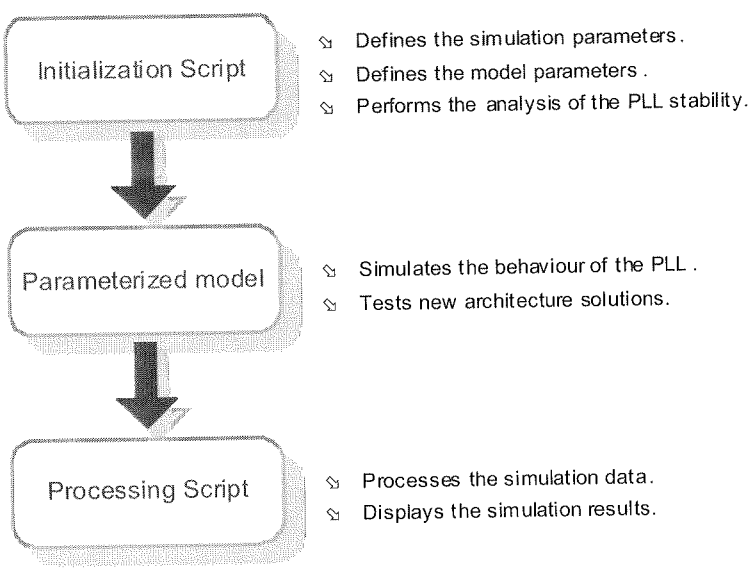

Fig. 2. Proposed model organization

In Fig. 1 we can see that the only block that processes discrete time phase quantities is the PFD. The discrete nature of the PFD contributes to many non ideal effects of

the PLL and as such it is modelled with great detail using digital wave forms and the digital circuit of Fig. 3.

The blocks following the PFD do not pose any modelling problems, the CP is modelled by a simple gain and the loop filter is modelled by its transfer function.

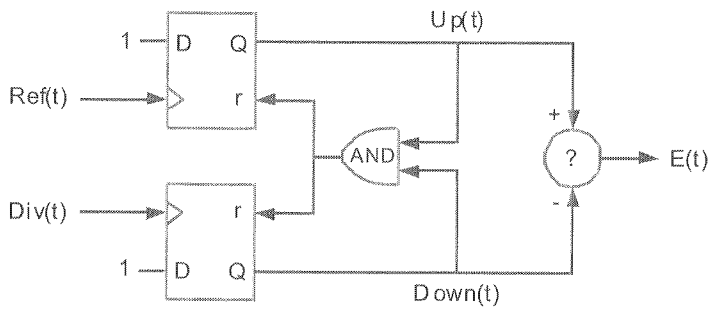

Fig. 3. PFD model

Traditional VCO models use a phase variable as the output of the VCO, phase outputs simplify the VCO modeling but provide a quantity that is always increasing. The constantly increasing phase at the output of the VCO can be problematic when it is necessary to detect small phase deviations such as spurious signals and phase noise. To solve these problems several models wrap around the phase for every 2π radians. This approach, however, complicates the analysis of the simulation results and phase noise analysis. In this work, we use a different solution and select a frequency variable as the VCO output. A frequency output simplifies the VCO model to the linear relation presented in (1) and provides a limited quantity at the VCO output, which results in a more straightforward analysis of the results.

$$f_{VCO} = K_v \times V_{in}(t) + f_{nom} \tag{1}$$

To model phase noise at the VCO output it is now necessary to convert it to frequency noise. This is not a complicate issue and can be done without any additional computational penalty as it will be shown later. The frequency divider is implemented simply by dividing the VCO frequency by the divide ratio.

For the model of sigma delta we use the known equations for a m^{th} order modulator [4]:

$$Y(z) = H_X(z)\,X(z) + H_Q(z)\,E_Q(z) \tag{2}$$

Where $H_X(z)$ is the signal transfer function, $H_Q(z)$ is the quantization noise transfer function, $X(z)$ is the input signal and $E_Q(z)$ is the quantization noise. The signal and quantization transfer functions for the m^{th} order modulator are respectively [4]:

$$H_X(z) = z^{-m} \tag{3}$$

$$H_Q(z) = \left(1 - z^{-1}\right)^m \tag{4}$$

The sigma delta fractional PLL operates with constant values at the sigma delta input. Sigma delta circuits with constant or DC inputs are known to suffer from limit cycle problems which generate periodic sequences at the sigma delta output. These periodic sequences have an undesired effect of causing strong spurious signals at the PLL output. To avoid this problem, sigma delta PLLs have some kind of dithering circuits which generate long pseudorandom sequences of zeros and ones used to drive the least significant bit of the sigma delta. To model the use of dithering circuits in the PLL, a Pseudo-Noise (PN) sequence generator with configurable generation polynomial was used. The output of the PN generator is the scaled to the value of the least significant bit of the sigma delta and added to the fractional divide ratio.

Fig. 4 presents the complete PLL model including the switches that allow the simulation of the PLL with one or both noise sources. Also the sigma delta noise can be deactivated by setting the fractional divide ratio to zero.

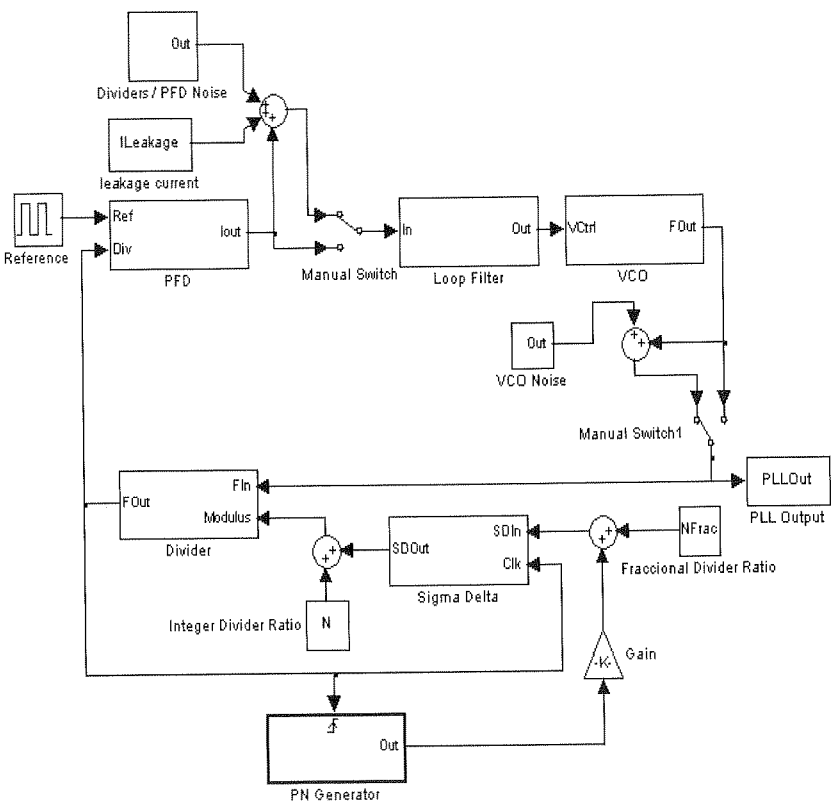

Fig. 4. Complete block diagram of the proposed sigma delta PLL model

The final part of the PLL model is the processing script. The processing script uses the results obtained through the parameterized model simulation and calculates the discrete Fourier transform of the PLL output to determine its spectral purity.

Fig. 5 shows the wave form at the VCO output obtained using the proposed model and Fig. 6 shows the spectral purity of the simulated synthesizer. Fig. 7 and Fig. 8 provide a design example where two different loop filters are simulated to determine their influence on the sigma delta spurious signal of a fractional PLL.

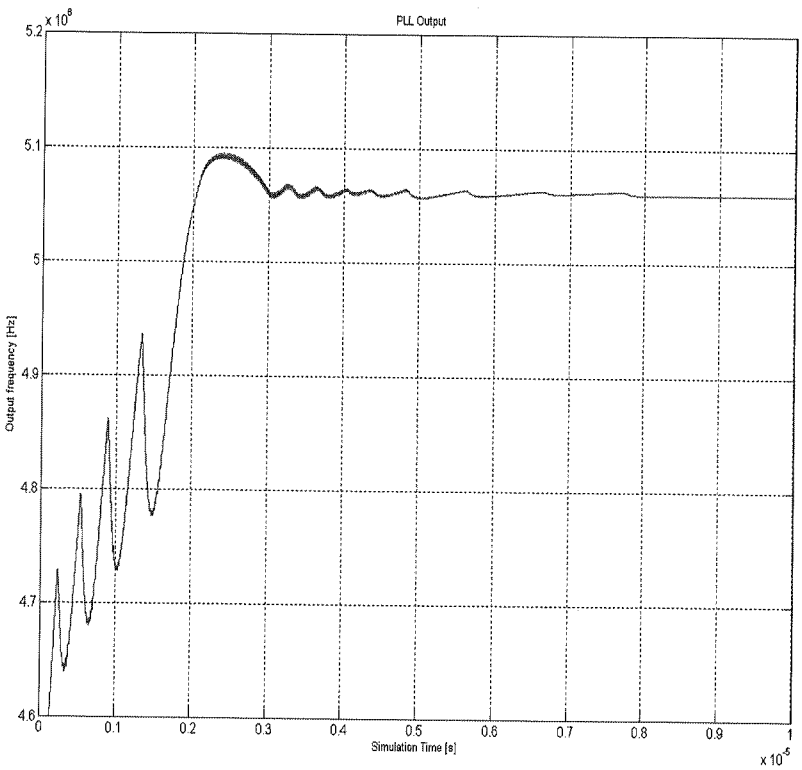

Fig. 5. Transient simulation of the VCO output showing nonlinearities in the PLL locking (cycle slipping)

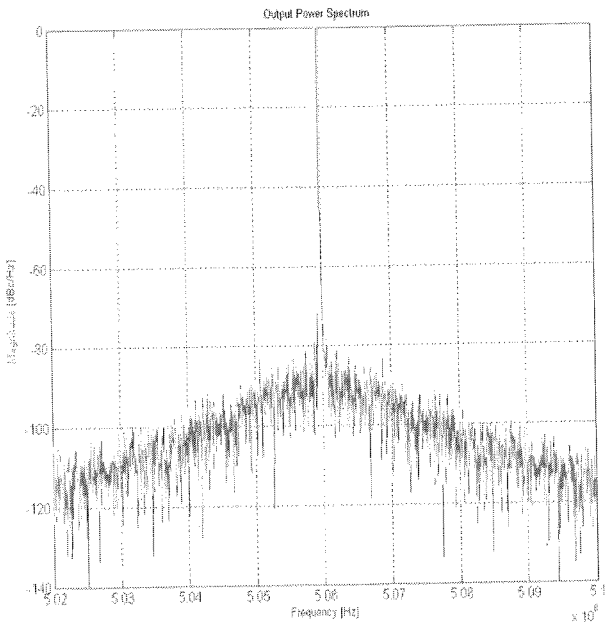

Fig. 6. Spectral purity of the PLL synthesizer with an integer divide ratio and added noise

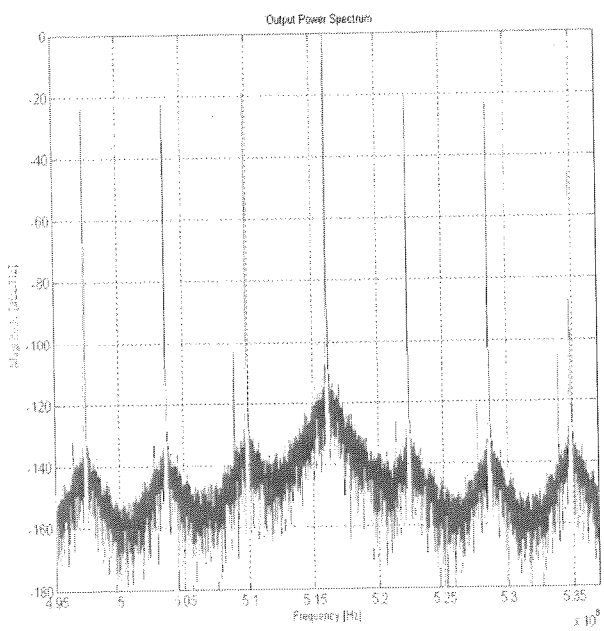

Fig. 7. Spectral purity of the synthesizer with a fractional divide ratio and a large loop filter bandwidth

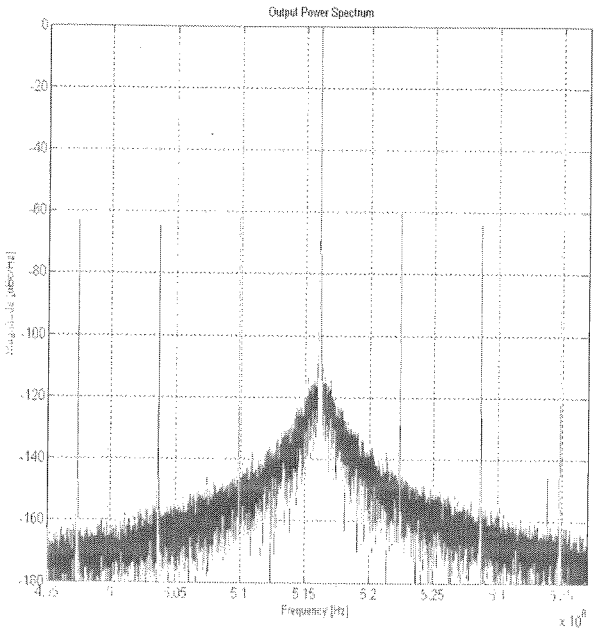

Fig. 8. Spectral purity of the synthesizer with a fractional divide ratio and a smaller loop filter bandwidth

4. NOISE MODELLING

The developed PLL noise model accounts for the noise and leakage effects present in the several PLL components and it is divided in three different parts. The first part is responsible for modelling leakage effect in the charge pump, which contribute to reference signal spurious at the VCO output. This leakage effect is simply modelled by subtracting a current source to the output node of the PFD. The next two parts model the noise contribution of the active devices present in the PLL building block. To simplify the noise analysis the noise sources present in the PLL where grouped into two classes, the noise sources that are low pass filtered by the PLL and the noise sources that are high pass filtered by the PLL. The low pass filtered noise sources are traditionally referred to the input of the PFD and are designated by equivalent PLL noise at the PFD input. The high pass filtered noise sources are referred to the VCO output and are normally designated by the equivalent VCO noise. In this model the equivalent PLL noise is added to the PFD output instead of being added to the PFD input, since it is very complicated to add phase noise to a digital wave form. For the equivalent VCO noise it is necessary to convert the phase noise to frequency noise because the VCO output is a frequency value.

The noise sources found in the PLL are not just white noise sources, the active devices present in the PLL generate flicker noise which greatly affects the phase noise at small offsets from the carrier. The noise model is implemented using a Gaussian random number generator with zero mean to obtain a noise sample for each simulation time step. The noise obtained is white and has a spectral density that depends on the variance of the random generator, the simulation step and simulation duration. The spectral power density of the simulated noise expressed in dB is given by:

$$\overline{v_n^2} = 10\log_{10}\left(\sigma^2\right) + 10\log_{10}\left(SimStep/SimTime\right) \tag{5}$$

The other noise regions are implemented by passing the white noise through continuous time filters. Frequency is the derivative of phase, so to add the equivalent VCO noise at the VCO output the f^{-3}, f^{-2} and f^{0} regions of phase noise are respectively converted to the frequency noise regions f^{-1}, f^{0} and f^{-2}. With this conversion it is possible to use the same noise model to add phase and frequency noise without any computational overhead. As a final remark, every noise source modelled has its own random generator so that they are all uncorrelated. The noise model parameters of the PLL are defined in the initialization script and it is possible to define the white noise floor and the noise corner frequencies that separate the several noise regions. The noise transition regions correspond to setting the bandwidth of the noise shaping filters.

5. COMBINING GENETIC ALGORITHMS AND THE BEHAVIORAL MODEL

Genetic algorithms are inspired on natural selection and other processes that drive the biologic evolution of species. Genetic algorithms are particularly useful when the optimization objective function is discrete, strongly non-linear or non-differentiable. A genetic algorithm iteratively selects and modifies individuals from an initial population of solutions so that from generation to generation the whole population converges to an optimal solution. The ability to optimize problems that do not have continuous and differentiable objective function, makes genetic algorithms an useful tool to iterative simulate and evolve the parameters of a circuit in order to optimize its performance. In this study the behavioral model for the sigma delta PLL is used as an objective function. The genetic algorithm then iteratively selects and modifies an initial set of PLL parameters, so that from generation to generation the set of parameter evolve to obtain an optimized phase noise.

The genetic algorithm starts by generating a random set of initial specifications as an initial population of possible PLL implementations. At each generation the population of PLLs is evaluated by using the behavioral model to obtain the output phase noise. After that, the population of PLLs is ranked by its phase noise performance. The next generation of PLL specifications is obtained from the previous by a combination of three different methods: A percentage of the top performance specification, or elite individuals, are simply propagated to the next generation. A number of top performers

are selected to reproduce and generate offspring's by interchanging some of their specification. A number of individuals from the previous generation are randomly selected to suffer random changes (mutations) to their specifications. The algorithm stops when one of the stop conditions is verified. These conditions can be a limit of generations, a limit of simulated time and a number of stall generations in which the algorithm does not provide a better solution.

As a demonstration of the capabilities of genetic algorithms combined with a fast behavioral model, a test PLL circuit with a reference frequency of 10MHz, an output frequency of 100MHz and a 3^{rd} order sigma delta was optimized. The goal of the optimization is to reduce the sigma delta generated phase noise of the PLL at an offset frequency of 1MHz. The parameters which where subject to the optimization process are the loop filter bandwidth, the charge pump current and the VCO gain. Furthermore, during the optimization process these parameters where subject to an upper and lower limit. The loop filter was limited from 10KHz to 1MHz, the charge pump current was limited from 10μA to 400μA, and finally the VCO gain was limited from 100KHz/V to 10MHz/V.

Fig. 9, Fig. 10 and Fig. 11 illustrate the operation of the genetic algorithm. In this optimization example a population of seven PLL specification where used and limit number of eight generations where simulated. This gives a total number of 63 PLL simulations (initial population plus eight generations times seven elements per generation) and a total simulation time of 43.3 minutes on a netbook PC with an Atom N280 1.66GHz processor. The population of each new generation was obtained using two elite individuals and the remaining elements obtained by crossover and mutation. The fraction of crossover children was 0.6 and the remaining children where mutation children as illustrated in Fig. 11.

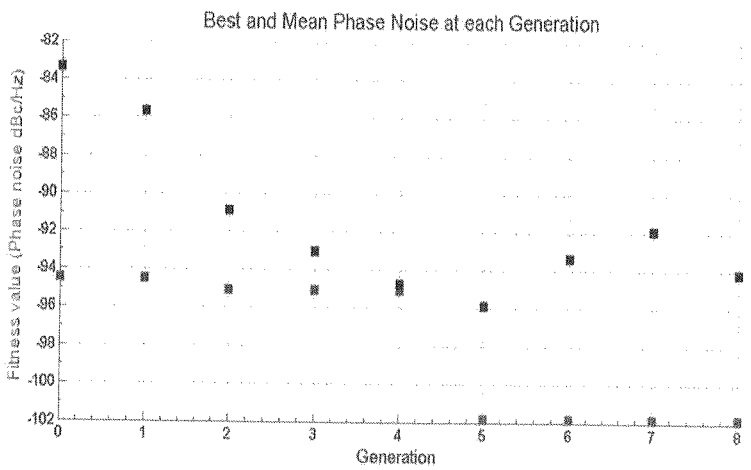

Fig. 9. Genetic algorithm convergence illustrated by the best and mean values of the fitness function

The optimization process stopped due to the stop limit of eight generation and the optimized values for the loop filter bandwidth, charge pump current and VCO gain where 186.4KHz, 354μA and 1.65MHz/V respectively. With these values an optimized phase noise of -101.8dBc/Hz@1MHz was obtained.

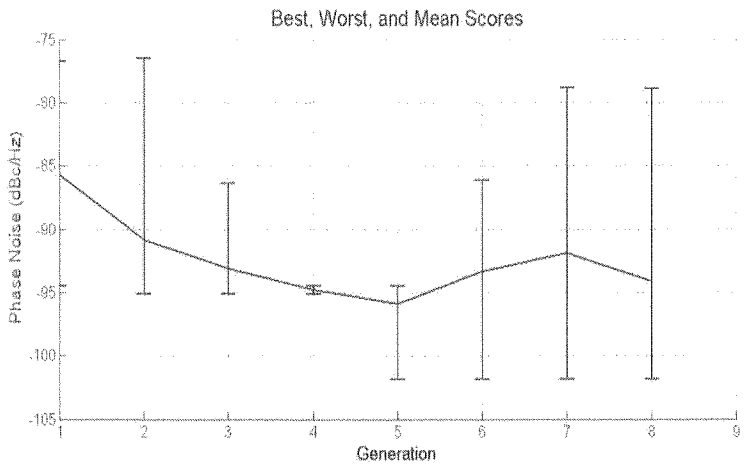

Fig. 10. Genetic algorithm population spread at each generation

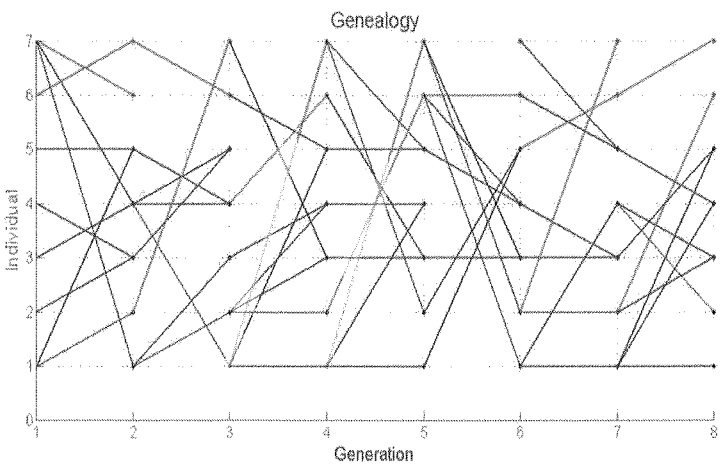

Fig. 11. Genealogy of the genetic algorithm, black lines represent elite individuals, red lines indicate mutation children and blue lines indicate crossover (reproduction) children

6. CONCLUSIONS

This paper has shown an accurate method of modelling sigma delta fractional PLLs without being to computational intensive. By selecting a frequency variable as

the output of the VCO, the problems of dealing with an unlimited phase quantity and phase wrapping were eliminated. A frequency variable for the VCO also results in simulation time speedups due to the simplicity of the VCO model. Noise and spurious signals models have also been presented, contributing further to a more precise and accurate PLL analysis.

It was also demonstrated that even though a frequency output has been used in the VCO model, the VCO noise can still be added to the output node simply by converting the several phase noise regions to frequency noise regions. This conversion can be performed before the simulation starts and requires no additional computational effort.

Finally it was demonstrated that by combining genetic algorithms and the proposed behavioral model a robust method for automatic dimensioning and optimization of PLL circuits can be obtained.

REFERENCES

1. I. Galton: *Delta–Sigma Data Conversion in Wireless Transceivers.* IEEE Transactions on Microwave Theory and Techniques, vol. 50, no. 1, January 2002.
2. S. E. Meninger and M. H. Perrott: *A Fractional-N Frequency Synthesizer Architecture Utilizing a Mismatch Compensated PFD/DAC Structure for Reduced Quantization-Induced Phase Noise.* IEEE Transactions on Circuits and Systems—II: Analog and Digital Signal Processing, vol. 50, no. 11, November 2003.
3. S. Pamarti, L. Jansson and I. Galton: *A Wideband 2.4-GHz Delta-Sigma Fractional-N PLL with 1-Mb/s In-Loop Modulation.* IEEE Journal of Solid-State Circuits, vol. 39, no. 1, January 2004.
4. S. R. Norsworthy, R. Schreier, and G. C. Temes: *Delta–Sigma Data Converters, Theory, Design, and Simulation.* New York: IEEE Press, 1997.
5. E. Drucker: *Model PLL Dynamics And Phase-Noise Performance.* MICROWAVES & RF, FEBRUARY 2000.
6. K. Kundert: *Predicting the Phase Noise and Jitter of PLL-Based Frequency Synthesizers.* The Designers Guide, Copyright © August 2006, Kenneth S. Kundert – Designer's Guide Consulting, Inc.
7. X. Mao, Huazhong, Y. H. Wang: *Behavioral Modeling and Simulation of Jitter and Phase Noise in Fractional-N PLL Frequency Synthesizer.*
8. M. H. Perrott, M. D. Trott and Ch. G. Sodini: *A Modeling Approach for Sigma Delta Fractional-N Frequency Synthesizers Allowing Straightforward Noise Analysis.* IEEE Journal of Solid-State Circuits, vol. 37, no. 8, August 2002.
9. X. Lai, Y. Wan and J. Roychowdhury: *Fast PLL Simulation Using Nonlinear VCO Macromodels for Accurate Prediction of Jitter and Cycle-Slipping due. to Loop Non-idealities and Supply Noise.* ASP-DAC 2005.
10. R. L. Haupt, S. E. Haupt: *Practical genetic algorithms 2nd ed.* Wiley-Interscience publication, 2004.
11. *Genetic Algorithm and Direct Search Toolbox™ User's Guide*, The Math Works, Inc. March 2009.

ELECTRONICS AND TELECOMMUNICATIONS QUARTERLY, 2009, 55, no 4, pp. 577–583

Duty Cycle Correction Using Negative Feedback Loop

SHARATH PATIL*, S. B. RUDRASWAMY**

*Kawasaki Microelectronics;
e-mail: sharathpatil85@gmail.com
**Sri Jayachamarajendra College of Engineering;
e-mail: rudra.swamy@gmail.com

Received 2009.10.05
Authorized 2009.11.18

An architecture has been proposed to obtain a duty cycle of nearly 50% for single-ended signals. The main idea is based on the fact that the average DC value of a signal is proportional to its Duty Cycle. So, if we assure that the signal and its inverted counterpart have equal average DC value, that particular signal will have a 50% duty cycle. A feedback circuit is used to compare the average DC values and correct the duty cycle of the signal. The duty correction circuit was implemented in 130nm technology with a power supply of 1.2 V. It was found by simulation that the circuit gives nearly 50% duty cycle at the output for a 500MHz signal when the input duty cycle is varied from 25% to 75%.

Keywords: Duty cycle Correction Analog solution Feedback

1. INTRODUCTION

Duty cycle distortion is introduced by device mismatches, process imbalance, etc. Duty cycle becomes an important specification when there is a minimum (or maximum) constraint on pulse width. One of those situations is when the signal has to be sampled by a clock at the receiver, during the valid data window. During such a situation, it should be ensured that the data signal is wide enough to be sampled in the valid data window to prevent distortions. There are several digital implementations for duty cycle correction. One of them has been explained in [1]. In this approach the duty correction circuit has been included in the DLL loop itself, but such an implementation might affect the working of the loop and may add jitter. Moreover, the circuitry and working is quite complex. In this paper, an analog solution has been proposed in which a negative feedback loop has been used for duty cycle correction. The loop settles within $1\mu s$

after enabling the circuit. There is no necessity of a reference voltage as the reference is generated using the signal itself. Also, because the correction circuit can be isolated from the PLL/DLL loop, it doesn't affect the working of the clock circuits.

A method is proposed in [2] for duty cycle correction of high frequency signals [about 2.5 GHz]. But for low frequency signals [500 MHz to 1 GHz] the simple method proposed can be used.

The working of the proposed duty correction circuit and its block diagram has been explained in section II. The results of simulation have been summarized in section III. Section IV contains the conclusion and future work needed to improve the performance.

2. PROPOSED ARCHITECTURE

Figure 1 shows the proposed architecture for duty cycle correction. It has the following blocks: Average value detector, Comparator and Duty-alter block. VErr is adjusted until VA and VB are equal, by the action of the feedback loop and the comparator.

2.1. PROPOSED AVERAGE VALUE DETECTOR

The average value detector is basically a low pass filter which filters out high frequency components and retains the average DC value of the signal. The simple architecture that was used for the purpose is shown in Fig. 2. The working has been explained below:

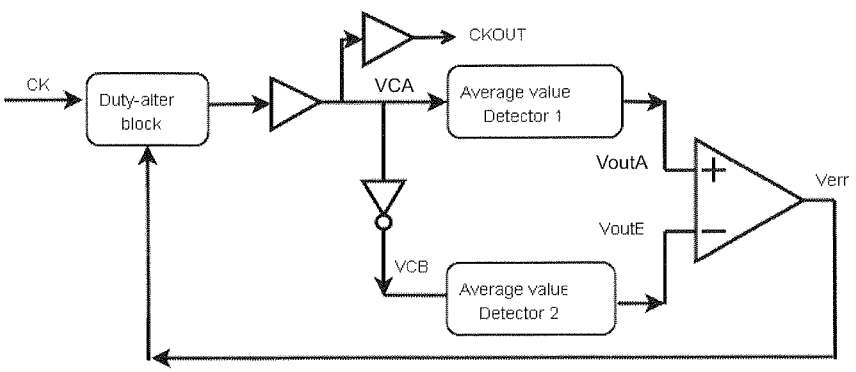

Fig. 1. Block diagram of the proposed architecture

When VCA is high, M1 is ON and the current IDC flows to ground. When VCA is low, M1 is OFF and the current IDC flows through the RC circuit and charges C1to VoutA. Consider the charge Q accumulated across the capacitor C1, given by

$$Q = C1 * VoutA \tag{1}$$

$$\text{ButQ} = C1 * \text{VoutA} \tag{2}$$

From (1) and (2) we have,

$$\text{IDC} * \text{TOFF} = C1 * \text{Vout} \tag{3}$$

$$\text{Or VoutA} = (\text{IDC} * \text{TOFF})/(C1) \tag{4}$$

VoutA is proportional to TOFF

$$\text{Similarly, VoutB} = (\text{IDC} * \text{TON})/(C1) \tag{5}$$

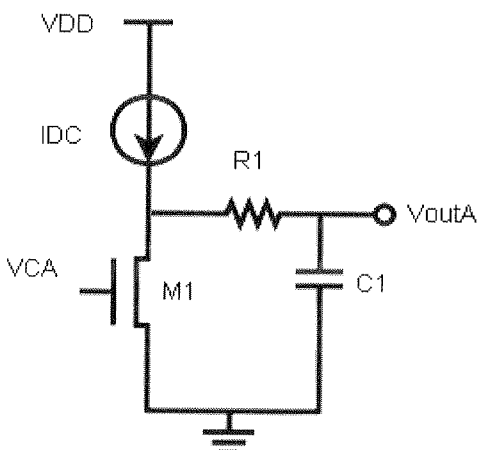

Fig. 2. Schematic of average value detector

The waveforms of VCA and VCB can be referred from Fig. 3.

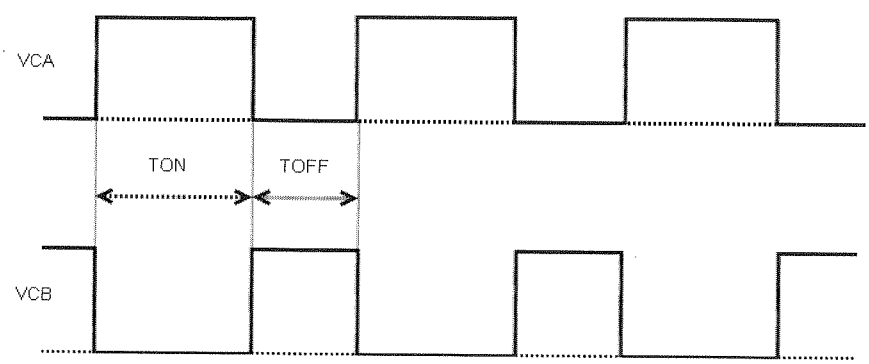

Fig. 3. Waveforms of VCA and VCB

Experimentation is going on with alternative circuit for average value detector. A circuit which is similar to a charge pump, shown in Fig. 4 is found to provide duty

correction over a range of frequencies (200MHz to 1 GHz) but the feedback loop is not stable at low input duty cycle (30%) at FF corner. So, currently work is going on to improve the stability of the loop.

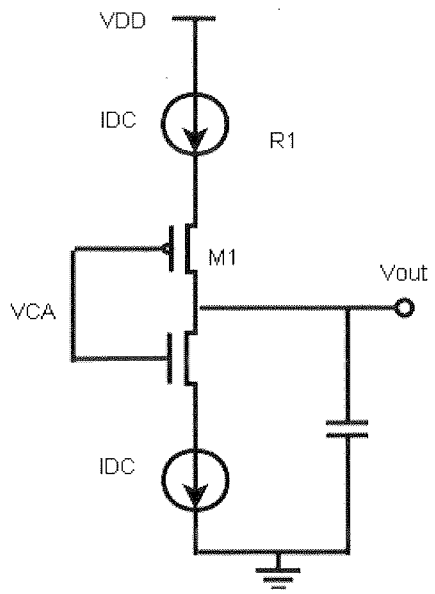

Fig. 4. Alternative circuit for Average detector

Apart from limited frequency range, the performance of the average value detector is limited by the current mismatch between the two detectors. The LHS in (3) and (4) are equal only if IDC is equal. Therefore, if there is a mismatch between IDC in the two average value detectors, VoutA and VoutB are not equal and hence 50% duty cycle cannot be assured at the output.

2.2. PROPOSED AVERAGE VALUE DETECTOR

The structure of the "Duty-alter" block is shown in Fig. 4. Output of the opamp is connected to the gate of the NMOS and the signal whose duty is to be corrected is connected to the gate of the PMOS as shown. The duty cycle of the signal produced at the output is inversely proportional to VErr (when is VErr>VThn). By changing the value of VErr, we can change the duty cycle of the output signal. Therefore, by the action of the feedback loop, VErr is adjusted such that 50% duty cycle is achieved.

3. SIMULATION RESULTS

In order to confirm the validity of the proposed ideas and to evaluate the performance, the duty correction circuit was implemented in TSMC 130nm technology

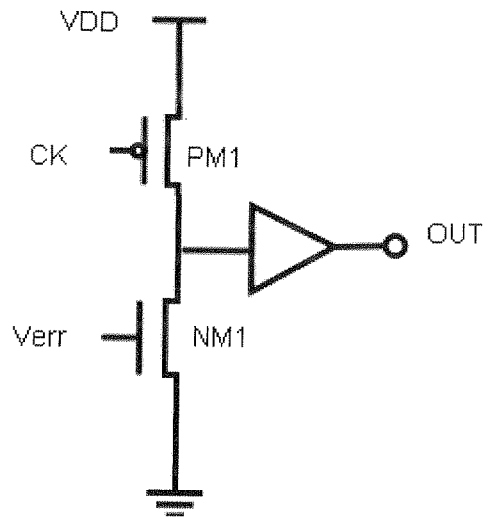

Fig. 5. Circuit for "Duty-alter" block

and simulated using BSIM3v3 models. Power supply voltage is 1.2V (typical). The input signal with various duty cycle values was given using a signal generator. The frequency of the signal was set to 500MHz. The circuit requires calibration (for R and C in the low pass filter) for very low frequency signals.

The circuit was tested across 3 corner conditions with 9 input duty conditions. The results have been summarized using the plots in Fig. 6. It can be observed from the figure that when the input duty cycle is varied +/50% (i.e. 25% to 75%) the output duty cycle varies by about +/-1%.

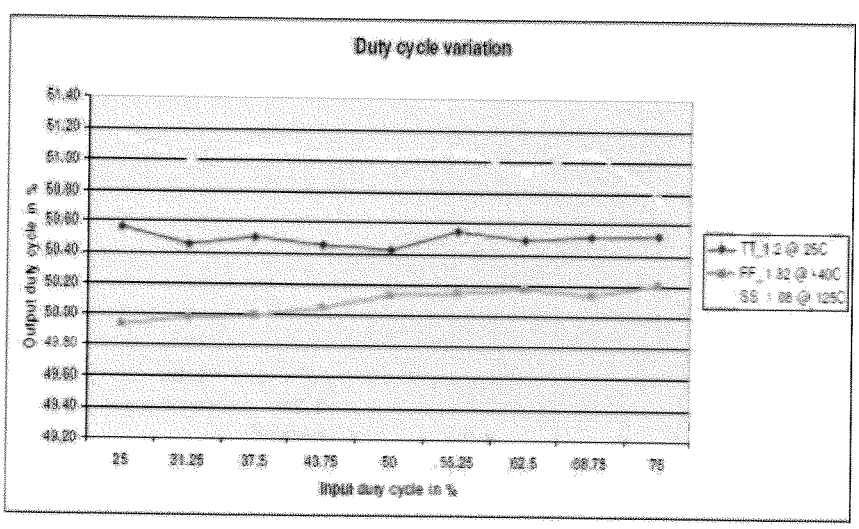

Fig. 6. Variation of output duty cycle

Fig. 7 shows the settling behavior of VoutA, VoutB and VErr at FF corner, 1.32 V and -40 C. It can be observed from the waveforms that there are no stability issues with the feedback loop.

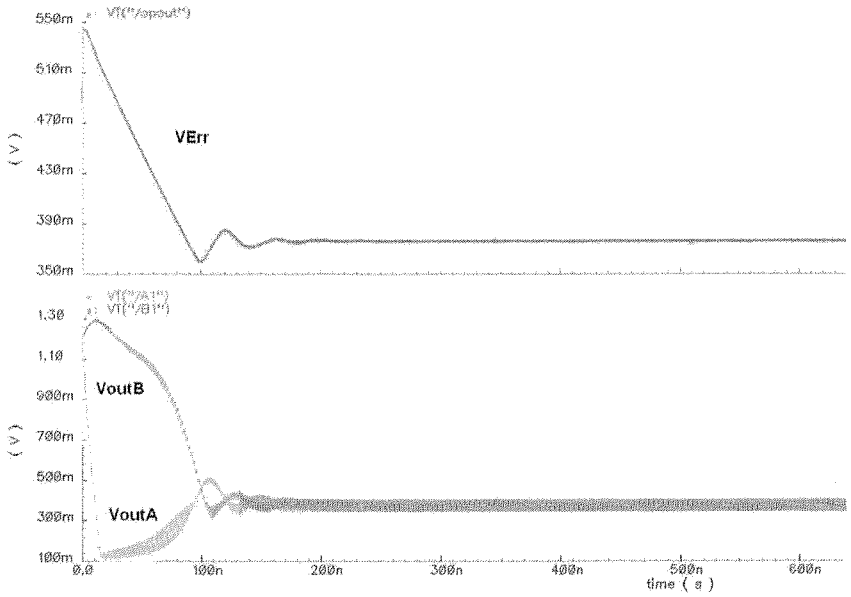

Fig. 7. Settling behavior of inputs and output to the opamp

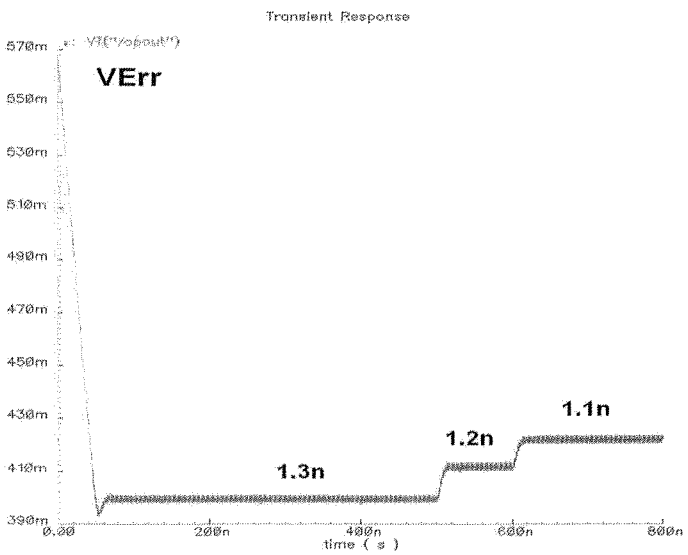

Fig. 8. Settling behavior of VErr for different input duty cycles

1.32 V issues

The circuit was tested by changing the duty cycle on the fly to check the response of the loop. The result is plotted in Fig. 8. We can observe that the control voltage VErr settles to a stable value within about 50 cycles. The figure shows the VErr waveform for input ON time of 1.3ns, 1.2ns and 1.1ns (i.e. for input duty of 65%, 60% and 55% respectively).

4. CONCLUSION

A duty cycle correction circuit has been proposed and demonstrated using analog blocks with a negative feedback loop. The circuit can be implemented using simple blocks as demonstrated, providing an output duty cycle of close to 50%. The performance of the circuit can be improved by modifying the "Duty-alter block" and the low pass filter. Future work includes modifying the "Duty-alter block" to make it more robust and reduce the current consumption. Also, the low pass filter uses bulky capacitors and resistors which can hopefully be replaced by more area-efficient implementations in the future.

REFERENCES

1. Keun-Soo Song, Cheul-Hee Koo, Nak-Kyu Park, Kwan-Weon Kim,Young-Jung Choi, Jin-Hong Ahn, Byong-Tae Chung: *A Single- Loop DLL Using an OR-AND Duty-Cycle Correction Technique*, Proceedings, IEEE Asian Solid-State Circuits Conference, Nov 2008
2. Kazuyuki Nakamura, Muneo Fukaishi, Yoshinori Hirota, Youetsu Nakazawa and Michio Yotsuyanagi: *A CMOS 50% Duty Cycle Repeater Using Complementary Phase Blending*, Symposium on VLSI Circuits Digest of Technical Papers. 2000

ELECTRONICS AND TELECOMMUNICATIONS QUARTERLY, 2009, 55, no 4, pp. 585–599

Co-Design Strategy Approach of LNA, Oscillator, and Mixer

J. P. OLIVEIRA, L. OLIVEIRA, J. FERREIRA, I. BASTOS, T. MICHALAK, P. PANKIEWICZ, B. NOWACKI, P. MAKOSA, A. RYBARCZYK

CTS – Centre of Technology and Systems UNINOVA / FCT /UNL, Portugal;
e-mail: jpao@fct.unl.pt
Chair of Computer Engineering, Poznan University of Technology, Poland;
e-mail: Andrzej.Rybarczyk@put.poznan.pl

Received 2009.09.21
Authorized 2009.11.09

A co-design strategy for the implementation of a low-voltage fully integrated CMOS receiver is presented. This co-design approach allows the design of a compact direct-conversion receiver by avoiding 50 Ω matching buffers and networks, and AC coupling capacitors between mixer inputs and LNA and oscillator outputs. Moreover, the proposed circuit does not require DC choke inductors for mixer biasing. Since a 1.2 V power supply is used, a current bleeding technique is applied in the LNA and in the mixer. To avoid inductors and obtain differential quadrature outputs, an RC two-integrator oscillator is employed, in which, a filtering technique is applied to reduce phase noise and distortion. The proposed receiver is designed and simulated in a 130 nm standard CMOS technology. The overall conversion voltage gain has a maximum of 35.8 dB and a noise figure below 6.2 dB.

Keywords: LNA, RC Oscillator, mixer, direct-conversion receiver, low–IF receiver, fully integrated CMOS receiver

1. INTRODUCTION

The direct conversion architecture, shown in Fig. 1, and low-IF architecture, shown in Fig. 2 are approaches to enable full integration of RF receivers in pure standard digital CMOS technology which is reaching higher transistor's cutoff frequencies ω_T. The success of these approaches is supported by its dissemination from high demanding 2G and 3G handsets to low data rate and low-power wireless sensors Networks (WSN) and INDUSTRIAL SCIENTIAL AND MEDICAL (ISM) applications.

Both, the direct conversion receiver (DCR) and the low-IF receiver techniques, allow significant reduction on the number of off-chip components, which means that

all the major building blocks will interconnect to each other inside the chip [1-3]. Therefore, the match between these internal interconnects at 50 Ω level is no longer required. This simple approach opens the design of highly integrated RF front-end with low area, low power, and low-cost implementation.

DCR and low-IF receivers require linear low noise amplifier (LNA) followed by a mixer that needs a high frequency local oscillator (LO) with precise quadrature outputs. Within these types of receivers, the conventional approach of designing independently these blocks is not longer suitable. Alternatively, a co-design methodology for adapting the mixer to the LNA and to the oscillator is required. All these requirements are difficult to fulfill simultaneously, and therefore, an optimized trade-off process should be followed.

This paper proposes a co-design strategy applied jointly to the LNA, mixer and to the local oscillator for applications in the sub-gigahertz band and with low to moderate data rate, which can be applied to direct or low-IF receivers.

The main objective of this co-design is to avoid matching buffers (in LNA and oscillator outputs), and directly connect to the mixer without using AC coupling capacitors and choke inductors. This co-design also allows the minimization of power consumption, which is an ongoing research work.

2. RF FRONT-END CONSIDERATIONS

In the homodyne receiver shown in Fig. 1, the RF spectrum is directly translated to the baseband by the complementary operation of the LNA, mixer and LO. The sub-gigahertz RF signal is first amplified by the LNA and then down-converted to zero-IF in-phase and quadrature (I/Q) signals by the composite mixer driven by quadrature LO signals. For DCR operation the LO has the same frequency of the input radio and I/Q signals are needed to separate the wanted channel from its mirror, which is accomplished by means of a Hilbert transform. As a consequence, this downconversion requires accurate quadrature signals generated by the LO [1, 2].

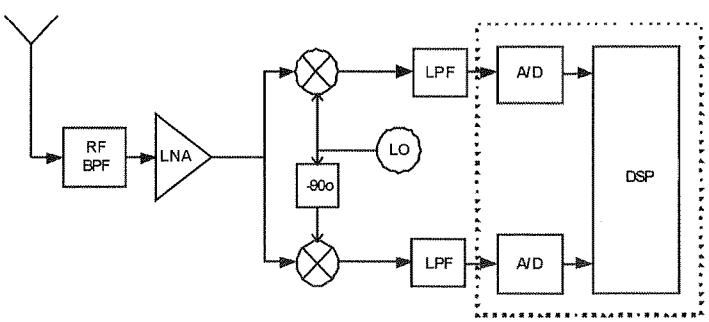

Fig. 1. Direct Conversion Receiver

Besides the previous requirements, the DCR architecture has several design issues to be addressed:

a) Flicker noise – the low frequency 1/f corner associated with standard MOS technology degrades the Signal-to-Noise ratio (SNR) at low frequency baseband signals. The major contribution at the output comes from the current commutating switching transistors of the mixer.

b) LO leakage – LO signal coupled to the antenna will be radiated again and re-injected to the mixer through the main signal path, originating unwanted baseband DC components.

c) Quadrature error – Quadrature error and amplitudes mismatches between the I and Q signals corrupt the downconverted signal constellation.

d) DC offsets – Since the downconverted band extends down to zero frequency, any offset voltage can corrupt the signal and saturate the receiver's baseband output stages. Hence, DC offset removal or cancellation is required in DCR.

The DCR approach removes the need for IF high-Q filters (reducing the receiver area and/or avoiding external components) which means that the LNA can be directly connected to the mixer. Moreover, since the input mixer impedance is essentially capacitive, the LNA output does not have to be matched to 50 Ω. Additionally, if a gate input type mixer is considered (meaning that it is driven by a voltage), it is the LNA voltage gain that should be considered.

It has been implicitly demonstrated that heterodyne receivers have important limitations due to the use of external image reject filters. But, DCR receivers have also some drawbacks, which degrade the signal translated directly to the baseband. Thus, there is interest in the development of new techniques to reject the image without using filters. An architecture, which combines the advantages of both the IF and the zero-IF receivers, is the low-IF architecture.

The low-IF receiver is a heterodyne receiver that uses special mixing circuits that cancel the image frequency, as shown in Fig. 2. A high quality image reject filter is not necessary anymore, while the disadvantages of the zero-IF receiver are avoided [3, 4].

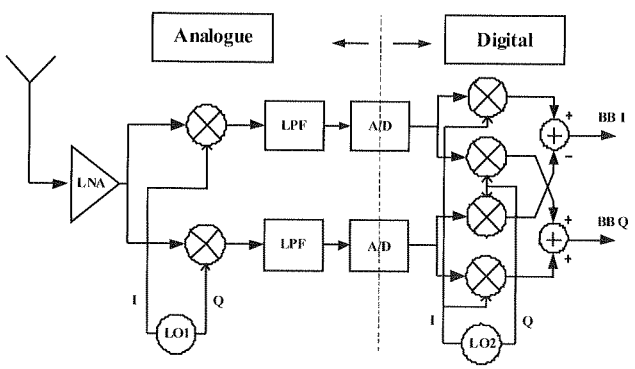

Fig. 2. Low-IF receiver (simplified block diagram)

The co-design strategy, proposed by this work, can be applied both for DCR or low-IF receivers.

3. RF FRONT-END KEY BLOCKS

3.1. LOW NOISE AMPLIFIER

The LNA topology, shown in Fig. 3, account for a source-degenerated effect around the input transconductance transistor M_1. This architecture is very common among narrowband LNA's as it is very close to achieving the goal of providing the input match and best noise performance simultaneously [1-4]. The cascode transistor (M_2) is used to reduce the effect of the gate-drain capacitance C_{gd} of the input transistor (M_1) and to increase the reverse isolation of the LNA. This improves the stability and makes the LNA's input impedance less sensitive to its load impedance. The number of integrated inductors is reduced to one, since L_S is implemented with the bonding wire and the output inductance L_D is replaced by a resistance. In order to avoid significant voltage drop at the output resistor a bleeding current is injected at the drain of M_1 preserving the value of the g_m of M_1, needed to maintain the input matching to 50 Ω.

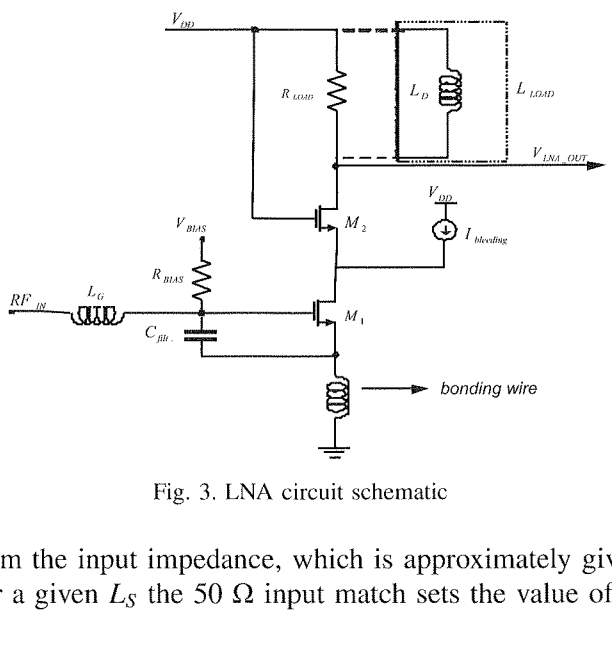

Fig. 3. LNA circuit schematic

It is clear from the input impedance, which is approximately given by (1), that at resonance and for a given L_S the 50 Ω input match sets the value of the transconductance gain.

$$Z_{in} = j\omega L_g + j\omega L_s + \frac{1}{j\omega\left(C_{filt} + C_{gs1}\right)} + \frac{g_{m1}L_s}{C_{filt} + C_{gs1}} \tag{1}$$

On the other hand, due to capacitive nature of the mixer input, an optimized value for the LNA voltage gain can be found by selecting an appropriate value of the output LNA load resistance.

Entering into account the effective transconductance gain at the resonance frequency, set by the input matching requirement, the LNA voltage gain in case of resistive load R_L is given approximately by:

$$|A_v| = G_{m,LNA} \cdot R_{out,LNA} \approx gm_{1,eff} \cdot R_L \tag{2}$$

The total LNA transconductance $G_{m,LNA}$ is approximately given by the effective transconducantce of M_1 if $1/g_{m2} << r_{out,M1}$. This effective transconductance also includes the degeneration effect due to L_s. The output LNA impedance is approximately given by R_L due the cascode configuration of M_1 and M_2 he value of R_L is the result of co-designing the LNA together with the mixer. The value of the 700 Ω guaranteed the best performance, from which a gain of 28 dB is achievable.

3.2. QUADRATURE LOCAL OSCILLATOR

The schematic of the two-integrator oscillator [5] is presented in Fig. 4. Each integrator is realized by a differential pair (transistors M) and a capacitor (C). The oscillator frequency is controlled by I_{tune}. There is an additional differential pair (transistors M_L), with the output cross-coupled to the inputs, which performs two related functions: a) compensation of the losses due to R to make the oscillation possible (a negative resistance is created in parallel with C); b) amplitude stabilization, due to the non-linearity (the current source I_{level} controls the amplitude). To start the oscillations the condition $g_m > 1/R$ must be met. Moreover, the I_{level} is used to control the output signals amplitude.

In order to obtain low distortion output, a filtering technique is used. To achieve this goal the extra capacitor C_{filter} is introduced to the terminals of the tuning current source I_{tune}. The introduction of this element reduced cancels the harmonics at this point and reduced the oscillator phase-noise.

The circuit of Fig. 4 can be represented by the linear model in Fig. 5, where the negative resistance is realized by the cross-coupled differential pair (M_L), and R represents the integrator losses due to the pairs of resistances R / 2.

The oscillator frequency varies by changing either the capacitance or the transconductance. In a practical circuit we can use varactors to change the capacitance or, most commonly, we can change the tuning current, and therefore, the transconductance.

These oscillators have wide tuning range with very precise inherent differential quadrature outputs (less than one degree quadrature error), which are required for very compact DCR and low-IF receivers [5].

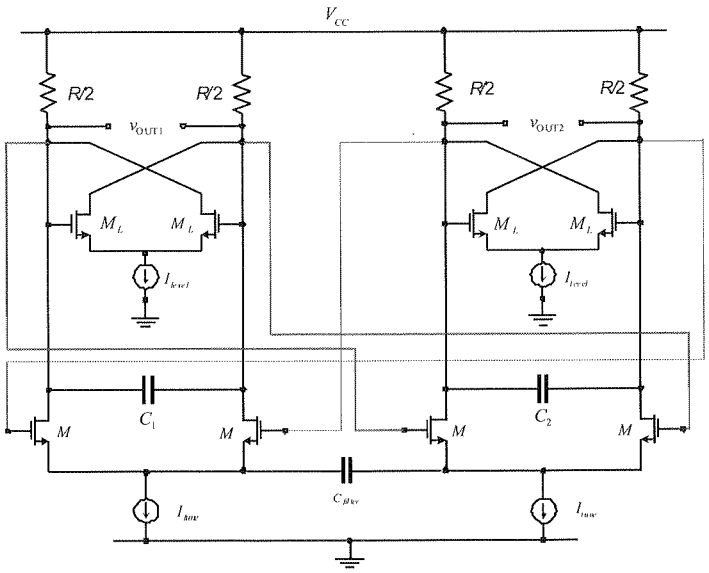

Fig. 4. Two-integrator schematic

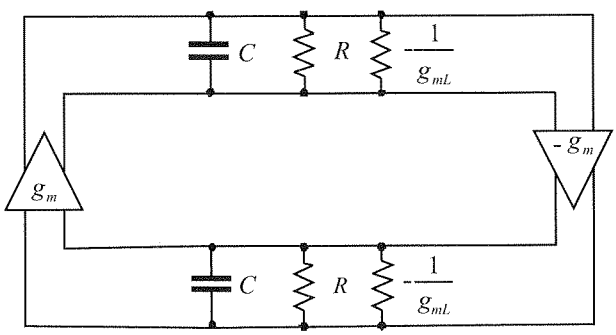

Fig. 5. Two-integrator linear model

3.3. MIXER

The I/Q mixer topology, shown in Fig. 6, is constructed around a double balanced Gilbert cell which needs accurate I/Q differential inputs from the LO. This differential mixer structure has higher conversion gain, lower noise figure, improved linearity, higher port-to-port isolation, higher spurious rejection, and lower even-order distortion, with respect to the singlebalanced mixer. The main disadvantage is the increased area (due to complexity) and power consumption but in order to save area and since the LNA output is single ended it has not been used a balun transformer to provide the RF differential at the mixer input [1-4].

Considering the high impedance mixer input, the LNA output can be directly AC connected to the mixer. Nevertheless, the LNA output DC component is important to bias the transconductance mixer stage, which controls the mixer conversion gain. Inside this transconductance mixer block, a minimum L is used, to maximize gain and speed, and the W is adjusted according to the DC voltage at the LNA output node. An additional current is injected into the mixer transconductance (formed by M_3 and M_4) to improve linearity and to set the conversion gain and noise figure. By adjusting this current, the DC output level from the LNA will have less impact on the mixer output voltage.

The mixing switching current commutating stage is formed by a couple of NMOS transistors pair, which are connected directly to the oscillator I/Q outputs. As in the previous stage, the oscillator AC output is connected directly to the mixer. The oscillator amplitude needs to be maximized to properly drive the mixer switching transistors and reduce the mixer output $1/f$ noise. Moreover, the oscillator output DC component is important to bias these switching pairs, and it will define their widths (since the L is kept at minimum value).

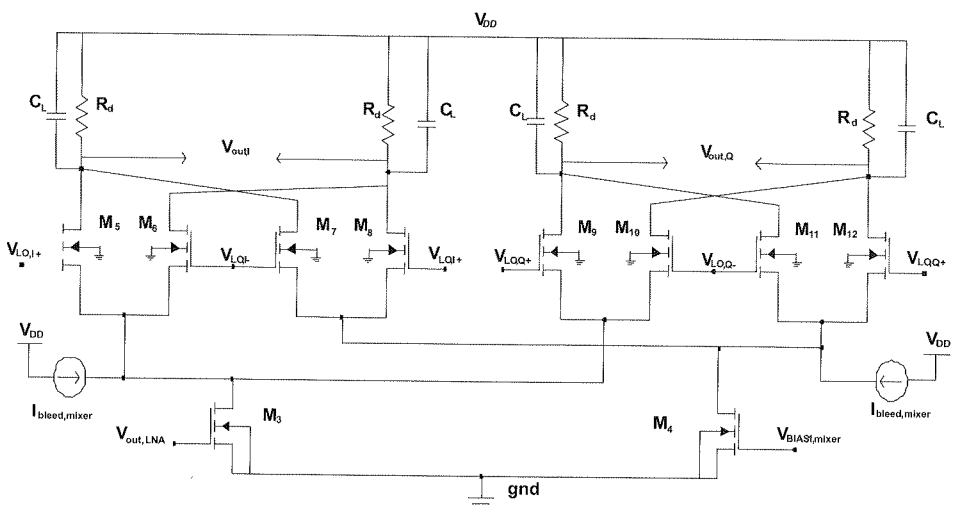

Fig. 6. Mixer circuit

3.4. CO-DESIGN STRATEGY

The co-design of the LNA, oscillator and mixer facilitates the optimization process to reach better tradeoff between conversion gain and noise figure. Another objective of this co-design is to avoid 50 Ω matching buffers and AC coupling capacitors. LNA and mixer merged topologies have been proposed in literature [6], but in our design a cascaded structure was chosen. This topology can achieve higher gain and better noise figure since the noise contribution of the mixer can be substantially suppressed

by the high voltage gain of the LNA. In this work we propose that the mixer should be co-designed with both the LNA and LO.

The design process begins by maximizing the LNA voltage gain for a given input match criteria (50 Ω in this case). By its turn the oscillator is designed to maximize the signal output swing voltage and improve the I/Q signals accuracy for a given power. With the obtained DC components at the output of these blocks, the mixer is then optimized to reach a reasonable conversion gain and noise figure. In order to reduce the total area, the design must remove as much as possible the use of inductors and AC coupling capacitors.

The co-design example presented in this work will reduce the total circuit area allowing the design of a low cost compact receiver.

The main objective of this work is the co-design between the LNA, LO and mixer in order to avoid 50 Ω matching buffers and AC coupling capacitors.

4. SIMULATION RESULTS

To validate the proposed design strategy, a LNA, mixer, and quadrature oscillator have been co-designed and simulated in a 130 nm CMOS technology with 1.2 V power supply. Two cases have been considered by varying the LNA gain from a high value, for improved sensitivity, to a reduced one, for improved receiver linearity under strong received signals.

4.1. RECEIVER WITH HIGH LNA GAIN

Beginning with a traditional inductive load of 27 nH inductor (one of the maximum available values for the chosen technology), a gain of 15 dB and a noise figure of 2.7 dB at 900 MHz are achieved. Replacing this inductor by a 700 Ω resistor (this can not be higher due to power supply headroom), the voltage gain and noise figure change, respectively, to 28 dB and 2.24 dB while maintaining the power consumption below 9 mW.

Concerning the RC two-integrator oscillator, Tab. 1 shows the effect of the capacitive filtering technique to reduce phase noise and distortion.

Table 1

RC Oscillator Simulation Results

Case	*Phase-noise @ 10MHz offset* [dBc/Hz]	*THD* [dB]	P_D [mw]
I : without C_{filter}	−111.0	−31.3	4.8
II : with C_{filter}	−112.6	−30.8	5.2
III: with C_{filter} optimized for THD	−120.0	−43.5	8.6

In comparison to case I, the simulations results from case II show that the introduction of a filtering capacitor C_{filter} generates a phase noise improvement of 1.6 dB but with a drop in output signal magnitude. Therefore, to achieve the desired amplitude and frequency, the current values have to be increased, and, the power consumption rises slightly. In case III, I_{tune} and I_{level} currents were further increased leading to better phase-noise and lower THD but followed by the corresponding increase of the circuit consumption.

The final values in the designed oscillator are: R = 314 Ω, (W/L) = 15 μm / 0.255 μm for M transistors, W/L = 10.8 μm / 0.255 μm for M_L transistors, C_{filter} = 217 fF (for cases I and II) and C_{filter} = 430 fF (for case III). The oscillator differential output amplitude is 290 mV @ 900 MHz.

The final values in the designed mixer are: R_L = 800 Ω, C_L = 2.5 pF, (W/L) = 100 μm/ 0.13 μm for the switching stage transistors, (W/L) = 30 μm / 0.13 μm for the RF stage transistors, and $I_{bled,mixer}$ = 4.15 mA.

In Figs. 7 to 11 simulations' results are presented for the completed front-end obtained from SpectreRF simulator, using BSIM3V3 models, including noise and linearity performance.

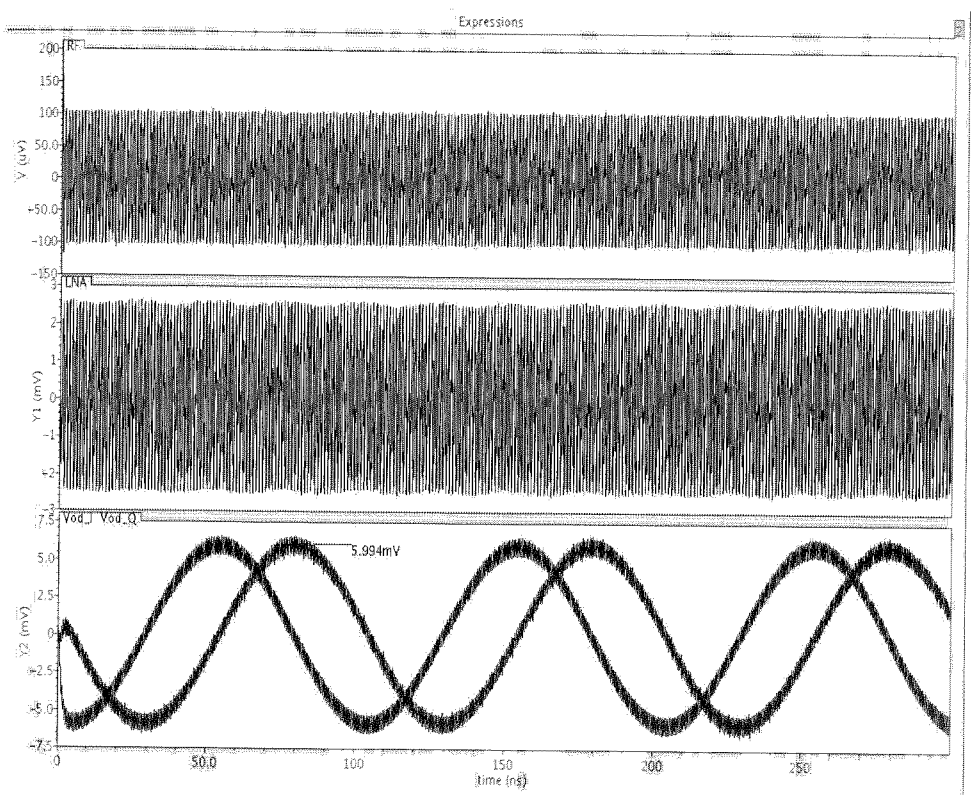

Fig. 7. LNA and Mixer simulated waveforms

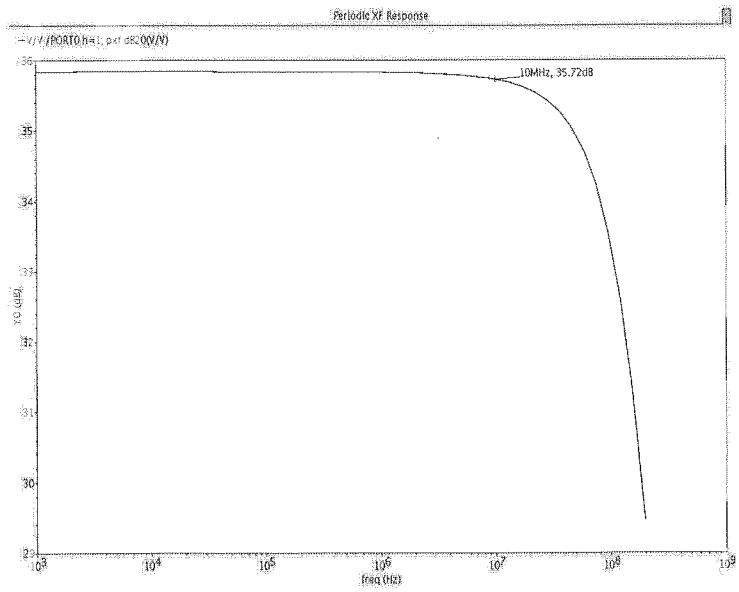

Fig. 8. Total conversion gain

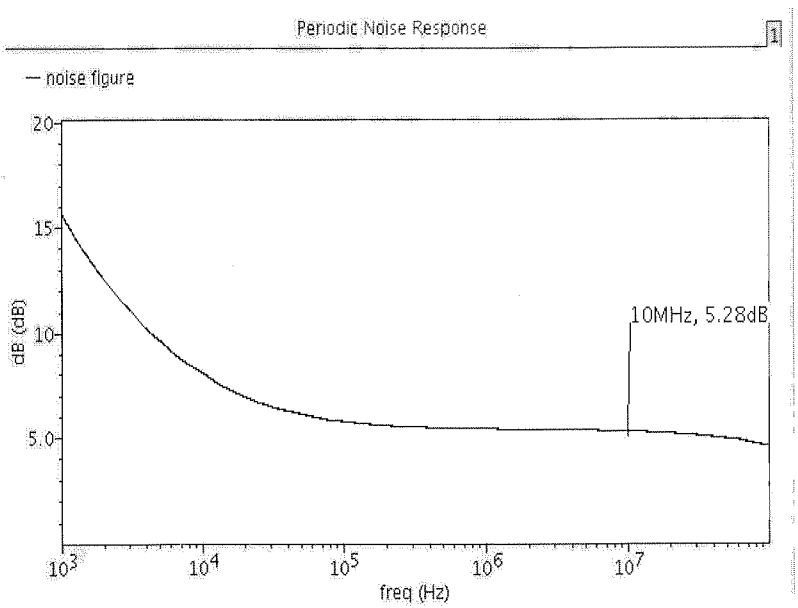

Fig. 9. Noise figure for the RF front-end

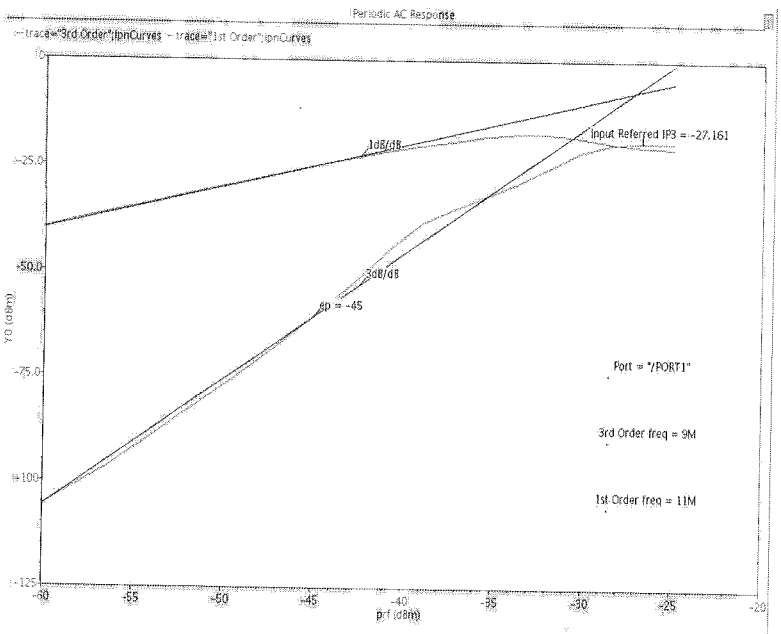

Fig. 10. IIP3

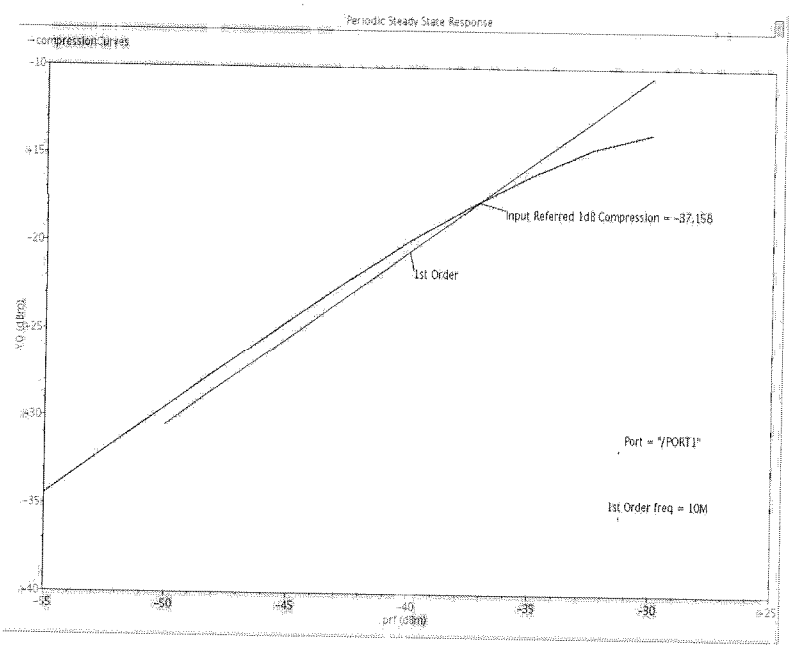

Fig. 11. 1dB Compression Point

4.2. RECEIVER WITH LOW LNA GAIN

In order to improve linearity, the LNA gain is reduced by removing the bleeding current and adjusting the resistive load R_L (from 700 Ω to 72 Ω) to meet the same DC output (thus, keeping the Mixer and LO unchanged). Table 2 shows the simulation results obtained for this low LNA gain design, and a comparison with the previous design.

The objective of these two designs is the following: in a complete receiver an RSSI block checks the amplitude at the output of the mixer and adjust the LNA gain in order to avoid the saturation of the amplifiers' blocks. Thus, the gain of the LNA has at least two possible gains: a high value if we have a very low input signal; and a low value in the presence of a strong input signal (e.g., close to the transmitter antenna). In both cases, the noise figure (NF) and conversion gain (CG) results were obtained from SpectreRF simulator, using BSIM3v3 with the complete front-end, models, including noise.

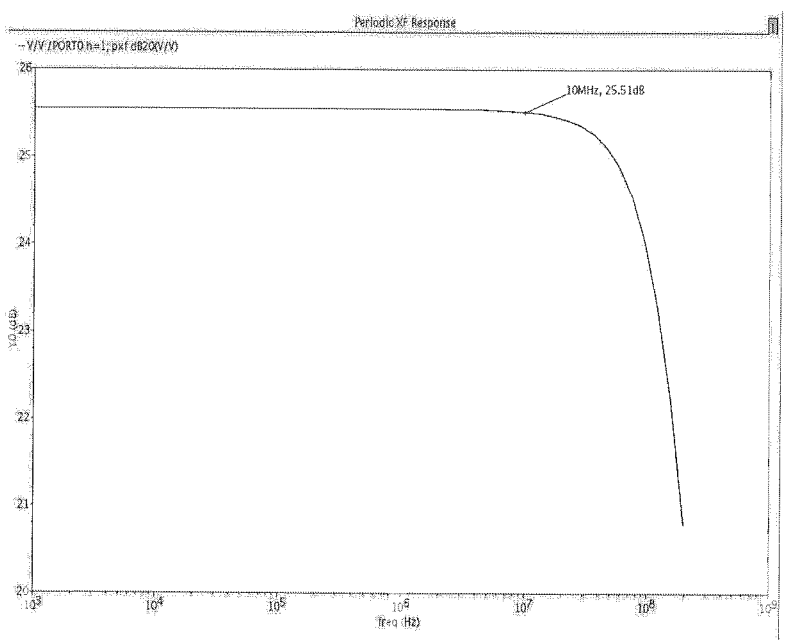

Fig. 12. Total conversion gain

Table 2

FRONT-END RESULTS (@ 10 MHz)

Parameter	High LNA Gain (#1)	Low LNA Gain (#2)
NF	5.28 dB	6.16 dB
CG	35.7 dB	25.5 dB
IIP3	−27.16 dBm	−17.33 dBm
1dB Compression Point	−37.16 dBm	−28.95 dBm

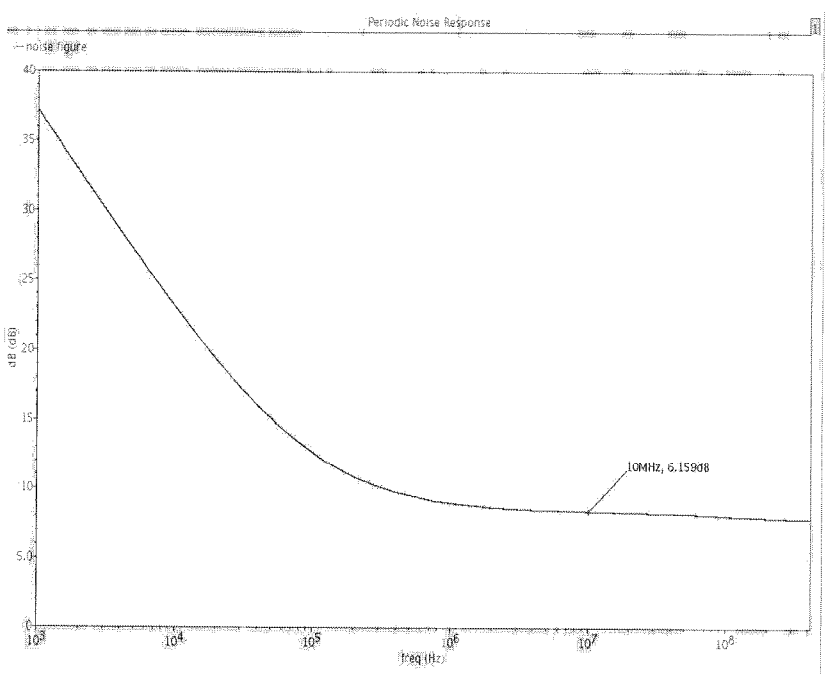

Fig. 13. Noise figure for the RF front-end

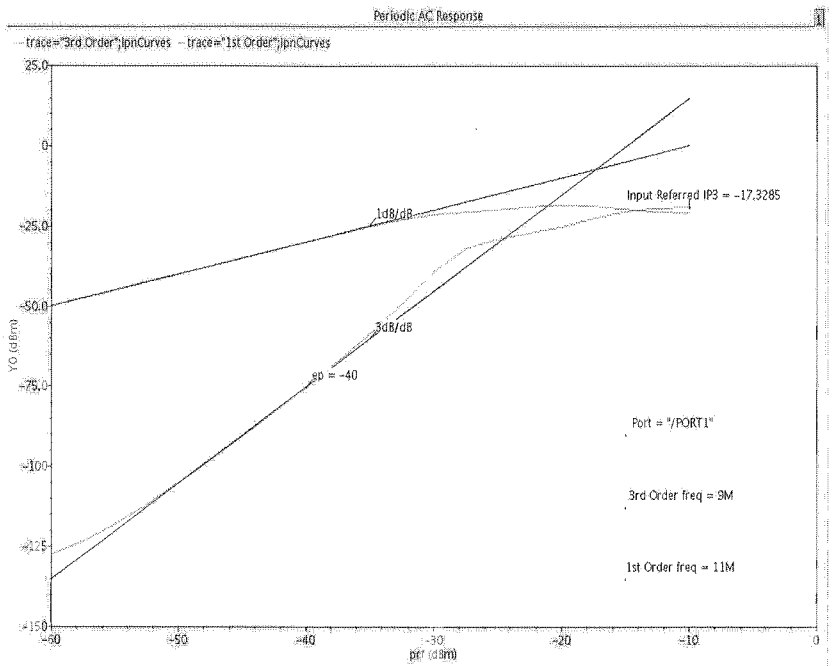

Fig. 14. IIP3

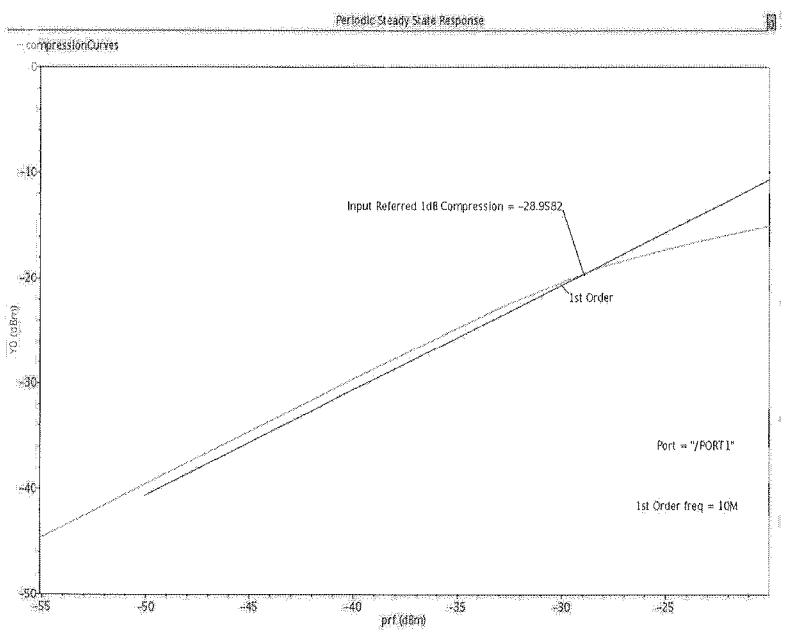

Fig. 15. 1dB Compression Point

5. DISCUSSION AND CONCLUSIONS

In this paper, a co-design strategy for the implementation of a low-voltage, low-area, and low-cost, fully integrated CMOS receiver was presented. This approach avoids 50 Ω matching buffers and networks, AC coupling capacitors, and DC choke inductors.

We present a resistive load LNA, with 700 Ω load, and an inductorless differential RC quadrature oscillator, which are combined with a mixer in a co-design strategy. A current bleeding technique is applied to the LNA and mixer, due to the low power supply voltage. The low area quadrature two-integrator oscillator uses a capacitive filtering technique, which reduces the oscillator phase-noise and the harmonic distortion.

The circuit in this paper has only one inductor, allowing the design of a very compact and low-cost receiver (DCR or low-IF), suitable for low data rates ISM applications.

The proposed receiver was designed and simulated with UMC 130 nm CMOS technology. The total conversion voltage gain has a maximum of 35.8 dB and the cascade noise factor has a minimum of 5.3 dB for the band of interest.

6. ACKNOWLEDGMENT

This work was supported by the Portuguese Foundation for Science and Technology (FCT) through funding of CTS-UNINOVA and project LEADER (PTDC/EEA-ELC/69791/2006).

REFERENCES

1. B. Razavi: *RF Microelectronics*, Prentice-Hall, 1998
2. T. H. Lee: *The Design of CMOS Radio Frequency Integrated Circuits (2nd edition)*, Cambridge University Press, 2004
3. J. Crols and M. Steyaert: *A Single-Chip 900 MHz CMOS Receiver Front-end with High Performance Low-IF Topology*, IEEE J. Solid-State Circuits, vol. 30, no. 12, pp. 1483–1492, December 1995
4. J. Crols and M. Steyaert: *CMOS Wireless Transceiver Design*, Kluwer, 1997
5. L. Oliveira, J. Fernandes, I. Filanovsky, C. Verhoeven, M. Silva: *Analysis and Design of Quadrature Oscillators*, Springer: Analog Circuits and Signal Processing 2008
6. H. Sjoland, A. Karimi, and A. A. Abidi: *A Merged CMOS LNA and Mixer For a WCDMA Recevier*, IEEE J. Solid-State Circuits, vol. 38, no. 6, pp. 1045–1050, 2003

ELECTRONICS AND TELECOMMUNICATIONS QUARTERLY, 2009, 55, no 4, pp. 601–616

Wide Tuning Range Quadrature VCO Using Coupled Multivibrators

IGOR M. FILANOVSKY*, LUIS B. OLIVEIRA**, JORGE R. FERNANDES***

*University of Alberta, Edmonton, Alberta, Canada
** Universidade Nova de Lisboa / INESC-ID, Monte da Caparica, Portugal
*** INESC-ID / TU Lisbon , Lisboa, Portugal
e-mail: igor@ece.ualberta.ca, l.oliveira@fct.unl.pt, jorge.fernandes@inesc-id.pt

Received 2009.09.21
Authorized 2009.11.09

Two emitter-coupled multivibrators are coupled to produce a quadrature current-/voltage controlled oscillator with wide frequency tuning range (which can be wider than one decade). The tuning range, the achievable frequency of oscillation, and the synchronization transients are investigated by simulation. The influence of mismatches of timing capacitors and charging currents on synchronization is also investigated. The results of simulations for different couplings show that one can find a design with low quadrature error, low phase noise and wide tuning range. This confirms the potential of the proposed VCO for RF applications.

Keywords: Emitter-coupled multivibrators, quadrature VCO oscillators, wide tuning range, RC Oscillators

1. INTRODUCTION

Emitter- and source-coupled multivibrators are used frequently as voltage-controlled oscillators, phase-locked loops being a typical example [1]. Recently [2, 3], the transition of these circuits from sinusoidal to relaxation oscillations was investigated. These multivibrators can be coupled [4] to produce quadrature oscillators.

When the bipolar technology was dominant, the investigation of emitter-coupled multivibrators resulted in circuits of high precision and wide tuning range [5]. With emergence of ubiquitous CMOS technology these results were nearly forgotten. Yet, the access to the BiCMOS SiGe bipolar technology makes it possible to return to these previous achievements, and allows one to develop them even further.

The circuit shown in Fig. 1 (a) was widely used as bipolar current-controlled or voltage-controlled oscillators (CCOs or VCOs) [5]. This circuit was well investigated [5, 6]; the oscillation frequency, in the first approximation, is [1]

$$f_0 \approx \frac{I}{4V_{BE(ON)}C} \tag{1}$$

where $V_{BE(ON)} \approx 0.7$ V is the voltage drop on the diode-connected transistor D. The circuit has frequency tuning range up to four decades [5], but it was never used as a component of a quadrature oscillator. We present here a modification that preserves the wide tuning range, allows higher oscillation frequencies and, at the same time, allows one to couple two modified circuits in a quadrature oscillator.

This modification is shown in Fig. 1 b). The emitter followers are now connected to the taps of the resistances connected in parallel with the diodes. This reduces the voltage amplitude at the timing capacitor, and allows higher oscillation frequencies. The oscillation frequency is now

$$f_0 \approx \frac{I}{4V_{R1}C} \tag{2}$$

where $V_{R1} = V_{BE(ON)}\dfrac{R_1}{R_1 + R_2} < 0.7\text{V}$.

To obtain a quadrature oscillator one couples two such oscillators using differential pairs [6]. The inputs of the coupling differential pairs should be connected to the timing capacitors (at A and A_1). Their outputs can be connected to the collectors E and E_1, which is called here the soft synchronization coupling (designated as "soft", for brevity, in the captions). They also can be connected to the base divider taps B and B_1, which we call rigid synchronization coupling, designated as "rigid".

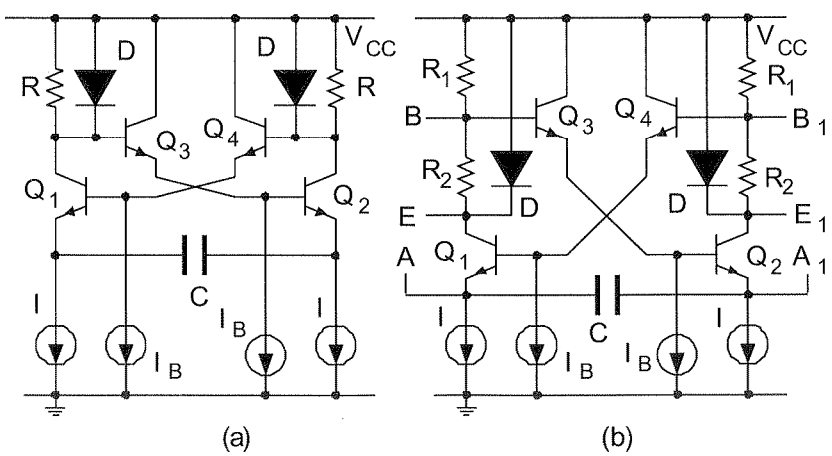

Fig. 1. Current-controlled oscillator (a) and its modification (b)

Section II describes the implementation of the quadrature oscillator. Section III gives simulation results for static and dynamic characteristics of this oscillator, namely, the tuning range and its dependence on the coupling current, and the phase error transient. The influences of the timing capacitance and tuning current mismatches are also evaluated. Finally, a discussion and some conclusions are given in Section IV.

2. CROSS-COUPLED QUADRATURE OSCILLATOR

To obtain a quadrature oscillator one connects two similar oscillators using two coupling differential pairs. Fig. 2 shows the first, "soft synchronization" connection. The synchronization mechanism is similar to that described for the coupled multivibrators with a fixed oscillation frequency [7]: the coupling current changes the base potential of Q_3 and Q_4, and this change is transmitted to the main transistors Q_1 and Q_2. In the soft coupling the change is "softened" by shunting effect of the diodes; in the rigid coupling this shunting is reduced.

If the coupling current is small in comparison to the tuning current, its influence on the oscillation frequency is very weak (except at very high frequencies, see Section III). Yet, this current is able to change the switching time of transistors Q_1 and Q_2 (increasing or decreasing it), and this leads to synchronous oscillation of the two multivibrators. The synchronous frequency can be approximately calculated using (2).

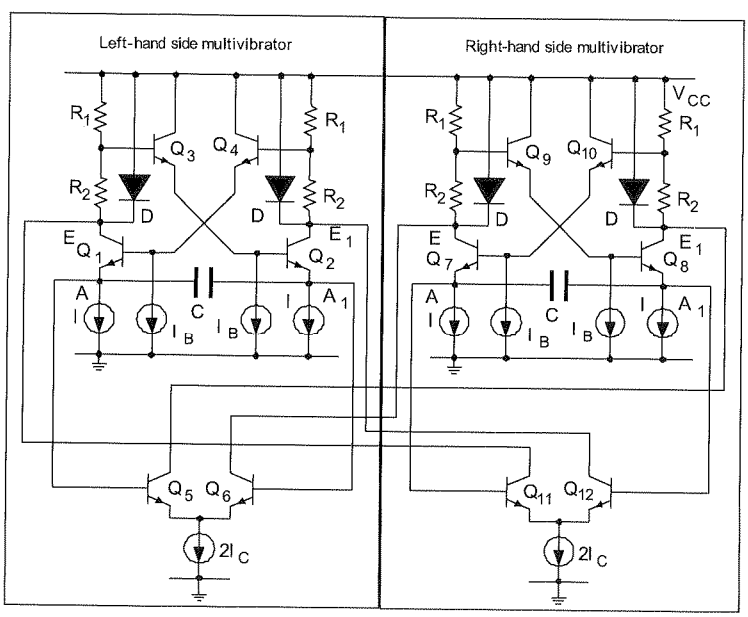

Fig. 2. Quadrature current-controlled oscillator (soft coupling)

3. SIMULATION RESULTS

The oscillator of Fig. 2 was designed and simulated with 0.35 μm AMS BiCMOS SiGe technology. The basic circuit parameters are: tuning current I = 1mA, coupling current $2I_C$ = 20μA, timing capacitance C = 20pF, and $R_1 = R_2 = R$ = 5kΩ.

The oscillator characteristics given in this section are obtained by changing one (tuning or coupling) or both of these currents and the timing capacitor. The follower bias current is I_B = 1mA. The diodes are realized as diode-connected transistors. The supply voltage is 3.3 V. The simulations reported in this section are given for the voltages taken between the collectors of Q_1 and Q_2 for the "soft" and between the bases of Q_3 and Q_4 for the "rigid" coupling.

Fig. 3 shows the oscillator tuning characteristics. They are similar for both couplings. For I_B below 1 mA the characteristics are approximately linear. The deviation from linearity at the high frequency end is due to the increasing influence of parasitic capacitances of the diode and voltage divider. The linear tuning zone at low tuning currents is limited by the chosen coupling current. The linearity of the tuning characteristic requires that the oscillation period does not depend on the switching times of Q_1 and Q_2 (these should be negligible) [5]. Yet, at very low tuning currents these switching times depend both on the tuning and coupling currents; it becomes a sizeable fraction of the oscillation period, and the linearity of the tuning characteristics is also lost.

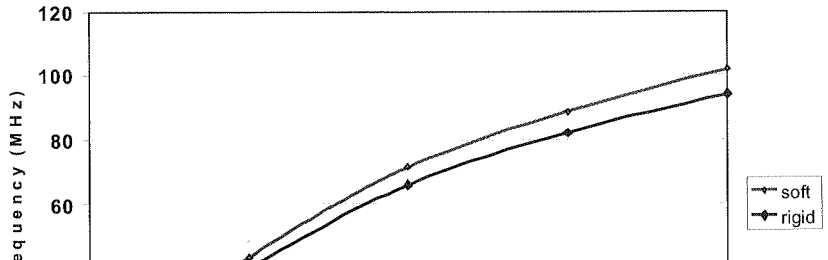

Fig. 3. Tuning characteristic for $2I_C$ = 20 μA

The region of linear tuning at the lower end of the tuning characteristic may be increased when the value of the coupling current is reduced. Yet, this reduction requires a longer synchronization time (larger number of periods to arrive at a given

phase error). The dependence of this time, for steady state error less than 1 degree is shown in Fig. 4 (again, the results are not very much different for both coupling cases).

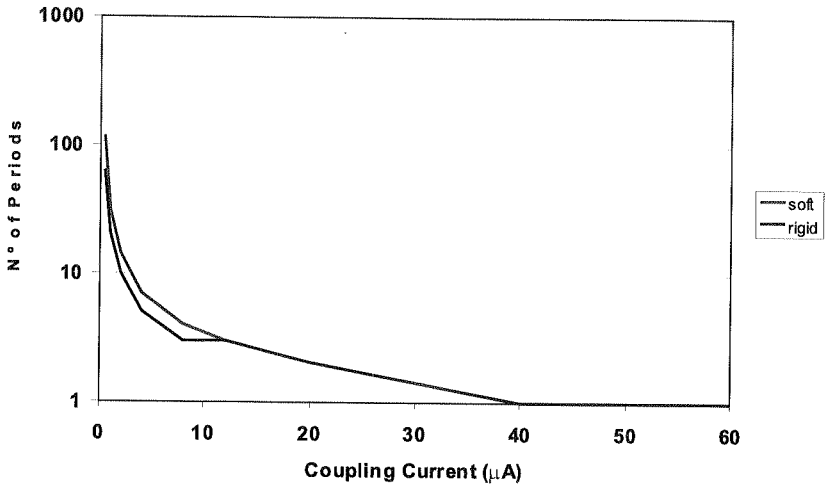

Fig. 4. Number of periods to set the quadrature oscillations for I = 1 mA

The approximately linear part of the tuning range can be moved to higher frequencies; this is achieved by the combined change of the oscillator parameters. First, the C value should be reduced (for both coupling cases), but stable operation requires that the value of C should be three to four times larger than the base-emitter capacitance of the transistors. Second, the resistances in the divider should be decreased, which requires the increase of both tuning and coupling currents. The increase of coupling current is necessary to shorten the switching time of Q_1 and Q_2, but this means that the tuning characteristics linearity is lost at the lower end of the tuning range. Fig. 5 shows the result of these combined changes in the basic parameters. Fig. 5 is obtained for C = 250fF, $R_1 = R_2 = R$ = 500Ω and with 2 I_C increased to 1mA. These modifications make the switching faster, and allow higher oscillation frequencies. We may notice that the transition from "soft" to "rigid" coupling reduces the tuning range, but makes it controllable for higher frequencies. Hence, the choice of the resistive divider ratio can be considered as compromise between tuning range and controllability range. The operation of each multivibrator is closer now to switching of the flip-flop consisting of two transconductance amplifiers with positive feedback. For small timing capacitor values the operation of individual multivibrators is closer to the sinusoidal regime [3], and the operation of the oscillator is similar to the behavior of two actively coupled sinusoidal oscillators.

Figs. 6 and 7 give samples of the output waveforms for the tuning range represented in Fig. 5. The quadrature operation is preserved, yet the rectangular shape is deteriorated.

The oscillator phase-noise characteristics are shown in Figs. 8 and 9. The phase-noise is about -106 dBc/Hz for "soft" and -110 dBc/Hz for "rigid" coupling @ 10 MHz offset.

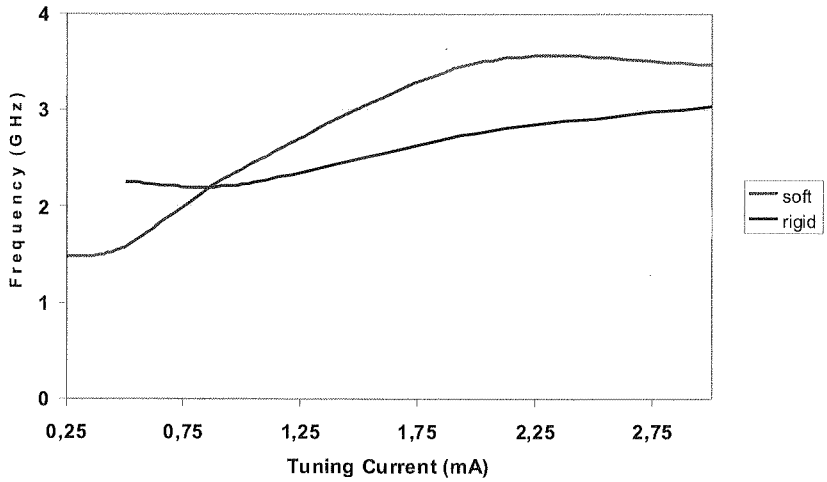

Fig. 5. Tuning characteristic for 2 I_C = 1 mA

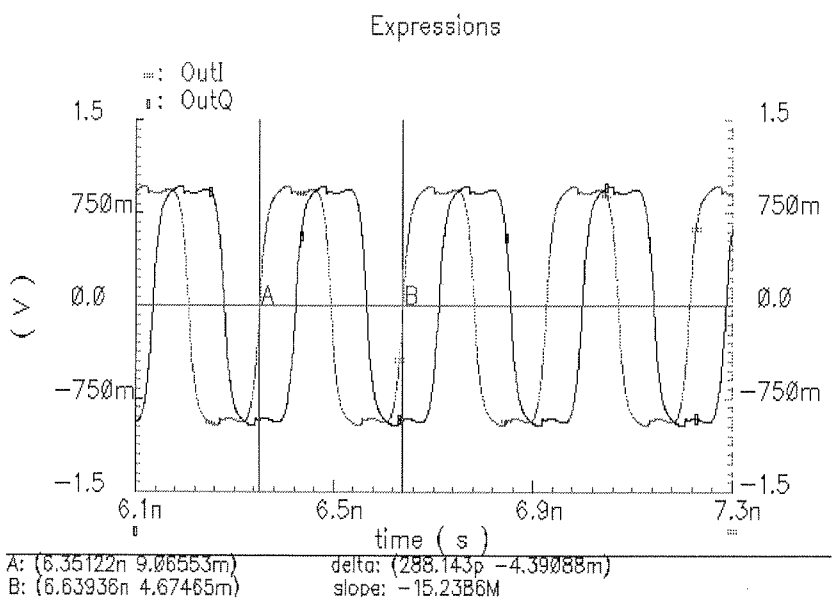

Fig. 6. Output waveforms ("soft" coupling)

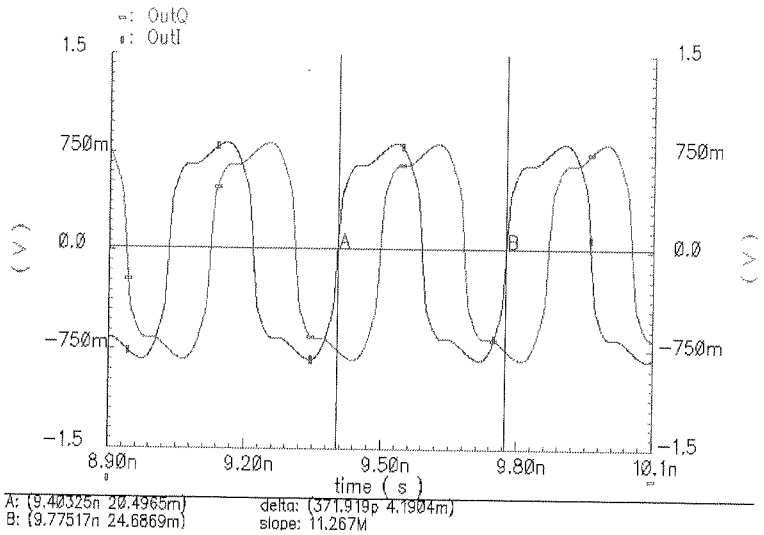

Fig. 7. Output waveforms ("rigid" coupling)

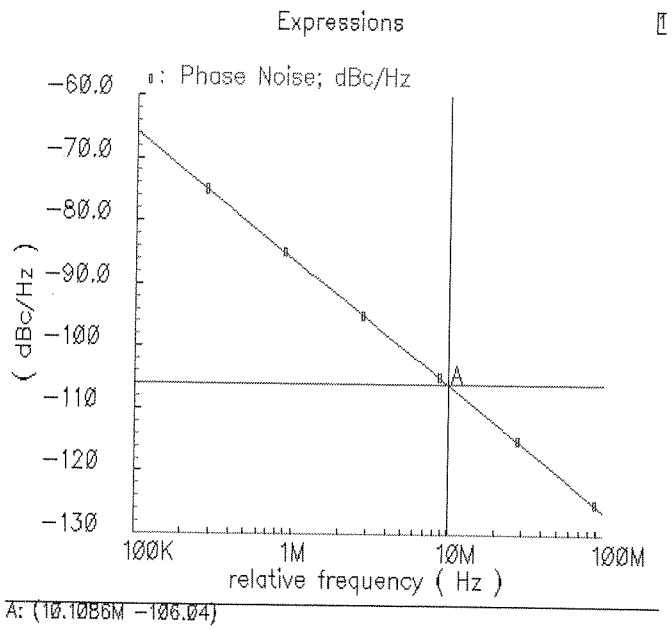

Fig. 8. Oscillator phase-noise ("soft" coupling)

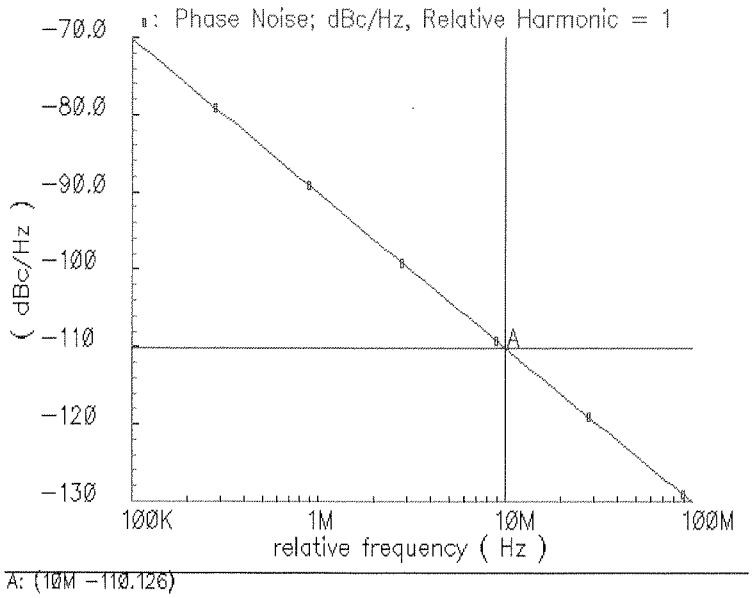

Fig. 9. Oscillator phase-noise ("rigid" coupling)

Some additional features of the oscillator are described by the following tables. The data in these tables were obtained using the parameters values of Section 2.

Table 1

Effect of 5% Mismatches in Capacitances ("Soft")

$2\ I_C$ (μA)	N°periods to lock	Frequency (MHz)	Phase error (°)
0.5	no lock	–	–
1	no lock	–	–
2	23	41	35.7
4	12	41.2	22
8	7	41.5	10.1
12	5	41.8	6.4
20	3	42.9	4.2
30	3	44.4	2.8
40	3	46.1	2.1
50	3	47.8	1.6
60	3	50.0	1.3
70	no oscillation		

Tables 1 to 3 and 4 to 6 show the influence of mismatches in the timing capacitance values for "soft" and "rigid" coupling, respectively. When this mismatch is present the

locking is lost for very low values of coupling current. Notice that the rigid coupling provides less phase error than the "soft" coupling.

Table 2

EFFECT OF 10% MISMATCHES IN CAPACITANCES ("SOFT")

$2\ I_C$ (μA)	N°periods to lock	Frequency (MHz)	Phase error (°)
0.5	no lock	–	–
1	no lock	–	–
2	no lock	–	–
4	no lock	–	–
8	8	41.2	21.1
12	5	41.5	13.1
20	3	42.4	7.6
30	3	43.9	4.7
40	3	45.5	3.4
50	3	47.3	3.1
60	3	49.4	2.5
70	no oscillation		

Table 3

EFFECT OF 20% MISMATCHES IN CAPACITANCES ("SOFT")

$2\ I_C$ (μA)	N°periods to lock	Frequency (MHz)	Phase error (°)
0.5	no lock	–	–
1	no lock	–	–
2	no lock	–	–
4	no lock	–	–
8	no lock	–	–
12	7	41.2	30
20	3	41.8	15.4
30	3	43.0	9.8
40	3	44.5	7.5
50	3	46.4	6.1
60	3	48.4	5.2
70	no oscillation	–	–

Table 4

EFFECT OF 5% MISMATCHES IN CAPACITANCES ("RIGID")

$2\ I_C$ (μA)	N°periods to lock	Frequency (MHz)	Phase error (°)
0.5	no lock	–	–
1	no lock	–	–
2	19	40.5	29.5
4	7	40.2	11.2
8	4	39.8	5.2
12	3	39.5	3.3
20	3	39.2	2.1
30	3	39.1	1.3
40	3	39.0	0.9
50	3	39.0	0.9
60	3	39.2	0.7
70	3	39.4	0.6
80	3	39.7	0.5
90	3	40.1	0.4
100	3	40.5	0.4

Table 5

EFFECT OF 10% MISMATCHES IN CAPACITANCES ("RIGID")

$2\ I_C$ (μA)	N°periods to lock	Frequency (MHz)	Phase error (°)
0.5	no lock	–	–
1	no lock	–	–
2	no lock	–	–
4	14	39.9	28.0
8	4	39.3	10.6
12	3	39.0	6.8
20	3	38.6	3.9
30	3	38.4	2.6
40	3	38.3	2.0
50	3	38.4	1.7
60	3	38.6	1.4
70	3	38.8	1.2
80	3	39.1	1.1
90	3	39.5	1.0
100	3	39.9	0.9
110	3	40.4	0.8
120	3	40.9	0.7
130	3	41.5	0.6
140	3	42.1	0.5
150	3	42.7	0.4

A
operati
reduced
Besides
and Q_2
reduced
Tab
currents

Table 6

EFFECT OF 20% MISMATCHES IN CAPACITANCES ("RIGID")

$2\,I_C$ (μA)	N°periods to lock	Frequency (MHz)	Phase error (°)
0.5	no lock	–	–
1	no lock	–	–
2	no lock	–	–
4	no lock	–	–
8	7	38.8	24.9
12	3	38.3	13.7
20	3	37.8	7.7
30	3	37.5	5.1
40	3	37.4	3.8
50	3	37.5	3.0
60	3	37.6	2.5
70	3	37.9	2.2
80	3	38.2	2.0
90	3	38.6	1.9
100	3	39.0	1.6
110	3	39.5	1.5
120	3	40.1	1.4
130	3	40.7	1.3
140	3	41.3	1.3
150	3	41.9	1.2
160	3	42.7	1.2
170	3	43.5	1.1
180	3	44.4	1.1
190	3	45.2	1.0
200	3	46.2	1.0

A larger mismatch requires a larger coupling current to establish synchronous operation (locking), but it leads to a much increased phase error. This error may be reduced by further increasing the coupling current, but it influences the frequency. Besides, the voltage drop $2I_CR_1$ reduces the voltage range for switching transistors Q_1 and Q_2 (this explains the increase of the oscillation frequency), and when this range is reduced to zero (i. e. when $2I_C(R_1 + R_2) \approx 0.7$ V) the multivibrators stop to oscillate.

Tables 7 to 12 show that the coupling current should be increased when the tuning currents are mismatched, but the same limitation as above applies: the phase error is

reduced with increase of the coupling current, but the circuit stops to oscillate when this increase does not leave any room for change of the base voltages of Q_1 and Q_2. Notice that for the timing current mismatch the phase error is also lower for "rigid" than for "soft" coupling.

Table 7

EFFECT OF 5% MISMATCHES IN TUNING CURRENTS ("SOFT")

$2\ I_C$ (μA)	N°periods to lock	Frequency (MHz)	Phase error (°)
0.5	no lock	–	–
1	no lock	–	–
2	15	40.9	48.7
4	9	41.1	20.3
8	6	41.5	9.7
12	4	41.9	6.5
20	3	42.9	3.9
30	3	44.4	2.6
40	3	46.1	2.0
50	3	48.0	1.6
60	3	50.2	1.4
70	no oscillation	–	–

Table 8

EFFECT OF 10% MISMATCHES IN TUNING CURRENTS ("SOFT")

$2\ I_C$ (μA)	N°periods to lock	Frequency (MHz)	Phase error (°)
0.5	no lock	–	–
1	no lock	–	–
2	no lock	–	–
4	no lock	–	–
8	8	41.2	20.9
12	5	41.5	13.3
20	3	42.4	7.9
30	3	43.8	5.3
40	3	45.5	4.1
50	3	47.4	3.4
60	3	49.5	2.8
70	no oscillation	–	–

Table 9

EFFECT OF 20% MISMATCHES IN TUNING CURRENTS ("SOFT")

$2\,I_C$ (μA)	N°periods to lock	Frequency (MHz)	Phase error (°)
0.5	no lock	–	–
1	no lock	–	–
2	no lock	–	–
4	no lock	–	–
8	no lock	–	–
12	4	41.1	32.4
20	3	41.8	16.6
30	3	43.0	11.1
40	3	44.5	8.5
50	3	46.4	7.0
60	3	48.5	5.9
70	no oscillation	–	–

Table 10

EFFECT OF 5% MISMATCHES IN TUNING CURRENTS ("RIGID")

$2\,I_C$ (μA)	N°periods to lock	Frequency (MHz)	Phase error (°)
0.5	no lock	–	–
1	no lock	–	–
2	9	40.5	26.9
4	6	40.1	10.7
8	4	39.8	5.1
12	3	39.6	3.3
20	3	39.2	2.0
30	3	39.1	1.3
40	3	39.0	1.0
50	3	39.1	0.9
60	3	39.2	0.7
70	3	39.5	0.6
80	3	39.8	0.5
90	3	40.1	0.5
100	3	40.6	0.4

Table 11

EFFECT OF 10% MISMATCHES IN TUNING CURRENTS ("RIGID")

$2\ I_C$ (μA)	N°periods to lock	Frequency (MHz)	Phase error (°)
0.5	no lock	–	–
1	no lock	–	–
2	no lock	–	–
4	7	39.9	28.3
8	4	39.3	10.7
12	3	39.0	6.9
20	3	38.6	4.1
30	3	38.4	2.8
40	3	38.4	2.1
50	3	38.5	1.7
60	3	38.6	1.4
70	3	38.9	1.3
80	3	39.2	1.2
90	3	39.6	1.0
100	3	40.0	1.0
110	3	40.5	0.9
120	3	41.1	0.8
130	3	41.7	0.8
140	3	42.3	0.8
150	3	43.0	0.7

Table 12

EFFECT OF 20% MISMATCHES IN TUNING CURRENTS ("RIGID")

$2\ I_C$ (μA)	N°periods to lock	Frequency (MHz)	Phase error (°)
0.5	no lock	–	–
1	no lock	–	–
2	no lock	–	–
4	no lock	–	–
8	no lock		
12	4	38.2	15.9
20	3	37.6	8.8
30	3	37.4	5.9
40	3	37.3	4.5
50	3	37.4	3.6

Table 11

c.d. Table 12

$2\ I_C$ (μA)	N°periods to lock	Frequency (MHz)	Phase error (°)
60	3	37.6	3.1
70	3	37.9	2.7
80	3	38.3	2.5
90	3	38.7	2.3
100	3	39.2	2.0
110	3	39.7	2.0
120	3	40.3	1.7
130	3	41.0	1.7
140	3	41.7	1.6
150	3	42.4	1.6
160	3	43.2	1.5
170	3	44.1	1.4
180	3	45.0	1.5
190	3	46.1	1.4
200	3	47.1	1.3

As one can see, the "rigid" coupling provides, in general, a lower quadrature error and allows higher coupling currents without stopping the oscillations.

For the different cases of mismatches the amplitudes of voltages at the coupling capacitors are different. This difference is directly related to the difference between the timing capacitances or the difference between the tuning currents.

Table 12

4. DISCUSSION AND CONCLUSIONS

The proposed quadrature oscillator has three degrees of freedom to control the oscillation frequency: timing capacitance, base potential of emitter followers, and tuning current. This can be used to maximize the tuning range, and provides flexibility in adaptation of the tuning range to particular requirements.

Simulations show that coupling of two multivibrators results in a quadrature oscillator which is very robust with respect to mismatches of timing capacitors and of charging currents. The circuit can have more than one decade of frequency tuning (2-100 MHz) for low frequency design, and about one octave (1.5-3.5 GHz) when designed for high frequency operation.

It is possible to make an analogy which will help to understand the difference between "soft" and "rigid" coupling. The transition to "rigid" coupling is similar to introduction of the error amplifier in a phase-locked loop [1]. Introducing this amplifier results in less static error and allows operation at higher frequency as well. This is

similar to phase error reduction and shift to higher tuning frequencies in our case of "locked" multivibrators.

Simulations (not included here) also show that the circuit can be synchronized by an external current source applied between the bases of the emitter followers (points B and B_1, see Fig. 1). This synchronization is very robust, and can be applied to one individual multivibrator or to one of the two multivibrators in the quadrature oscillator. In the last case this results in the quadrature oscillator synchronized by an external source. The investigation of this concept and its applications are the matter of future work.

ACKNOWLEDGMENT

This work was supported by the Portuguese Foundation for Science and Technology (FCT) through funding of INESC-ID, CTS-UNINOVA, and project LEADER (PTDC/EEA-ELC/69791/2006).

REFERENCES

1. P. R. Gray, P. J. Hurst, S. H. Lewis, and R. G. Meyer: *Analysis and Design of Analog Integrated Circuits*, 4th ed., J. Wiley, New York, 2007
2. Buonomo, A. Lo Schiavo: *Analysis of Emitter (Source)-Coupled Multivibrators*, IEEE Trans. Circuits and Systems-I, vol. 53, no. 6, pp. 1193–1202, 2006
3. I. M. Filanovsky, C. J. M. Verhoeven: *Sinusoidal and Relaxation Oscillations in Source--Coupled Multivibrators*, IEEE Trans. Circuits and Systems-II, vol. 54, no. 11, pp. 1009–10013, 2007
4. C. J. M. Verhoeven: *A High-Frequency Electronically Tunable Quadrature Oscillator*, IEEE J. Solid-State Circuits, vol. 27, no. 7, pp. 1097–1100, 1992
5. B. Gilbert: *A Versatile Monolithic Voltage-to-Frequency converter*, IEEE J. Solid-State Circuits, vol. SC-11, no. 6, pp. 852–864, 1976
6. I. M. Filanovsky: *Remarks on Design of Emitter-Coupled Multivibrators*, IEEE Trans. Circuits and Systems, vol. 35 no. 6, pp. 1182–11185, 1992
7. L. B. Oliveira, I. M. Filanovsky, and C. J. M. Verhoeven: *Exact Calculations of Amplitudes and Frequency in an RC Oscillator with Quadrature Outputs*, 47th IEEE Int. Midwest Symp. Circuits and Systems (MWSCAS'04), vol. I, pp. 413–416, July 2004

ELECTRONICS AND TELECOMMUNICATIONS QUARTERLY, 2009, 55, no 4, pp. 617–624

FPGA Implementation of a Numerically Controlled Oscillator with Spur Reduction

STEFAN LACHOWICZ*, HANS-JÖRG PFLEIDERER**

*Edith Cowan University, Perth, Western Australia
e-mail: s.lachowicz@ecu.edu.au
**Ulm University, Germany
e-mail: hans-joerg.pfleiderer@uni-ulm.de

Received 2009.09.21
Authorized 2009.11.09

This paper presents a novel method of reducing the spurious signal content in a digitally synthesized sine wave at the output of a numerically controlled oscillator (NCO). The proposed method uses a linear approximation subsystem with a reduced size look-up table (LUT). Two NCO architectures are considered. Architecture 0 - which is the standard - in which the accumulator word length is longer than the LUT address word, is compared with Architecture 1, where the accumulator bits beyond the LUT address space are used for the linear approximation of the value in between the entries of the LUT. Analysis of both architectures demonstrates that the spurious free dynamic range (SFDR) in Architecture 1 equates to 12 dBc per bit of the address space of the LUT as opposed to 6 dBc for Architecture 0. The system was implemented and tested using the Xilinx Spartan 3 platform.

Keywords: Numerically controlled oscillator; Digital waveform synthesis; Spurious free dynamic range, FPGA

1. INTRODUCTION

Field Programmable Gate Arrays (FPGA) are becoming more widely used in Digital Signal Processing (DSP) systems. Modern FPGAs exhibit very high performance, very large number of IOs and high capacity memory on the chip. The development is rapid and risks are low since the IP can be easily modified. For the low to medium production volume range, it is not economical to develop an ASIC and, if needed, there are companies who offer convenient solutions to allow for the seamless migration from FPGA to ASIC.

The evolution of FPGAs has enabled to implement more and more sophisticated DSP subsystems in the form of dedicated hardware on the device. In late 1990s, FPGAs usually had just a few hardware multipliers per chip. In the early 2000s, hardwired multipliers in large numbers (up to ~500), with clock speeds of up to 100 MHz became available. Mid 2000s saw DSP algorithms like full FIR filters implemented, and currently, powerful arithmetic, such as fast square root and divide, floating point operations and many more are being implemented.

In a DSP systems, nonlinear functions, such as trigonometric, square root or Bessel functions are often encountered. There are several solutions to this problem, for instance, using a CORDIC core, or look-up tables (LUTs). A great deal of effort is expended to optimize LUTs to maintain the precision required, whilst minimizing the actual size of the table.

For some functions, an existing approach is to utilize hierarchical LUTs. In this work, we present a numerically controlled oscillator (NCO) - sometimes referred to as a direct digital frequency synthesizer (DDFS) - using a LUT and a linear approximation circuit for the generation of the sine wave values in between the entries of the LUT.

Today's advanced DDFS solutions are fast becoming an alternative to traditional analog synthesizers. The main advantages of a DDFS system are [1]:

- Micro-Hertz tuning resolution of the output frequency and sub-degree phase tuning capability.
- Extremely fast "hopping speed" with continuous phase.
- No manual system tuning as in analog systems.
- Unparalleled matching and control of I and Q signals in a quadrature synthesizer.

The conventional digital sinusoid generation in a NCO, referred to as Architecture 0, is presented in Fig. 1.

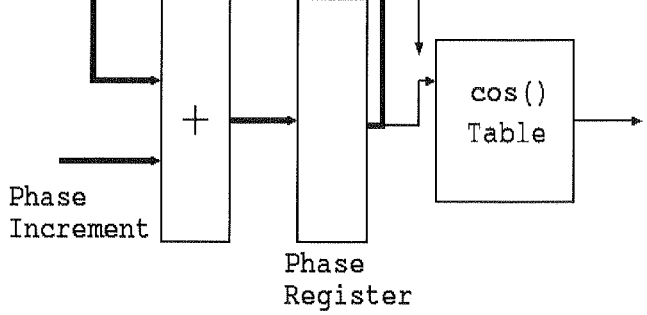

Fig. 1. Conventional digital sinusoid generation (Architecture 0)

In this system the phase register width N is normally between 24 and 48 bits. The truncation is determined by the LUT size, and leaves n between 10 and 16 bits which

corresponds to one quarter of 1024 to 65536 memory locations in the LUT. The table stores uniformly spaced samples of a cosine wave. The sinusoid argument is:

$$\Theta(k) = k\frac{2\pi}{2^n} \tag{1}$$

The output frequency f_{out} and the frequency resolution Δf can be expressed:

$$f_{out} = \frac{f_{clk}\Delta\theta}{2^N} \tag{2}$$

$$\Delta f = \frac{f_{clk}}{2^N} \tag{3}$$

where $\Delta\theta$ is the phase increment value.

In the system from Fig. 1, there are several sources of spurious frequencies. Firstly, the precision of the samples stored in the LUT creates a noise floor corresponding to the number of bits used for storing the samples. If the NCO is followed by the digital-to-analog converter (DAC), the precision of the converter further limits the signal-to-noise ratio (SNR). The influence of the DAC will not be considered further in this paper. In the digital domain, this quantization noise can be at least partially suppressed by dithering [2]. The second and the most dominant source of spurious frequencies, severely limiting the spurious free dynamic range (SFDR) is the truncation of the phase word related to the size limit of the LUT. Because both the phase and amplitude samples are periodic sequences, their finite word length representations contain periodic error sequences, which cause spurs. The spur signal level in Architecture 0 is approximately 6 dB per address bit of the look-up table below the amplitude of the desired sinusoidal signal [3].

The remainder of the paper is organized as follows. Section 2 presents the method of linear approximation as applied in the NCO, referred to as Architecture 1. Section 3 deals with the analysis of the performance of Architecture 1. Section 4 presents the results of the simulations and hardware implementation, and the obtained output spectra of the NCO. It is followed by conclusions.

2. NUMERICALLY CONTROLLED OSCILLATOR ARCHITECTURE WITH LINEAR APPROXIMATION

2.1. LINEAR APPROXIMATION WITH LOOK-UP TABLES

One method of enhancing the LUT method of generating a nonlinear function such as a cosine, is to use a linear approximation circuit. Every function can be approximated by a piecewise linear function as presented in Fig. 2 (a). Within a segment (or between the node points) the function can be expressed using the line equation:

$$\hat{f}(x) = y_i + \frac{y_{i+1} - y_i}{x_{i+1} - x_i}(x - x_i) \tag{4}$$

There are two ways to select the values of the function at the node points (segment boundaries). The first is simply to choose the exact values (within a given precision), as represented by the node points of the linear segment $\hat{f}(x)$ in Fig. 3 (a). In this case, the error $f(x) - \hat{f}(x)$ is nonnegative for the range of x where the function is convex, and nonpositive for the range of x where the function is concave. The second way is to adjust the boundary points in such a way that they are shifted from the exact values by half of the average of the maximum errors in the segments to the left and to the right of the segment boundary. In this case, the maximum error magnitude $f(x) - \hat{f}_1(x)$ in the segment is halved and its sign changes within a segment. However, in the special case of the harmonic function, this adjustment in the time domain will only affect the magnitude of the respective frequency components, which can be instead corrected by adjusting the gain slightly. Therefore, in our system, the former method of selection is used.

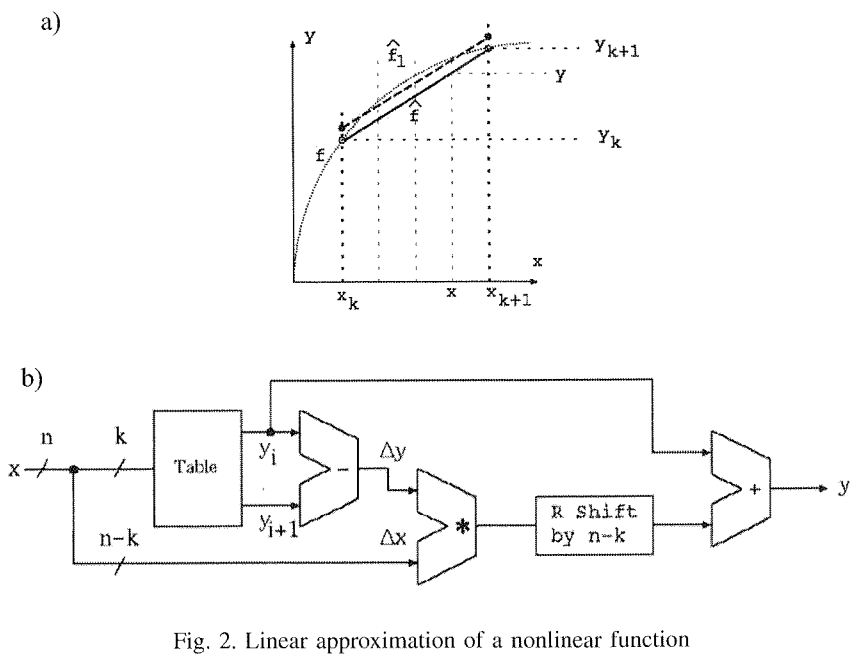

Fig. 2. Linear approximation of a nonlinear function

The hardware mapping is presented in Fig. 2 (b). Here, the segments of the LUT are evenly distributed, so the input word x is split into two parts: the more significant part is an address for the LUT and the less significant part is an increment of x within the current segment of the LUT. The node values y_i and y_{i+1} are read from the LUT, the increment $y_{i+1} - y_i$ is calculated and is subsequently multiplied by the increment

Δx. The shift replaces the division in (4), as the difference $x_{i+1} - x_i$ is constant and a power of two.

2.2. IMPROVED NCO ARCHITECTURE (ARCHITECTURE 1)

Fig. 3 presents the proposed Architecture 1 of a NCO with an embedded linear approximation circuit. All accumulator bits are fed into the phase-to-amplitude converter. The top portion of the accumulator bits is used to address the cosine LUT and the remaining bits are used for linear approximation. The LUT contains the cosine samples in the first quadrant, and some simple logic is used for address sequence reversal in quadrants 2 and 4, and sign change in quadrants 2 and 3 to obtain the full period of the waveform.

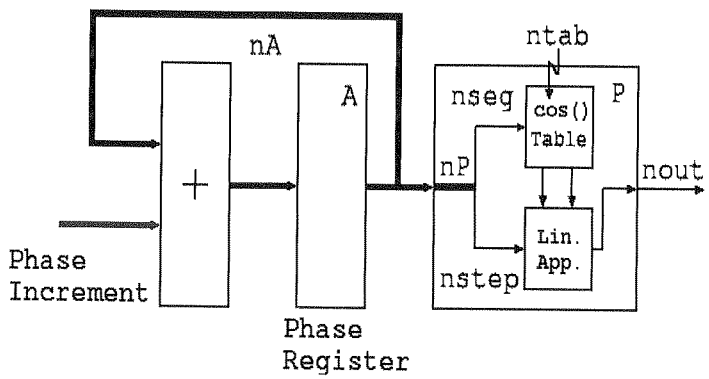

Fig. 3. NCO Architecture 1

3. NCO ARCHITECTURE 1 PERFORMANCE

In [3], the following analysis yields an upper bound on the size of the largest frequency component in the spectrum $e_A[n]$, of the error sequence of a mid-tread quantizer, applicable to Architecture 0. Assuming that the quantizer is not saturated by the input signal $x[n]$, the maximum possible quantization error is $\Delta_A/2$ where Δ_A is the amplitude quantization step size. The total power in $e_A[n]$ is then bounded by $\Delta_A^2/4$. By Parseval's relation, the sum of the spur powers in the spectrum of $e_A[n]$ equals the power in $e_A[n]$. In order to maximize the power in a given spur, the total number of spurs must be minimized. Since $e_A[n]$ is real, the maximum power in a spur occurs when there are two frequency components at $+\omega_{spur}$ and $-\omega_{spur}$, with equal power (excluding DC offsets and half sampling rate spurs which can be easily eliminated). With two frequency components the power in a single spur is $\leq \Delta_A^2/8$.

Since $x[n]$ is real, its spectrum consists of a positive and a negative frequency component, each having a power of $A^2/4$. Using the above bound on spur power, the

SFDR is $\leq \Delta_A^2/(2A^2)$. If $A \approx 1/2$ provided b is not small, then in dBc (decibels in respect to carrier), SFDR $\leq 3 - 6b$ dBc, where $\Delta_A = 2^{-b}$, and b is the LUT address length in bits. In summary, this upper bound on power in a spur caused by amplitude quantization exhibits -6 dBc per bit behavior.

In [4], it is shown that for linear approximation, the worst case approximation error is bounded by

$$\epsilon_{\max} = \frac{h^2}{8} \max\left(\left|f''(x)\right|\right) \tag{5}$$

where $h = x_{k+1} - x_k$ and $x = [x_k, x_{k+1}]$, as in Fig. 3(a). For a cosine:

$$\max\left(\left|f''(x)\right|\right) = 1 \tag{6}$$

Thus, $\epsilon_{\max} \sim h^2$. Consequently, doubling the LUT size, and therefore halving h, reduces the maximum error by a factor of 4, ie. 2 bits. Therefore, if the quantization step corresponds to the maximum error, the result is -12 dBc per bit behavior. Fig. 5 presents the output spectrum of the NCO, with a 12-bit address-space LUT and precision of 20 bits. As expected, the SFDR is approximately $12 \times 12 = 144$ dB.

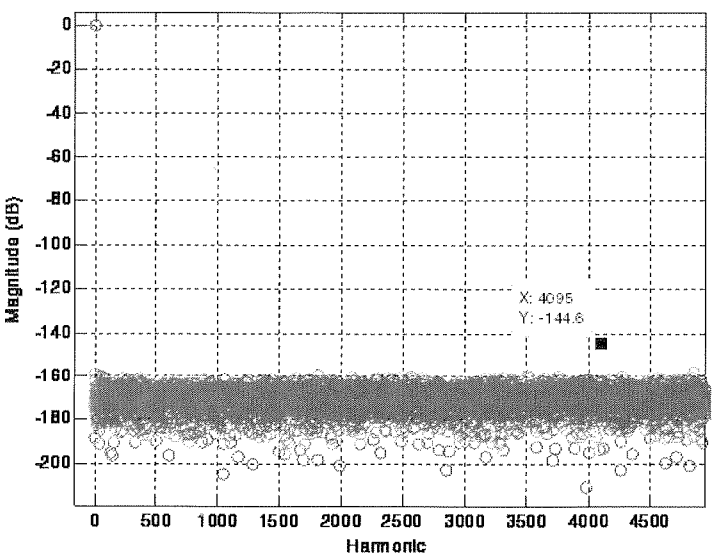

Fig. 4. Output spectrum of a NCO with 12-bit address space and 20-bit precision

Fig. 6 presents the comparison of the performance between Architecture 0 and Architecture 1.

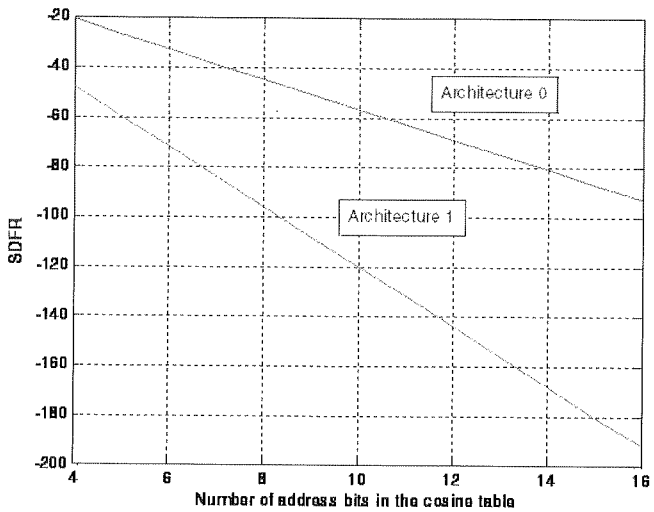

Fig. 5. Performance comparison between the two NCO architectures

4. FPGA IMPLEMENTATION

The reduced-spur NCO has been designed, synthesized for the Spartan 3 platform, and simulated and tested using Xilinx ISE tools and ModelSim. The LUT was constrained by the available size of the block RAM in a Spartan 3 chip. The size of the block RAM is 512 × 32 bits. Only one quadrant needs to be stored in RAM. Additionally, one memory location was split into a 20-bit value and a 12-bit increment of the successive sample. Therefore, effectively the LUT stored 1024 values for one quadrant of the cosine, yielding a 12-bit addressing space for the full period of the waveform. The design required the following resources in an xc3s1000 chip:

- 325 slices (1.3 %)
- One block RAM (4 %)
- 2 hardware multipliers (8%) forming one combined multiplier for word lengths greater than 16.

The master clock frequency was 50 MHz and the latency of the NCO was 1 clock cycle, which would allow very fast frequency hopping and compares favorably with the DDFS system presented in [5] which requires 11 clock cycles, while using a smaller LUT.

5. CONCLUSIONS

A novel architecture of a numerically controlled oscillator has been developed. A distinguishing feature of the proposed solution is the application of linear approxi-

mation, leading to significant improvements of the spurious performance of the NCO. It is shown that if all the bits of the phase accumulator of the NCO are used for phase-to-amplitude conversion using the linear approximation, as is the case of Architecture 1, the SFDR increases at a rate of 12 dBc per per bit of the LUT addressing space, as opposed to 6 dBc in the standard architecture (Architecture 0). The achieved SDFR of 144 dB compares also favourably to the Xilinx core [7], which is capable of a maximum SFDR of 120 dB. Future work will include the application of variable step LUTs [6], and 2^{nd} order polynomial interpolation.

REFERENCES

1. Analog Devices: *A technical tutorial on digital signal synthesis*, http://www.analog.com/static/imported-files/tutorials/ 450968421DDS_Tutorial_rev12-2-99.pdf, 1999
2. L. Schuchman: *Dither signals and their effects on quantization noise*, IEEE Trans. Commun. Technol., Vol. COM-12, pp. 162–165, Dec. 1964
3. M. J. Flanagan and G. A. Zimmerman: *Spur-reduced digital sinusoid synthesis*, IEEE Trans. Communications, Vol. 43, No. 7, pp. 2254–2262, July 1995
4. D-U. Lee, R. C. C. Cheung, W. Luk and J. D. Villasenor: *Hardware implementation trade-offs of polynomial approximations and interpolations*, IEEE Trans. Computers, Vol. 57, No. 5, pp. 686–701, May 2008
5. Y. Song and B. Kim: *Quadrature direct digital frequency synthesizers using interpolation-based angle rotation*, IEEE Trans. VLSI Syst., Vol. 12, No. 7, pp. 701–710, July 2004
6. S. Lachowicz and H-J. Pfleiderer: *Fast evaluation of nonlinear functions using FPGAs*, Proc. 4th Intl. Symposium on Electronic Design, Test and Applications DELTA 2008, Hong Kong, Jan 2008
7. Xilinx (Logic Core): *DDS Compiler v2.1*, DS558, March 24, 2008

ELECTRONICS AND TELECOMMUNICATIONS QUARTERLY, 2009, 55, no 4, pp. 625–637

Silicon 9 MHz MEMS Based Oscillator with Low Phase Noise and High Quality Factor

FABRIZIO LO CONTE*, DANIEL GROGG**, ADRIAN MIHAI IONESCU**, MAHER KAYAL*

* *Electronic Laboratory (e-lab.epfl.ch)*
** *Nanoelectronic Devices Laboratory (nanolab.epfl.ch)*
*,** *EPFL, 1015 Lausanne, Switzerland*
e-mail: fabrizio.loconte@epfl.ch; daniel.grogg@epfl.ch; adrian.ionescu@epfl.ch; maher.kayal@epfl.ch

Received 2009.09.21
Authorized 2009.11.11

A 9.4MHz micro-electromechanical oscillator based on a Vibrating Body Field Effect Transistor (VB-FET) is presented in this work. The electrical characteristics of this active MEM resonator are detailed for static and dynamic operation. In open-loop configuration the tuning fork resonator provide a quality factor of 9400. The benefit of the intrinsic gain for oscillator design is analyzed and an oscillator design is proposed based on these findings. The proposed oscillator is fully CMOS compatible. The achieved performance shows the advantages of an active MEM resonator for the construction of MEM based oscillators.

Keywords: Active MEMS, resonator, tunable oscillator, tuning fork, phase noise

1. INTRODUCTION

For timing and frequency reference applications micromechanical resonators attract a lot of interest, due to their promise of miniaturization and integration with CMOS technology compared to quartz resonators. Even though micromechanical resonators have shown performances on a par with quartz resonators or even better [1], miniaturization of these devices faces some practical problems. One major issue is the increasing motional resistance of capacitive MEM resonators with decreasing size. The concepts of Resonant Gate [2, 3] and Vibrating Body [4] FET take advantage of a built-in amplification to increase the output signal, thus reducing the motional resistance.

This is especially interesting to build oscillators, as the requirements on the sustaining amplifier are reduced. Oscillators based on capacitive MEM resonator have

been reported [5, 6] and it was found that an automatic level control [7, 8] reduces an unwanted $1/f^3$ phase noise component. An oscillator based on this type of devices was presented in [9] and [10]. In this paper the impact of the built-in amplification on the feedback loop will be discussed in detail based on experimental results.

2. THE VB-FET

Figure 1a is a SEM image of a fabricated tuning fork design based on the VB-FET technology [11]. The device is designed to vibrate laterally (in-plane), the mode shape, simulated with ANSYS is shown on the right side (Fig. 1b). The FET is placed at the center of each suspended beam, where the displacement is the largest. The body region of the FET is indicated with square. The drain current is modulated in the body region, as a function of the applied gate voltages and the variation of the gate capacitances. The body region is mobile and the gate is fixed (Fig. 1c), the modulation of the charges occurs on the lateral surface facing the gate electrode. In this configuration the channel width is limited to the thickness of the substrate; the channel length can be designed

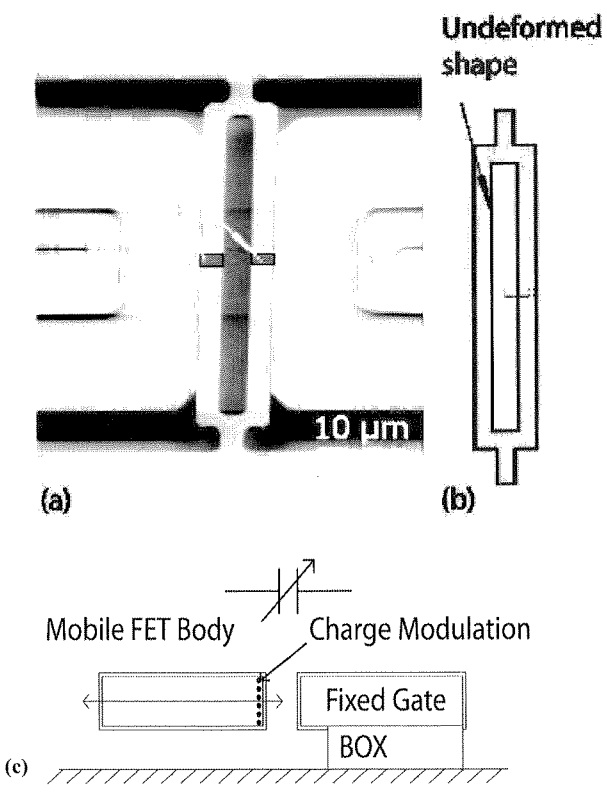

Fig. 1. a) SEM image of a tuning fork Vibrating Body FET and b) its fundamental in-plane mode shape. c) Cross section of VB-FET; the channel is formed on the lateral side, facing the gate electrode

by CAD. The gate-to-channel capacitance is formed by the air gap in series with two thin oxide layers and mainly given by the gap. Additionally to the FET current modulation, the varying capacitance between the gate and the resonator induces a capacitive current (like in purely capacitive MEM resonators). Furthermore, the total current may be influenced by the modulation of the resistance of the silicon body and the piezoresistivity of silicon.

The investigated VB-FETs are designed and fabricated on a SOI substrate with a 1.25μm thin silicon film on a 3μm BOX based on a process that uses sacrificial polysilicon and DRIE to define sub-200 nm air gaps [5]. The beams of the tuning fork are 40μm long and 3μm wide. The source, drain and gate are phosphorous doped with an impurity concentration on the order of $4 \cdot 10^{19}$ cm^{-3}. The phosphorous doping of the channel region is estimated from measurements to be on the order of $6 \cdot 10^{15}$ cm^{-3}. The channel is 1μm long and 1.25μm wide. A thermal oxide is grown on the released resonator surface to reduce the number of surface charges. The gaps between the resonator and the gate electrode are dry etched into the silicon. A gap dimension of 180nm has been measured by microscopy.

3. ELECTRICAL DEVICE CHARACTERISTICS

The static characteristics, I_D-V_D and I_D-V_G are shown in Fig. 2. For these measurements V_G was applied on both gates. The VB-FET behaves like a depletion-mode MOSFET with a deep implant, which cannot be completely turned off by applying high negative voltage. As a consequence the I_D-V_D characteristic is strongly dominated by the current through the VB-FET body and has only a limited influence on the gate voltage. This is also observed on the I_D-V_G curve. The modulation of I_D is almost linear with V_G, but the current through the body remains high. The extracted transconductance values 2.2μS at V_G=15V correspond well to the low gate-to-channel capacitance. The drain current is on the order of 1.1mA when V_G is equal to zero and modulated by 2μA per volt. This rather high current is due to the size of the n-type body in this depletion mode configuration. The apparent drain resistance shown in Fig. 2b increases with the drain voltage. Thus it is convenient to work with a high V_D in order to have the maximum intrinsic gain of the resonator and a high source-to-drain resistance. However the drain voltage is limited by saturation and self-heating. At higher V_D the intrinsic gain saturates and thermal effects dominate the mechanical properties of the device.

Figure 3 reports the frequency spectrum of a tuning fork VB-FET with a 15V gate voltage. All measurements are done in a vacuum (better 10^{-5}mbar) with a vector network analyzer HP8753D. The quality factor has been extracted using the 3dB method from the transmission scattering parameter S_{21}. The resonator motion is excited by applying an ac and a dc voltage on gate 1 using a bias-T. The time harmonic electrostatic force acts only on one side of the resonator, gate 2 is used solely to modulate the current in the second channel.

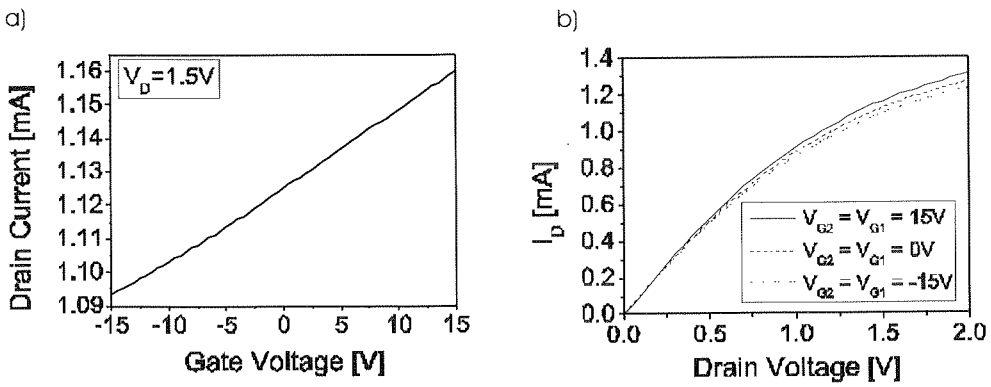

Fig. 2. a) Experimantal I_d-V_g characteristics b) Experimantal I_d-V_d characteristics of a tuning fork VB-FET (beam length=40μm, beam width=3μm, channel length=1μm). The gate voltage is applied on both gates (V_{G1}=V_{G2})

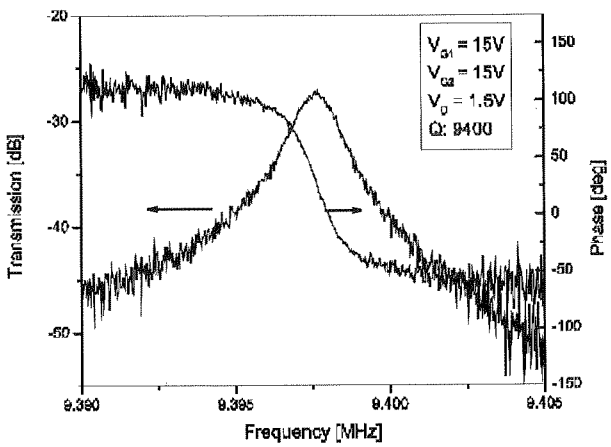

Fig. 3. Magnitude and phase of the scattering transmission parameter for a VB-FET

Under the given biasing conditions the quality factor of the device is 9400. The maximum transmission obtained is -27.5dB and a phase shift of 180° is observed around the resonance frequency. As the device is operated in a vacuum chamber rather long cables had to be used, which introduce an additional, constant phase shift.

The tuning fork VB-FET transmission characteristics are dependent on the combination of the two gate voltages and the drain voltage. Qualitatively, the transconductance of a FET is proportional to the drain current and this is also the case for the VB-FET, resulting in a strong increase of the maximum Sparameter with the drain current (Fig. 4). As a second effect, a reduction of the resonance frequency is observed when V_D increases.

Frequency tuning based on the variation of V_G can be obtained either by varying both gate voltages simultaneously (Fig. 5) or by varying only one (Fig. 6). Changing

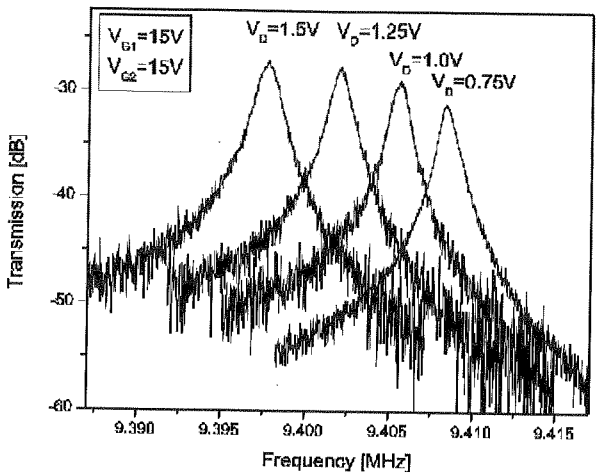

Fig. 4. Frequency spectra of the VB-FET with V_D as parameter

only V_{G2} results in a narrow tuning range, leaving the amplitude of vibration unchanged. The spring softening in the gap between gate 1 and the resonator is dominant and the effect on the frequency through gate 2 is small. The internal gain of the device depends on the gate voltage, but the dependence is not very strong. Therefore the transmission characteristics remain almost unchanged in magnitude. Frequency tuning based on variation of V_{G2} results in a tuning range of ~2kHz per volt. Varying the bias voltage on both gates results in a higher tuning range (~20kHz per volt). The current modulation is dependent on the amplitude of vibration and therefore a function of V_G. As a consequence, the varying gate voltage reduces the spring softening and the internal gain of the device.

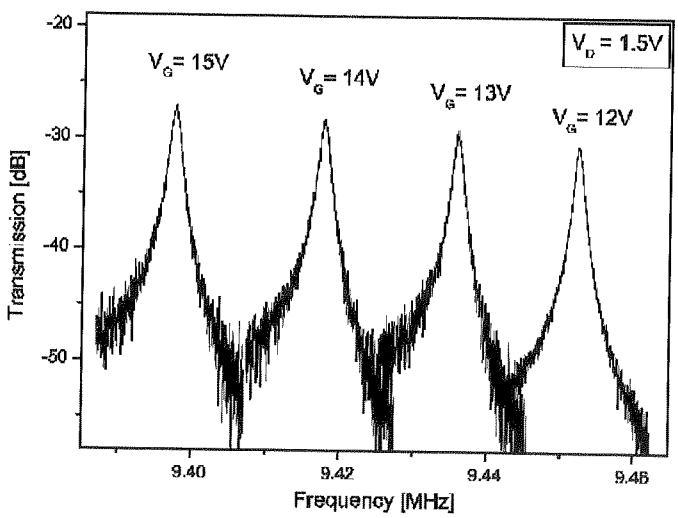

Fig. 5. Frequency spectra of the VB-FET with as parameter V_G=V_{G1}=V_{G2}

$$f_{res} = \frac{1}{2\pi}\sqrt{\frac{k_{mech} - k_{el}}{m_{eff}}} \approx f_0 - \frac{k_{el}}{2\pi m_{eff}} \tag{1}$$

Where k_{mech} and k_{el} are the mechanical and electrical spring constant respectively. The term m_{eff} stands for the effective resonator mass of the beam.

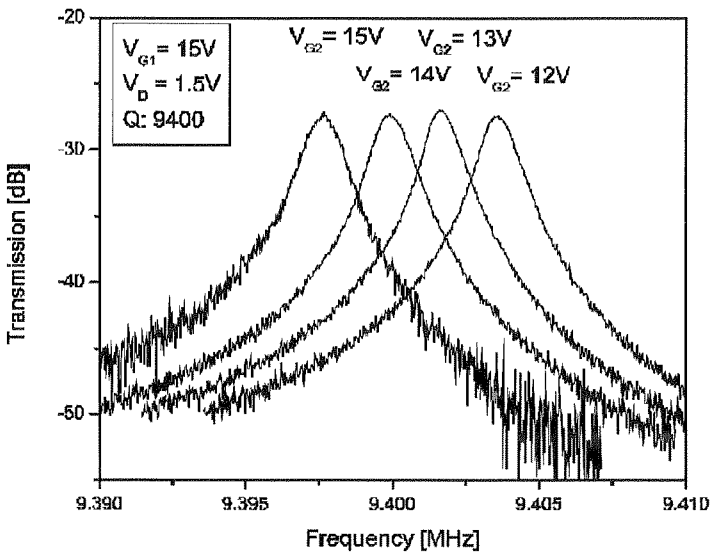

Fig. 6. Frequency spectra of the VB-FET with as parameter V_{G2} and with V_{G1}=constant

4. SUSTAINING ELECTORNICS

4.1. EQUIVALENT MODELLING

The VB-FET can be seen as a lumped G_m, RLC network when a first order small signal analysis is done. The G_m and R_1 parameters can be extracted from the measurements shown in Fig. 2, the other parameters are fitted based on the magnitude and phase transmission characteristics.

The resonant frequency is given by the LC product, as:

$$\omega_0 = \frac{1}{\sqrt{LC}} \tag{2}$$

The quality factor can be expressed in a mechanical or an electrical way:

$$Q = \frac{\sqrt{m \cdot k}}{Df} \tag{3}$$

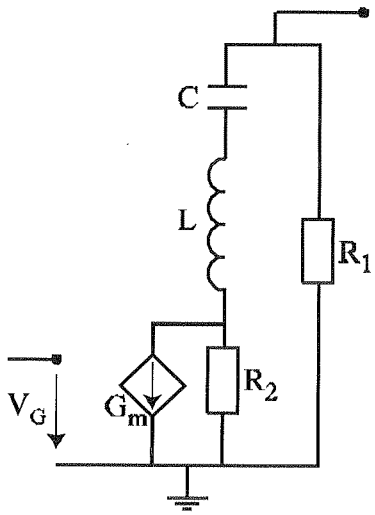

Fig. 7. Electrical Equivalent Small Signal Model

Where m is the equivalent mass of the moving beam, k the equivalent elasticity and Df the damping factor. The term m is normalized by the mode shape to obtain the effective (lumped model) mass. To extract the quality factor of the equivalent schematic the following transfer function should be calculated:

$$V_{out} = \frac{g_m \cdot V_G \cdot R_1 \cdot R_2}{Z_t + R_2} \tag{4}$$

Where Z_t is the impedance of the resonant CLR_1 branch that can be written as:

$$Z_t = \frac{L}{j\omega}\left((j\omega)^2 + j\omega\frac{R_1}{L} + \frac{1}{L \cdot C}\right) \tag{5}$$

Q can be written as:

$$Q = \frac{\omega_0}{2 \cdot \Delta\omega} = \frac{1}{R_1 + R_2}\sqrt{\frac{L}{C}} \tag{6}$$

$\Delta\omega$ is the frequency shift where an attenuation of 3dB appears in the transfer function.

This device is thus similar to a series RLC resonator apart from its particularity, the high biasing voltages. A classical way of doing oscillator is to connect the resonator in the feedback loop of a high gain amplifier.

One particular problem of MEM resonators are the non-linearity phenomena. For the described VB-FET device under the given biasing conditions, the electrical non-linearity is limiting the linear behavior. Such a device can be considered linear only for small displacement, thus for small current modulation. Or, larger amplitudes

are preferred to increase the current modulation and lessen the specifications of the electronic front-end.

The second difficulty present with active MEMS is the high biasing voltage needed for a working dispositive. Thus, a high voltage amplifier is needed to use the resonator in a feedback loop. The sustainment signal applied to the gate should be on the order of some milli-volts so as to avoid electrical non-linearity. Designing such a high voltage amplifier able to deal with milli-volts is a difficult task.

In this article we propose a topology where the resonator is referenced to ground and can be driven with a low-voltage amplifier without a complex gain loop control. Instead an active band pass filter is used. The measured transfer function is shown in Fig. 8. A proof of concept oscillator based on discrete elements has been realized, a fully integrated SOI solution is planned where the tuning of circuit-level parameters [12, 13] or system level parameters [14] will be done.

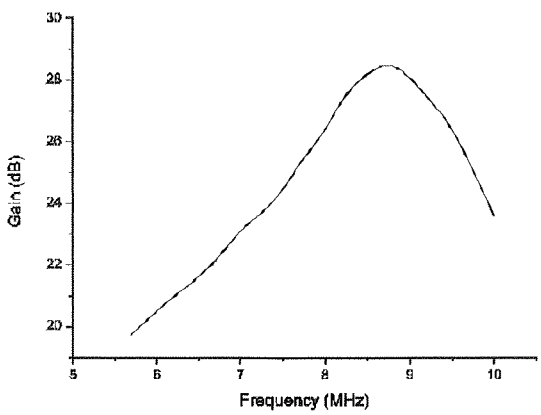

Fig. 8. Transfer function of the amplifier around the resonating frequency

The resonant frequency of the VB-FET (around 9.4 MHz) is above the flat part of the amplifier transfer function. As a consequence, a shift in the resonance frequency will automatically affect the gain of the overall loop. Thus playing on the gate and on the drain voltage of the VB-FET will set both the loop gain and the phase.

This architecture, using continuous time filter, offers the advantage to be easy to integrate in an IC. Moreover, the high voltages are confined on the MEM device, thus low cost classical 0.35μm technology can be used for the ASIC.

4.2. ADVANTAGES OF ACTIVE MEMS IN μ-ELECTRONICS

An important issue in resonators based on MEM dispositive is the electrical non-linearity appearing when the input voltage is too high. The amplitude of a resonant MEM device is limited [15] and proportional to the product of the input voltages (V_{dc}· V_{ac}). The non linearity effect of the used VB-FET with a gate voltage of 15V appears at an ac signal of approximately 5mV. The increase of applied input power

leads to a strong reduction in the transmission peak and a bending of the resonance frequency toward lower frequencies. This bending corresponds to the theory of the damped-forced Duffing system [16].

In non-active resonators, due to the fact that the output signal is in one to two orders of magnitude lower [4] extracting the output signal requires a very low-noise input stage in the electronic part.

One of the advantages of the current VB-FET is to have an intrinsic gain, which allows to simplify drastically the electronics. This resonator can be seen as a tunable band-pass filter with a very high quality factor and small insertion loss.

As shown in the previous section, the gain of the system and the resonant frequency can be tuned by biasing. The drawback is that these two characteristics are not independent. In fact, the gain loop increases when V_D is increased, but at the same time the resonant frequency decreases. The same phenomena appear for the gate voltage. But the gain and the resonant frequency can be set independently using a combination of both tuning parameters.

Thus, from an electronic point of view, this type of devices offers numerous advantages when tunable high quality factor filtering is required, typically in oscillator circuits. Its sensitivity to the biasing conditions can be controlled, since those biasing conditions are set very precisely in micro-electronics.

4.3. OPEN-LOOP CHARACTERIZATION

The band-pass amplifier shown on Fig. 9, was connected to the VB-FET in order to increase the transmission characteristic. Both poles have their respective frequencies lower than the device resonating frequency, as stated in the previous section.

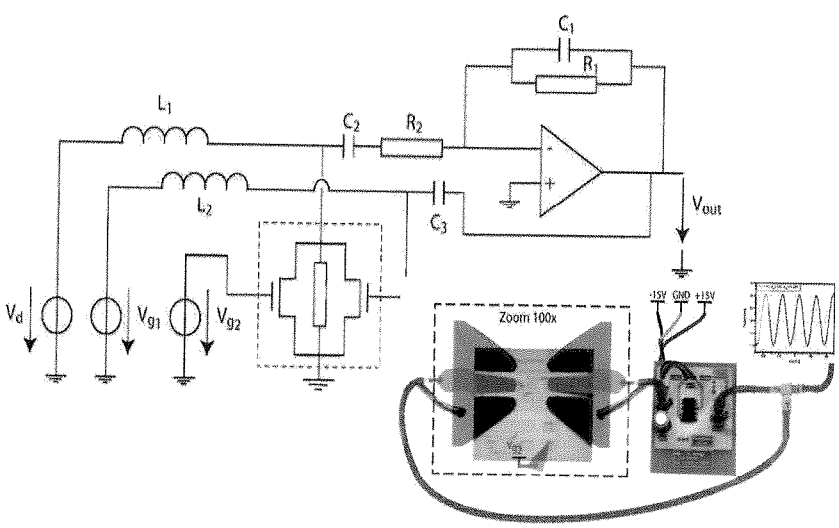

Fig. 9. Oscillator Schematic in closed loop configuration

The DC operation voltages are applied to the circuit using a commercial bias-T. The circuit elements L_1 and L_2 are thus given.

The drain current is the output of the device and is modulated by the mechanical oscillation. The current-to-voltage conversion is done directly on the VB-FET, taking advantage of the high drain impedance shown in Fig. 2. In fact the input impedance of the amplifier has been kept higher than the output impedance of the dispositive. The small signal resistance seen from the drain of the VB-FET increases with V_D, it is around 2.5kΩ at 1.5V.

The simulation and the measurement of the open loop characteristic of the circuit are shown in Fig. 10 and 11 respectively. The capacitor C3 of the final oscillator schematic (Fig. 9) has been removed in order to work in an open-loop configuration.

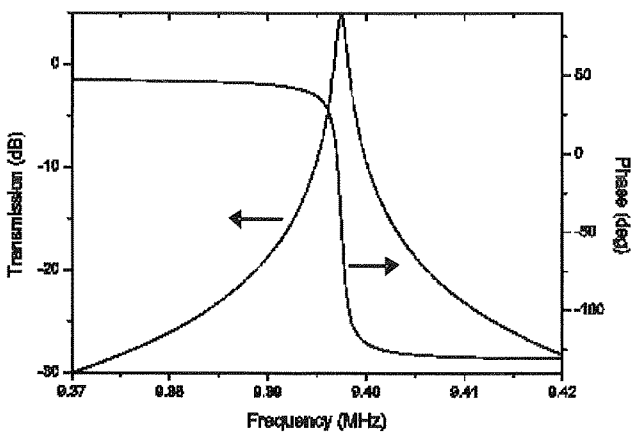

Fig. 10. Simulated open loop magnitude and phase characteristics

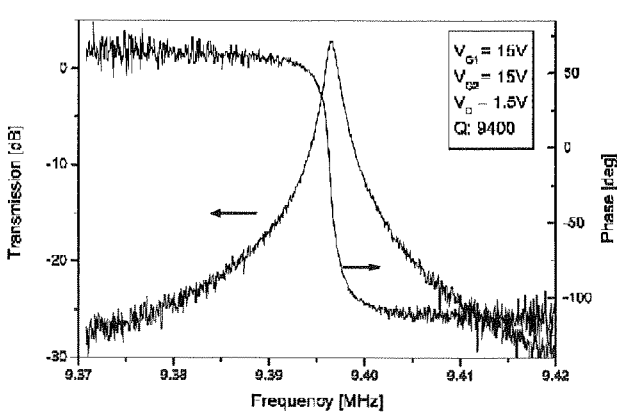

Fig. 11. Measured open loop magnitude and phase of the VB-FET oscillator

As expected a gain of 2.9dB is observed for the given biasing conditions. The measured phase of the overall loop at the resonant frequency is approximately -30°. The zero phase shift needed to sustain the amplifier is obtained around 9.395 MHz, thus at a lower frequency that the one presented.

4.4. OSCILLATOR PERFORMANCE

The setup shown in Fig. 9, using microprobes to connect the VB-FET resonator has been used. In the closed-loop process the output of the amplifier is measured using an appropriate buffer to avoid loading the amplifier with the 50 Ohm input impedance of the spectral analyzer.

Figure 12 shows the spectrum of the oscillator and the sinusoidal output signal measured after the sustaining amplifier. A drain voltage of 1.5V and gate voltages of 14V and 13.7V are applied respectively on gate 1 and gate 2. The reduced gate voltages were used to reduce parasitic effects and obtain the best possible oscillator spectrum. This tuning influences slightly on the gain in the oscillator loop and the frequency of operation. The amplitude of approximately 20mV corresponds well to the limit of linear operating region measured on this device. From the difference between the measured onset of non-linearity and the actual amplitude we conclude that the electrical non-linearity of the resonator is limiting the maximum amplitude. A small amplitude modulation of the sinusoidal signal is observed, which we link to the non-linear operation of the resonator. The amplitude frequency relation is no longer a single valued function in the non-linear region and it may be that there is no stable point of operation. As a consequence an oscillation of the amplitude around the point of unity loop gain is observed. When a higher gain is set in the system, parasitical peaks related to the amplitude modulation appear in the spectrum. It is not yet known if this modulation contributes to the observed phase noise.

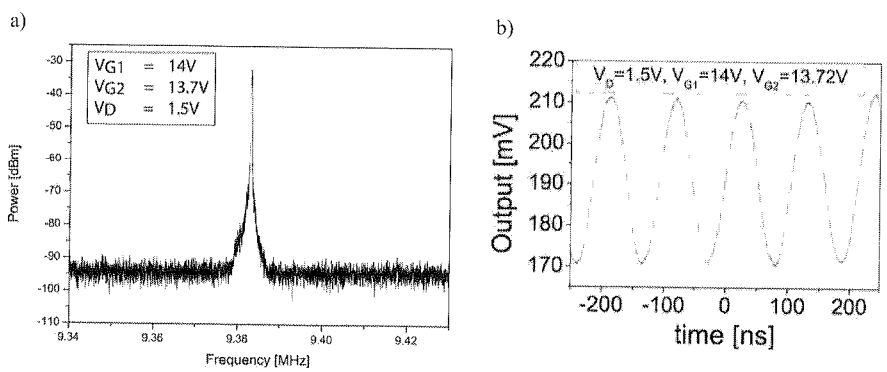

Fig. 12. a) Spectrum of the VB-FET based oscillator b) Sinusoidal output signal of 20 mV

The phase noise was extracted from the frequency spectrum of Fig. 12 with V_G set to 13.7V. As expected, the phase noise follows a $1/f^3$ characteristics curves, suspected

to be caused by the electrical non-linearity. An explanation for the observed phase noise is given in [17] and is directly applicable to VB-FETs, as the excitation of the resonator is also based on electrostatic force. The noise floor measured for the amplifier is in the range of -74dBc (not shown). These values for phase noise and frequency stability are quite far away from the performance obtained with quartz crystal based oscillator. This is a direct consequence of the capacitive excitation used and its inherent non-linearity. However the advantage of the built-in amplification to drive the miniaturization further and reduce the requirements of the sustaining amplifier remains.

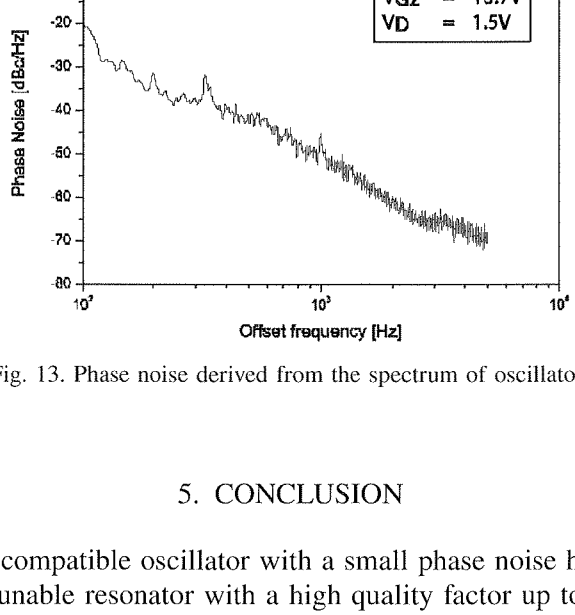

Fig. 13. Phase noise derived from the spectrum of oscillator

5. CONCLUSION

A full CMOS compatible oscillator with a small phase noise has been built using an active MEMS tunable resonator with a high quality factor up to 9400.

This type of oscillators is a growing field of research. Fully on-chip high precise oscillators can nowadays be obtained only at very high frequencies using LC resonator but most of time the noise figure is still not good enough to use them in RF communication.

The resonator used in this case offers a quality factor almost as high as a quartz resonator. In respect to other resonating MEMS the output level is higher due to its intrinsic gain. Therefore, we have been able to interface it with discrete electronics as a proof of concept. The realized oscillator has a tunable frequency. The other advantage of the current structure is that a classical low voltage amplifier can be used due to the fact that the high biasing voltages are decoupled.

Further steps can be taken with the enhancement of the intrinsic gain of the VB-FET and the generation of the biasing voltage in such a way that the frequency and the gain settings will be decoupled.

REFERENCES

1. C. T. C. Nguyen: *MEMS technology for timing and frequency control*, Ultrasonics, Ferroelectrics and Frequency Control, IEEE Transactions on, vol. 54, pp. 251–270, 2007
2. J. H. C. Nathanson and R. A. Wickstrom: *A Resonant-Gate Silicon Surface Transistor With High-Q Band-Pass Properties*, Applied Physics Letters, vol. 7, pp. 84–86, 1965
3. N. Abele, R. Fritschi, K. Boucart, F. Casset, P. Ancey, and A. M. Ionescu: *Suspended-gate MOSFET: bringing new MEMS functionality into solid-state MOS transistor*, in Electron Devices Meeting, 2005. IEDM Technical Digest. IEEE International, pp. 479–481, 2005
4. D. Grogg, M. Mazza, D. Tsamados, and A. M. Ionescu: *Multi-Gate Vibrating-Body Field Effect Transistors (VB-FETs)*, in Electron Devices Meeting, 2008. IEDM 2008. IEEE International, pp. 663–666, 2008
5. C. T. C. Nguyen and R. T. Howe: *Design and performance of CMOS micromechanical resonator oscillators*, in Frequency Control Symposium, 1994. 48th., Proceedings of the 1994 IEEE International, pp. 127–134, 1994
6. C. T. C. Nguyen and R. T. Howe: *An integrated CMOS micromechanical resonator high-Q oscillator*, Solid-State Circuits, IEEE Journal of, vol. 34, pp. 440–455, 1999
7. L. Yu-Wei, L. Seungbae, L. Sheng-Shian, X. Yuan, R. Zeying, and C. T. C. Nguyen: *Series-resonant VHF micromechanical resonator reference oscillators*, Solid-State Circuits, IEEE Journal of, vol. 39, pp. 2477–2491, 2004
8. L. Seungbae and C. T. C. Nguyen: *Influence of automatic level control on micromechanical resonator oscillator phase noise*, in Frequency control symposium and pda exhibition jointly with the 17th european frequency and time forum, 2003. proceedings of the 2003 ieee international, pp. 341–349, 2003
9. D. Grogg, F. Lo Conte, M. Kayal, A. M. Ionescu: *9 MHz Vibrating Body FET Tuning Fork Oscillator*, EFTF-IFCS, Besançon, 2009
10. F. Lo Conte, D. Grogg, A. M. Ionescu, M. Kayal: *High-Quality factor MEMS based oscillator*, MIXDES, Łódź, 2009
11. D. Grogg, C. Meinen, D. Tsamados, H. C. Tekin, M. Kayal, and A. M. Ionescu: *Double gate movable body Micro-Electro-Mechanical FET as hysteretic switch: Application to data transmission systems*, in Solid-State Device Research Conference, 2008. ESSDERC 2008. 38th European, pp. 302–305, 2008
12. M. Blagojevic, M. Pastre, M. Kayal, P. Fazan, S. Okhonin, M. Nagoga, M. Declercq:, *SOI Capacitor-Less 1-Transistor DRAM Sensing Scheme with Automatic Reference Generation*, IEEE Symposium on VLSI Circuits, pp. 182–183, June 2004
13. M. Blagojevic, M. Kayal, M. Pastre, L. Harik, S. Okhonin, P. Fazan: *Capacitor-Less 1T DRAM Sensing Scheme with Automatic Reference Generation*, IEEE Journal of Solid-State Circuits (JSSC), Vol. 41, pp. 1463–1470, June 2006
14. M. Pastre, M. Kayal, H. Blanchard: *A Hall Sensor Analog Front End for Current Measurement with Continuous Gain Calibration*, IEEE Sensors Journal, Special Edition on Intelligent Sensors, Vol. 7, Number 5, pp. 860–867, May 2007
15. V. Kaajakari, T. Mattila, A. Oja, and H. A. S. H. Seppa: *Nonlinear limits for single-crystal silicon microresonators*, Microelectromechanical Systems, Journal of, vol. 13, pp. 715–724, 2004
16. M. Agarwal, S. A. Chandorkar, H. Mehta, R. N. Candler, B. Kim, M. A. Hopcroft, R. Melamud, C. M. Jha, G. Bahl, G. Yama, T. W. Kenny, and B. Murmann: *A study of electrostatic force nonlinearities in resonant microstructures*, Applied Physics Letters, vol. 92, no. 10, pp. 104 106–3, 2008
17. V. Kaajakari, J. K. Koskinen, T. Mattila: *Phase Noise in Capacitively Coupled Micromechanical Oscillators*, Ultrasonics, Ferroelectrics and Frequency Control, IEEE Transactions on, vol. 52, pp. 2322–2331, 2005

n
a
d
c
v

K

Let p b
is said
$x^2 \equiv$
given p
modulo
non-res
taking a
modulo
More p
one can

* Th
grant no.

ELECTRONICS AND TELECOMMUNICATIONS QUARTERLY, 2009, 55, no 4, pp. 639–647

On the average of the least quadratic non-residue modulo a prime number*

ANDRZEJ PASZKIEWICZ

Warsaw University of Technology
e-mail: anpa@tele.pw.edu.pl

Received 2009.10.13
Authorized 2009.11.16

In this paper we focus on a problem of existence the mean value of the least quadratic non-residue modulo a prime number. We prove that the answer to that question is positive and calculate the exact value of that constant with high accuracy. We also prove that the density of all primes having its least quadratic non-residue equal to k-th prime is $1/2^k$. Some computational results are included to provide numerical arguments that the convergence is very fast.

Keywords: Least quadratic non-residue, multiplicative group modulo a prime number, least primitive root, primality testing algorithms

1. INTRODUCTION

Let p be a prime number greater than 2 and $n_2(p)$ its least quadratic non-residue. It is said that a is quadratic non-residue modulo p if it is a solution of the equation $x^2 \equiv a \pmod{p}$, otherwise we call a quadratic residue. It is well known that for a given prime number p the numbers of quadratic residues and quadratic non-residues modulo p are equal [5]. It is a great practical interest to consider quadratic residues or non-residues. Many algorithms for testing primality a given positive odd integer N or taking a square root modulo N assume the existence of a small quadratic non-residue modulo N. In fact such a small quadratic non-residue exists by special assumptions. More precisely by the assumption of the Extended Riemann Hypothesis (ERH) [1] one can show that $n_2(N) \leq 2 \cdot (\log N)^2$, where $\log N$ denote natural logarithm. This

* This paper was supported by the Ministry of Science and Higher Education of Poland – research grant no. N517 003 32/0583 for 2007-2010

provides, for example, a fundamental for the following short and excellent conditional algorithm for testing primality of N in polynomial time with respect to $\log N$. This is in fact a non random version of the famous Solovay Strassen test [10],[8],[6].

Testing primality of N

/returns "prime" for N being a prime number, otherwise returns "composite"/

Input: N an odd integer greater than 2
for $a = 2$ to $2 \cdot (\log N)^2$ do
{
if $\gcd(a, N) \neq 1$ then return "composite"
else
if $\left(\frac{a}{N}\right) \equiv a^{(N-1)/2} \pmod{N}$ then return "composite"
}
return "prime"

The two argument function $\left(\frac{a}{N}\right)$ where N is a positive odd integer denote the Jacobi symbol [1],[5],[8]. It has to be pointed out, that $n_2(p)$ is a prime number. This simple fact actually allows to save a lot of time when searching the least quadratic non-residue.

Many recent theoretical and computational investigations show, that $n_2(p)$ is really very slowly growing function. In 1949, Friedlander [3] and Salié [9] independently showed that $n_2(p) = \Omega(\log p)$, which means, that there are infinitely many primes p, such that $n_2(p) \geq c \cdot \log p$ for some absolute constant c. In 1971 Montgomery [7] showed that if the Generalized Riemann Hypothesis is true, then $n_2(p) = \Omega(\log p \log\log p)$. Graham and Ringrose [4] showed unconditionally a weaker result: $n_2(p) = \Omega(\log p \log\log\log p)$. That means, $n_2(p)$ cannot be majorized by any logarithmic function. Recently author of this paper within the scope of a distributed Internet project[1] computed $n_2(p)$ for all primes below 10^{16}. These computations show that for primes p less than 10^{16} the corresponding to it the least quadratic non-residue $n_2(p)$ does not exceed 223.

2. THE DENSITY OF PRIMES WITH A GIVEN LEAST QUADRATIC NON-RESIDUE

As it has been remarked before, the least quadratic non-residue $n_2(p)$ is a prime number. This fact follows from the multiplicativity of the Legendre symbol [5]. The property

[1] A. Paszkiewicz, The least quadratic non-residue, a computational point of view. (to be published)

$\left(\frac{2}{p}\right) = (-1)^{(p-1)(p+1)/8}$ imply that $\left(\frac{2}{p}\right) = -1$ for all prime numbers p of the form $8k+3$ or $8k+5$ and $\left(\frac{2}{p}\right) = 1$ for primes p of the form $8k+1$ or $8k+7$. That means that for primes p in the arithmetic progressions of the form $8k+3$ or $8k+5$ corresponding to it $n_2(p) = 2$. For primes p contained in the remained arithmetic progressions $8k+1$ and $8k+7$ the number 2 is a quadratic residue. From Dirichlet's theorem it follows, that primes in arithmetic progressions $ak + b$ with coprime positive integers a, b are uniformly distributed [8] it follows that primes in the progressions 8k+3 and 8k+5 for which 2 is the least quadratic non-residue cover exactly one half of all primes. That is the density of primes for which 2 is the least quadratic non-residue equals to 1/2. Consider now the progressions $8k+1$ and $8k+7$. For all primes contained in these progressions 2 is a quadratic residue. We ask now, what is the density of primes for which 3 is the least quadratic non residue. All we need is to resolve two equations $\left(\frac{3}{8k+1}\right) = -1$ and $\left(\frac{3}{8k+7}\right) = -1$ for primes p of the form $8k+1$ and $8k+7$.. Let us consider the first case. By Gauss theorem (Gauss quadratic reciprocity law, see [5]) we have $\left(\frac{3}{8k+1}\right) = (-1)^{\frac{3-1}{2}\,\frac{8k+1-1}{2}}\left(\frac{8k+1}{3}\right) = \left(\frac{8k+1}{3}\right)$. The last is equal to -1 if and only if $8k+1$ is quadratic non-residue modulo 3, that means $8k+1$ is congruent to 2 modulo 3 or other words $8k$ is congruent to 1 modulo 3. This equation can be easily solved by the aid of Chinese Remainder Theorem. By that theorem we find the parameter k should be of the form $3t+2$ for an integer t and finally $8k+1=8(3t+2)+1=24t+17$. So we stated that for all primes in the sub-progression $24t+17$ of the arithmetical progression $8k+1$ the least quadratic non-residue is 3. For the sub-progression of the form $24t+1$ (found by analogy) we see that 2 and 3 are quadratic residues. By the same way the progression $8k+7$ can be split into two sub-progressions of the form $24t+7$ and $24t+23$ respectively. For the first one each prime of the form $24t+7$ has its least quadratic non-residue equal to 3 and for each prime of the form $24t+23$ the numbers 2 and 3 are quadratic residues. Again all primes in arithmetic progressions $8k+7$ for which 2 is quadratic residue were split into progressions for which 3 is quadratic non-residue and the remained progressions for which 2 and 3 are quadratic residues. We see that these considerations can be extended.

While working on the general conclusion we produced the five tables below which contain the distribution of primes into disjoint arithmetic progressions containing primes for which initial primes numbers are least quadratic non-residues.

Table 1

PROGRESSIONS FOR WHICH 2 IS THE LEAST QUADRATIC NON-RESIDUE (BOLD LETTERS)

$8k+1$	**$8k+3$**	**$8k+5$**	$8k+7$

Table 2

PROGRESSIONS FOR WHICH 3 IS THE LEAST QUADRATIC NON-RESIDUE (BOLD LETTERS)

$8k+1$		$8k+7$	
$24k+1$	**$24k+17$**	**$24k+7$**	$24k+23$

Table 3

PROGRESSIONS FOR WHICH 5 IS THE LEAST QUADRATIC NON-RESIDUE (BOLD LETTERS)

$24k+1$				$24k+23$			
$120k+1$	$120k+49$	**$120k+73$**	**$120k+97$**	**$120k+23$**	**$120k+47$**	$120k+71$	$120k+119$

Table 4

PROGRESSIONS FOR WHICH 7 IS THE LEAST QUADRATIC NON-RESIDUE (BOLD LETTERS)

$120k+1$						$120k+49$					
$840k+1$	$840k+121$	$840k+361$	**$840k+241$**	**$840k+481$**	**$840k+601$**	**$840k+409$**	**$840k+649$**	**$840k+769$**	$840k+169$	$840k+289$	$840k+529$

Table 5

PROGRESSIONS FOR WHICH 7 IS THE LEAST QUADRATIC NON-RESIDUE (BOLD LETTERS)

$120k+71$						$120k+119$					
$840k+311$	$840k+551$	$840k+671$	**$840k+71$**	**$840k+191$**	**$840k+431$**	**$840k+239$**	**$840k+359$**	**$840k+599$**	$840k+479$	$840k+719$	$840k+839$

Denote by E_k the density of all primes for which $n_2(p) = p_k$, that is the following limit:

$$E_k = \lim_{x\to\infty} \frac{1}{\pi(x)} \sum_{p<x,\ n_2(p)=p_k} 1 \tag{1}$$

where $\pi(x)$ is the number of primes below x. Now we are able to formulate and prove the following theorem.

THEOREM 1. Let p_k be the k-th prime. The density E_k of all primes p for which $n_2(p) = p_k$ equals to $\frac{1}{2^k}$.

Proof. As we have seen our theorem is true for the initial four primes p_k. We apply mathematical induction to the proof. In our construction described above we created in the k-th step two sets of arithmetical progressions. One set consisting of those progressions for which the initial primes $p_1, p_2, \ldots, p_{k-1}$ were quadratic residues for primes in that progressions. Then for each such progression we constructed two new sub-progressions, one – such that for each prime in that sub-progression the number

p_k. is a quadratic residue and the second such that p_k. is a quadratic non-residue. By the Chinese Remainder Theorem every arithmetical progression obtained in the k-th step is of the form $8p_2p_3...p_k \cdot a + b$. Let b be chosen so that $8p_2p_3...p_k \cdot a + b$ is quadratic residue modulo primes p_i for initial $i = 1, 2, ..., k$ and n is one of the $\frac{p_{k+1} - 1}{2}$ quadratic non-residues modulo p_{k+1}. Now we can solve the equation $8p_2p_3...p_k \cdot a + b \equiv n (\mathrm{mod}\, p_{k+1})$. It follows by induction that $\frac{1}{2}$ of all solutions of the congruence are just quadratic non-residues modulo p_{k+1} which are the same time quadratic residues modulo primes p_i for initial $i = 1, 2, ..., k$. That is for $\frac{1}{2} \cdot \frac{1}{2^k} = \frac{1}{2^{k+1}}$ of all primes p_{k+1} is the least quadratic non-residue. This finishes the proof by induction.

With minor modification the above theorem can by generalized.

THEOREM 2. Let $\varepsilon_1, \varepsilon_2, ..., \varepsilon_k$ be any finite sequence of numbers chosen from the set {1,-1}. The density $E_{\varepsilon_1,\varepsilon_2,...,\varepsilon_k}$ of all prime numbers p for which $\left(\frac{p_i}{p}\right) = \varepsilon_i$ equals to $\frac{1}{2^k}$.

The proof is very similar to the proof of THEOREM 1.

3. THE AVERAGE OF THE LEAST QUADRATIC NON-RESIDUE

Let E be the mean value of the least quadratic non-residue, that is the limit

$$E = \lim_{x\to\infty} \frac{1}{\pi(x)} \sum_{p<x} n_2(p). \tag{2}$$

We will show, that the limit (1) exists and calculate it with high accuracy. By simple transformations we have:

$$E = \lim_{x\to\infty} \frac{1}{\pi(x)} \sum_{p<x} n_2(p) = \lim_{x\to\infty} \frac{1}{\pi(x)} \sum_{\substack{p < x \\ n_2(p) = p_k}} 1 = \sum_{k=1}^{\infty} E_k.$$

$$E = \sum_{k=1}^{\infty} \frac{p_k}{2^k}. \tag{3}$$

LEMMA 1. Let p_k be the k-th prime. For $k \geq 3$ the following inequality is valid

$$p_k \leq k(k-1). \tag{4}$$

Proof. It is easy to check that the inequality (4) is valid for $k = 3, 4$ and 5. It is proved more sharp inequality for p_k (see [8])

$$p_k \leq k \log(k \log k) \tag{5}$$

for all $k \geq 6$. Combining(4) and (5) it suffices to show that $\log(k \log k) \leq k - 1$. Let $f(x)$ be a real function defined as follows: $f(x) = \log(x \log x) - x + 1$. We have $f(e) = 2 - e < 0$, where e is the basis of the natural logarithm. Differentiating $f(x)$ we obtain $f'(x) = \frac{1}{x} + \frac{1}{x \log x} - 1$. For $x > e$ we have $f'(x) < f'(e) = \frac{1}{e} + \frac{1}{e \log e} - 1 < \frac{2-e}{e}$ and the right side of the last inequality is negative thus $f(x)$ is a monotone falling function for $x > e$. This finishes the proof.

LEMMA 2. For $N \geq 3$ the following equality holds

$$\sum_{k=N}^{\infty} \frac{k(k-1)}{2^k} = \frac{N^2 + N + 2}{2^{N-1}} \tag{6}$$

An easy proof by the aid of differential calculus we omit.

CONCLUSION. The average value E of the least quadratic non-residue is equal

$$E = 3,67464396601132877899567 6 \tag{7}$$

with an error not exceeding 10^{-26}.

Proof. For N=97 the right hand side of (6) becomes less than 10^{-26} so at least 25 decimal digits of $\sum_{k=1}^{96} \frac{p_k}{2^k}$ are exact.

4. NUMERICAL INVESTIGATIONS AND CONCLUSIONS

By computations we tabulated the functions E_k (k=1,...,25) with the step 10^9 for the initial 1000 steps. The results are illustrated on the following 5 Figures. One can observe very fast convergence of that functions to the values $\frac{1}{2^k}$ guaranteed by the THEOREM 1. It is interesting to remark that the investigation time for each interval of the length 10^9 is between 6 up to 22 seconds including the sieving procedure used for testing primality and determining the least quadratic non residue of each prime number. The computations were performed on a few modern IBM PC computers running under Windows XP operation systems. These investigations comprise a small part of vast Internet search performed in the 2006, 2007 and 2008 years.

All software used to computations were tested several times, mainly within students' semestral projects.

It is a bit strength that, as we have seen it, is quite simple to prove the existence of the mean value of the least quadratic non-residue and it is almost impossible to do the same for the least primitive roots. Many authors suggested that the average of the least primitive root has a finite limit [2] but nobody proved it.

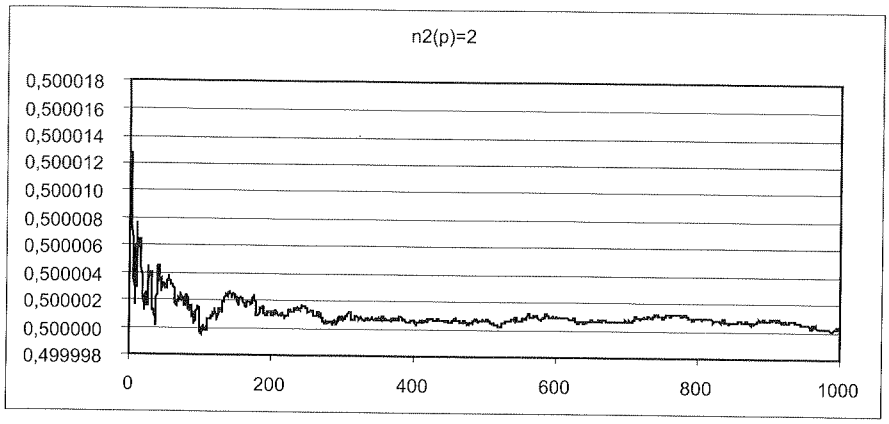

Fig. 1. Graph of the function E_1

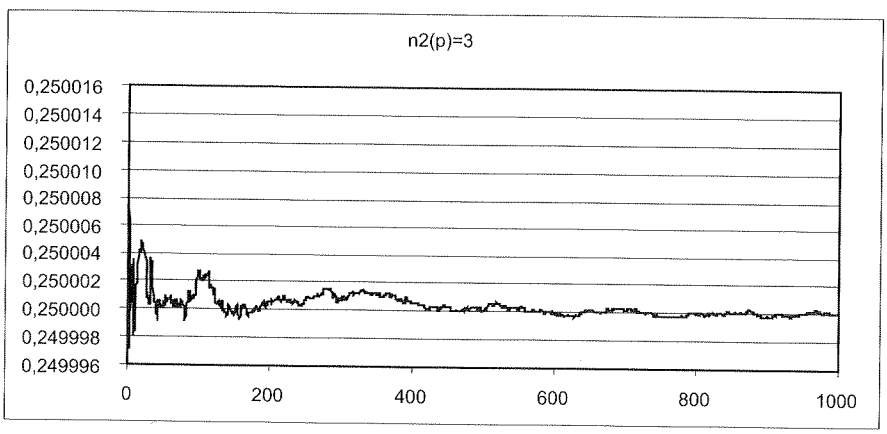

Fig. 2. Graph of the function E_2

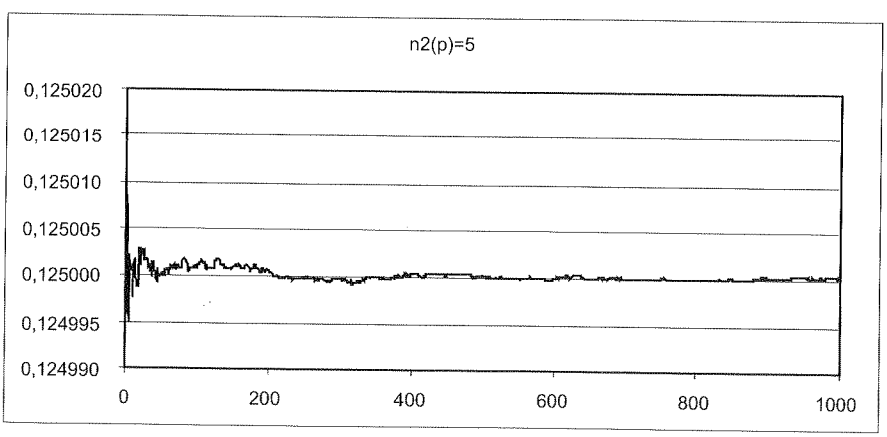

Fig. 3. Graph of the function E_3

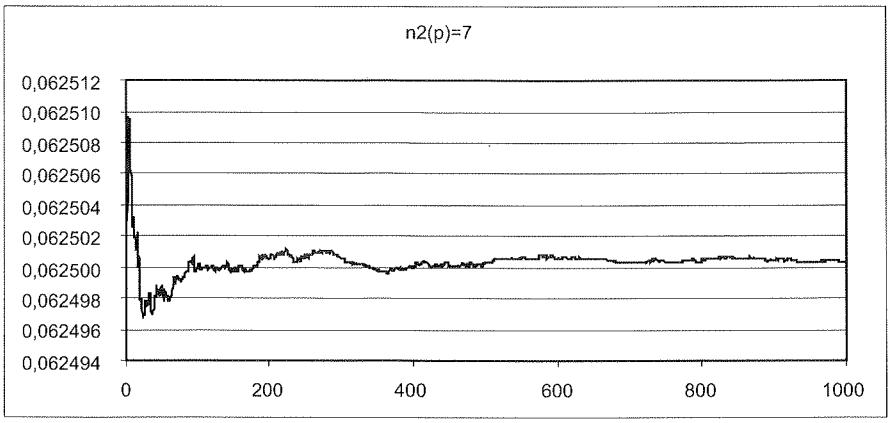

Fig. 4. Graph of the function E_4

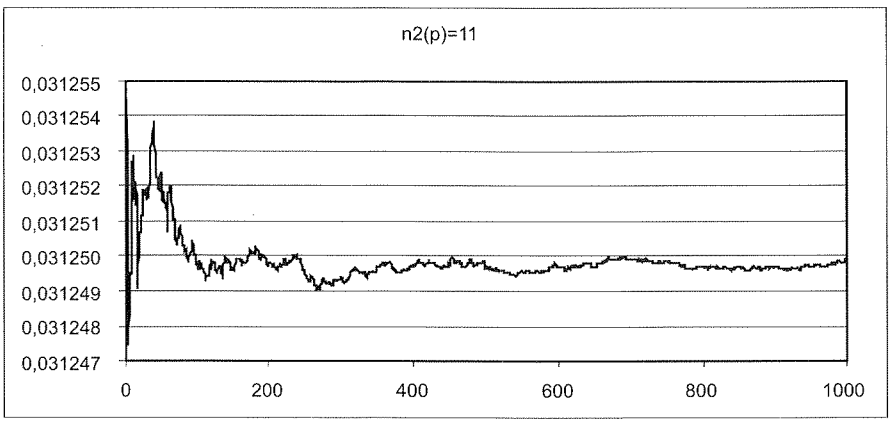

Fig. 5. Graph of the function E_5

REFERENCES

1. R. Crandall, C. Pomerance: *Prime Numbers, a Computational Perspective*, Springer Verlag New York, Berlin, 2001
2. P. D. T. A. Elliott, L. Murata: *On the average value of the least primitive root modulo p*, J. London Math. Soc. 56 (2), pp. 435–454, 1997
3. V. R. Friedlander: *On the least n-th power non-residue*, Dokl. Akad. Nauk SSSR 66, pp. 351–352, 1949
4. S. W. Graham, C. J. Ringrose: *Lower bounds for least quadratic non-residues,* Analytic Number Theory, Proceedings in Honor of Paul T. Bateman, Progress in Mathematics 85, Birkhäuser, Boston, pp. 269–309, 1990
5. K. Ireland, M. Rosen: *A Classical Introduction to modern Number Theory*, Springer-Verlag, New York, Heidelberg, Berlin, 1982, Graduate Texts in Mathematics, 87
6. A. Menezes et all: *Handbook of Applied Cryptography*, CRC Press, Boca Raton, 1997
7. H. L. Montgomery: *Topics in Multiplicative Number Theory*, Lecture Notes in Math. Springer Verlag, New York, 1971

8. H. Riesel: *Prime Numbers and Computer Methods for Factorizations*, 2nd ed., Birkhäuser, Boston, Basel, Berlin 1994
9. H. Salié: *Über den kleinsten positiven quadratischen Nichtrest nach einer Primzahl*, Math. Nachr. 3, pp. 7–8, 1949
10. R. M. Solovay, V. Strassen: *A fast Monte-Carlo test for primality*, SIAM Journal on Computing, 6(1), pp. 84–85, 1971

O

m
m
el

Ke

It is
group Z
and k a
prime n
can obse
for p^k, v
$g(p)$ and
By theor
modulo
a given
primitive
is a prim
densities

* This
grant no. N

ELECTRONICS AND TELECOMMUNICATIONS QUARTERLY, 2009, 55, no 4, pp. 649–658

On the least primitive root modulo $2p$ for odd primes p*

ANDRZEJ PASZKIEWICZ

Warsaw University of Technology
e-mail: anpa@tele.pw.edu.pl

Received 2009.10.13
Authorized 2009.11.16

In this paper we present results of numerical investigations concerning primitive roots modulo $m = 2p$, where p is prime greater than 2. This is one of these cases of integers m for which the multiplicative group of primitive rests modulo m can be generated by one element. Our computations comprise all primes below 10^{10}.

Keywords: Multiplicative group modulo an integer m, the least primitive root, cyclic groups, generator of a group

1. INTRODUCTION

It is well known since Gauss, that the only modulus m for which the multiplicative group Z_m^* is cyclic, belong to the set $\{2, 4, p^k, 2p^k\}$, where p is prime greater than 2 and k a positive integer [1]. In [2] we showed some results concerning densities of prime numbers p, such that i-th prime p_i is the least primitive root modulo $2p$. One can observe that for most primes p their least primitive roots $g(p)$ are also the same for p^k, with $k > 1$. For $p < 10^{12}$ there exist only two exceptional primes p for which $g(p)$ and $h(p)$ differ ($h(p)$ denote the least primitive root mod p^2, see [4] for details). By theorem of Jacobi [1] if g is primitive root modulo p^2 then it is also primitive root modulo p^k for all $k \geq 2$. Our current interest addresses the densities of primes with a given least primitive root modulo $2p$, that is we remove the constraint for the least primitive root to be a prime. A number a is a primitive root modulo $2p$ if a is odd and is a primitive root modulo p. We are not able to derive concrete formulas for these densities such as in [2] or [3] but by computer investigations we can approximate the

* This paper was supported by the Ministry of Science and Higher Education of Poland – research grant no. N517 003 32/0583 for 2007-2010

densities of primes with its least primitive roots equal to a given initial odd integers greater than 1.

2. COMPUTER INVESTIGATIONS AND RESULTS

Let $D_2^*(n,x)$ and $D_2^*(x)$ be two functions defined as follows

$$D_2^*(n,x) = \frac{1}{\pi(x)} \sum_{p<x, g(2p)=n} 1 \tag{1}$$

$$D_2^*(x) = \frac{1}{\pi(x)} \sum_{p<x} g(2p). \tag{2}$$

The first function is a natural density of primes below x, with the least primitive root modulo $2p$ equal to n and the second, the average value of the least primitive root modulo $2p$ extended over primes below the limit x. We tabulated both functions with the step 10^8 up to the limit $x < 10^{10}$ and $n \leq 39$. All results of our computations are illustrated in Figures 1-17 and Tables 1 and 2.

All computations were performed on one powerful PC computer with Pentium processor running on Linux operation system. The experiment has finished after approximately one day of computation.

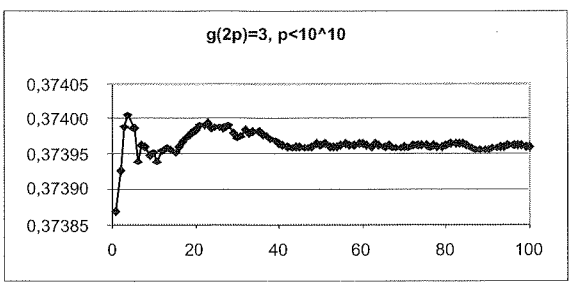

Fig. 1.

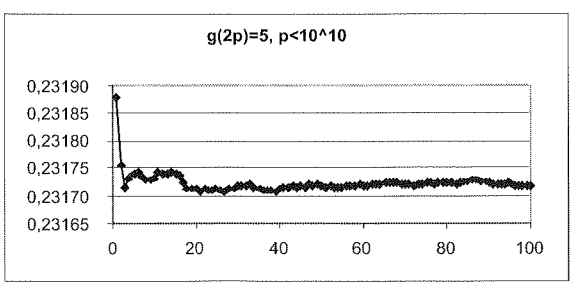

Fig. 2.

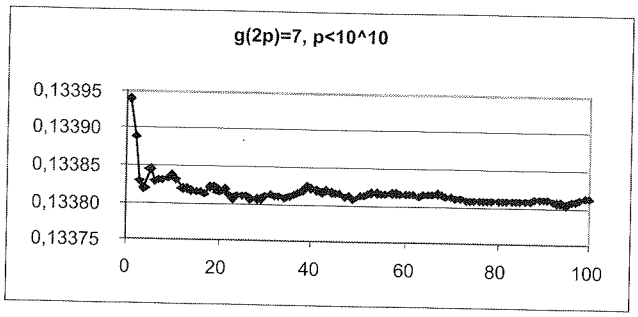

Fig. 3.

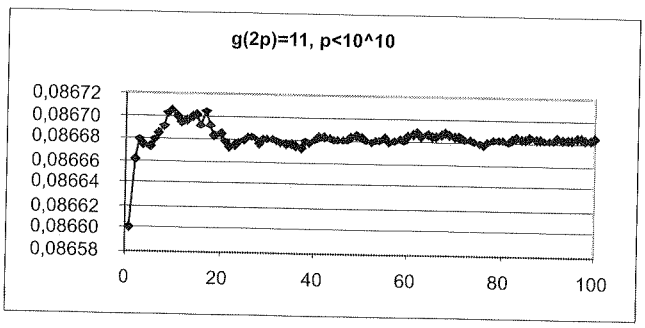

Fig. 4.

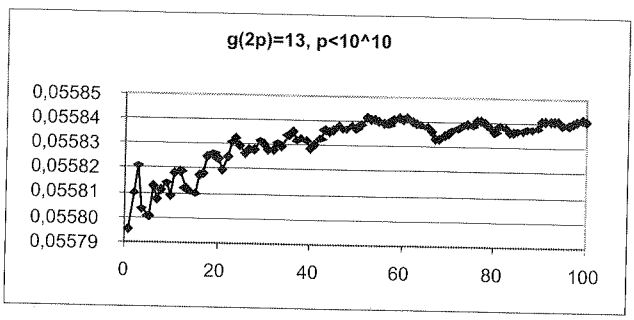

Fig. 5.

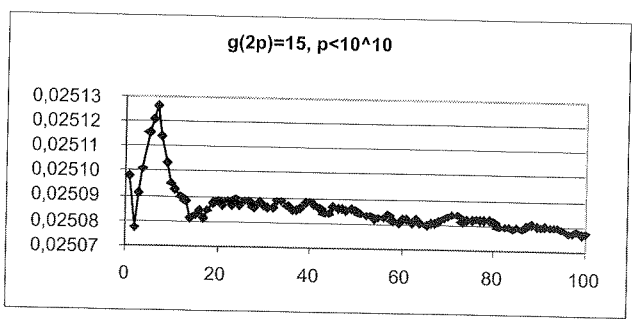

Fig. 6.

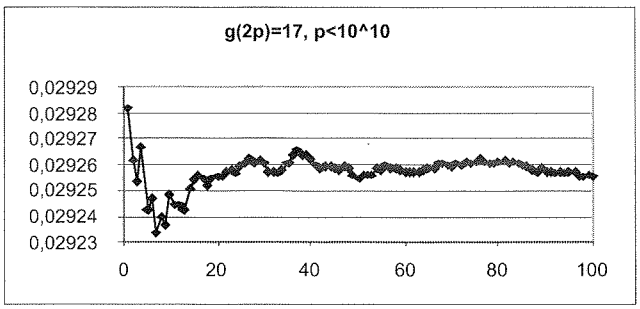

Fig. 7.

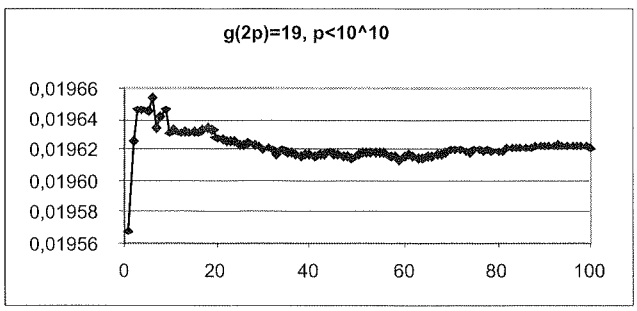

Fig. 8.

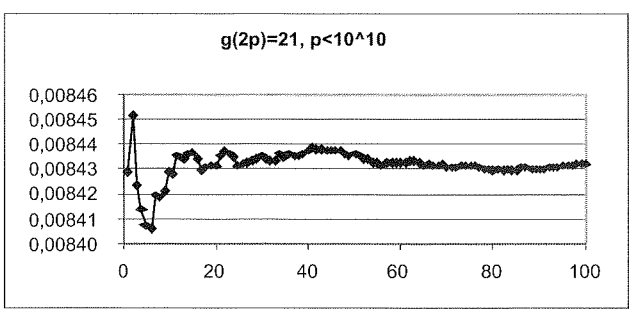

Fig. 9.

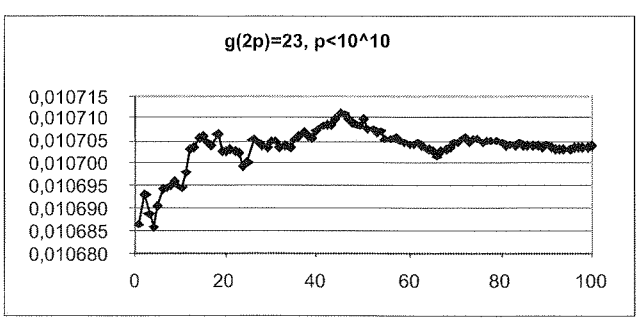

Fig. 10.

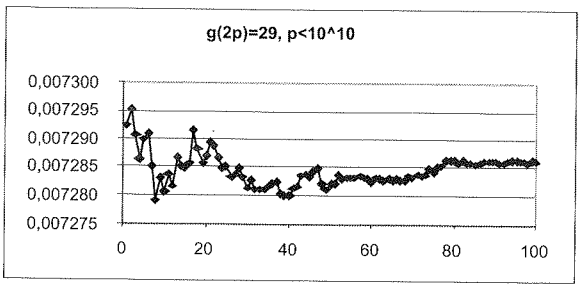

Fig. 11.

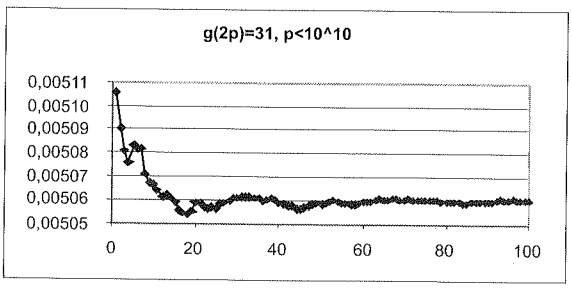

Fig. 12.

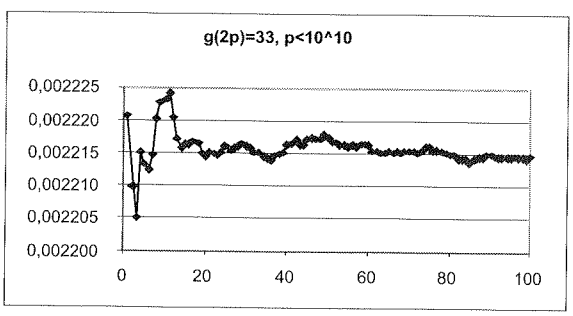

Fig. 13.

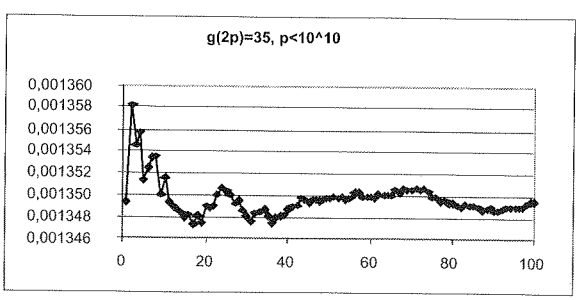

Fig. 14.

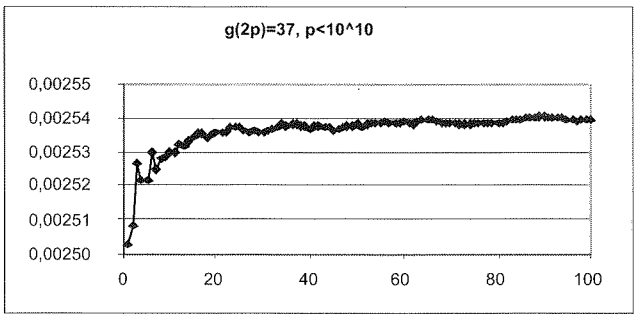

Fig. 15.

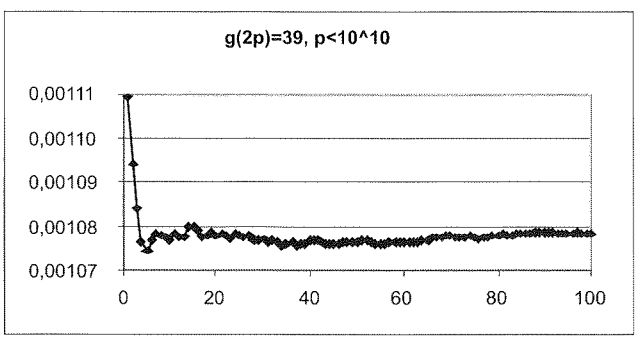

Fig. 16.

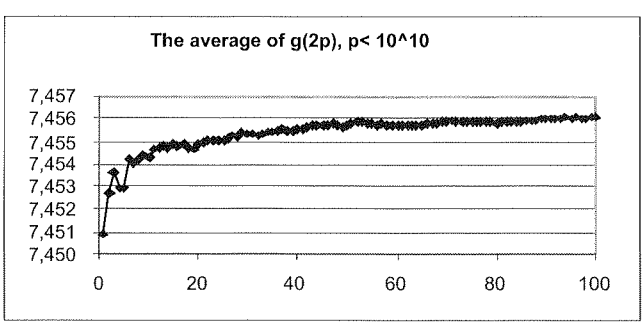

Fig. 17.

Table 1

THE FIRST OCCURRENCES OF PRIMES WITH $g(2p) = n$, FOR INITIAL n

$g(2p)$	$G(2p)$	$G(p)$	$g(p)$	p	$p-1$
5	5	5	5	23	$2\cdot11$
7	7	2	2	11	$2\cdot5$
11	11	2	2	59	$2\cdot29$
13	13	13	13	457	$2^3\cdot3\cdot19$
15	43	43	6	271	$2\cdot3^3\cdot5$
17	17	2	2	131	$2\cdot5\cdot13$
19	19	19	19	191	$2\cdot5\cdot19$
21	23	2	2	181	$2\cdot3^2\cdot5$
23	23	2	2	421	$2^2\cdot3\cdot5\cdot7$
29	29	2	2	1453	$2^2\cdot3\cdot11^2$
31	31	31	10	1021	$2^2\cdot3\cdot5\cdot17$
33	47	2	2	1531	$2\cdot3^2\cdot517$
35	37	2	2	1171	$2\cdot3^2\cdot5\cdot13$
37	37	2	2	3877	$2^2\cdot3\cdot17\cdot19$
39	43	2	2	9661	$2^2\cdot3\cdot5\cdot7\cdot23$
41	41	41	6	1811	$2\cdot5\cdot181$
43	43	43	14	8011	$2\cdot3^2\cdot5\cdot89$
45	47	2	2	306517	$2^2\cdot3\cdot7\cdot41\cdot89$
47	47	2	2	32341	$2^2\cdot3\cdot5\cdot7^2\cdot11$
51	67	67	6	57991	$2\cdot3\cdot5\cdot1933$
53	53	2	2	14821	$2^2\cdot3\cdot5\cdot13\cdot19$
55	67	2	2	54181	$2^2\cdot3^2\cdot5\cdot7\cdot43$
57	67	2	2	33301	$2^2\cdot3^2\cdot5^2\cdot37$
59	59	59	6	214141	$2^2\cdot3\cdot5\cdot43\cdot83$
61	61	2	2	136501	$2^2\cdot3\cdot5^3\cdot7\cdot13$
63	71	2	2	1035061	$2^2\cdot3\cdot5\cdot13\cdot1327$
65	89	2	2	608941	$2^2\cdot3^2\cdot5\cdot17\cdot199$
67	67	2	2	136621	$2^2\cdot3^3\cdot5\cdot11\cdot23$
69	83	83	69	110881	$2^5\cdot3^2\cdot5\cdot7\cdot11$
71	71	71	22	221101	$2^2\cdot3\cdot5^2\cdot11\cdot67$

cd. Table 1

$g(2p)$	$G(2p)$	$G(p)$	$g(p)$	p	$p-1$
73	73	2	2	385141	$2^2 \cdot 3 \cdot 5 \cdot 7^2 \cdot 131$
75	83	2	2	21267091	$2 \cdot 3^3 \cdot 5 \cdot 1373 \cdot 83$
77	101	101	34	2057701	$2^2 \cdot 3 \cdot 5^2 \cdot 19^3$
79	79	2	2	174931	$2 \cdot 3 \cdot 5 \cdot 7^3 \cdot 17$
83	83	83	10	394549	$2^2 \cdot 3 \cdot 7^2 \cdot 11 \cdot 61$
85	101	101	10	1445137	$2^4 \cdot 3 \cdot 7 \cdot 11 \cdot 17 \cdot 23$
87	97	97	44	71761	$2^4 \cdot 3 \cdot 5 \cdot 13 \cdot 23$
89	89	2	2	1709341	$2^2 \cdot 3 \cdot 5 \cdot 31 \cdot 919$
91	101	101	26	6146281	$2^3 \cdot 3^4 \cdot 5 \cdot 7 \cdot 271$
93	107	2	2	267901	$2^2 \cdot 3 \cdot 5^2 \cdot 19 \cdot 47$
95	101	2	2	2535331	$2 \cdot 3 \cdot 5 \cdot 7 \cdot 12073$
97	97	97	74	8954401	$2^5 \cdot 3 \cdot 5^2 \cdot 7 \cdot 13 \cdot 41$
99	109	109	58	4326841	$2^3 \cdot 3^2 \cdot 5 \cdot 7 \cdot 17101$
101	101	101	26	3126061	$2^2 \cdot 3^3 \cdot 5 \cdot 7 \cdot 827$
103	103	103	86	7415641	$2^3 \cdot 3^2 \cdot 5 \cdot 20599$
105	109	109	22	92019721	$2^3 \cdot 3 \cdot 5 \cdot 13 \cdot 61 \cdot 967$
107	107	107	10	7485949	$2^2 \cdot 3^2 \cdot 23 \cdot 9041$
109	109	109	46	7337521	$2^4 \cdot 3^3 \cdot 5 \cdot 43 \cdot 79$
111	127	127	94	10126561	$2^5 \cdot 3 \cdot 5 \cdot 17^2 \cdot 73$
113	113	113	34	3466681	$2^3 \cdot 3 \cdot 5 \cdot 7 \cdot 4127$
115	131	131	10	3248701	$2^2 \cdot 3 \cdot 5^2 \cdot 7^2 \cdot 13 \cdot 17$
117	137	2	2	256181941	$2^2 \cdot 3^4 \cdot 5 \cdot 7 \cdot 19 \cdot 29 \cdot 41$
119	127	127	34	44499841	$2^7 \cdot 3 \cdot 5 \cdot 7^2 \cdot 11 \cdot 43$
127	127	2	2	13681669	$2^2 \cdot 3 \cdot 7 \cdot 11 \cdot 13 \cdot 17 \cdot 67$
129	149	2	2	42090469	$2^2 \cdot 3 \cdot 7 \cdot 501077$
131	131	131	34	62461141	$2^2 \cdot 3 \cdot 5 \cdot 7 \cdot 127 \cdot 1171$
133	173	173	18	16135981	$2^2 \cdot 3 \cdot 5 \cdot 7 \cdot 103 \cdot 373$
137	137	2	2	222587821	$2^2 \cdot 3^2 \cdot 5 \cdot 7 \cdot 13 \cdot 107 \cdot 127$
139	139	139	14	179296261	$2^2 \cdot 3 \cdot 5 \cdot 11 \cdot 13 \cdot 20897$
141	179	179	94	5109721	$2^3 \cdot 3 \cdot 5 \cdot 7^2 \cdot 11 \cdot 79$
143	163	163	26	595802761	$2^3 \cdot 3 \cdot 5 \cdot 7^2 \cdot 19 \cdot 5333$

cd. Table 1

$g(2p)$	$G(2p)$	$G(p)$	$g(p)$	p	$p-1$
145	157	157	22	364511281	$2^4 \cdot 3 \cdot 5 \cdot 7 \cdot 17 \cdot 12763$
149	149	149	10	58261141	$2^2 \cdot 3^3 \cdot 5 \cdot 7 \cdot 15413$
151	151	151	10	83248621	$2^2 \cdot 3 \cdot 5 \cdot 7 \cdot 13 \cdot 79 \cdot 193$
153	181	181	34	921754681	$2^3 \cdot 3 \cdot 5 \cdot 7^2 \cdot 11 \cdot 14251$
155	167	167	22	1244418421	$2^2 \cdot 3 \cdot 5 \cdot 7 \cdot 29 \cdot 71 \cdot 1439$
157	157	157	10	637531021	$2^2 \cdot 3^3 \cdot 5 \cdot 7 \cdot 23 \cdot 7333$
159	193	2	2	111657781	$2^2 \cdot 3^2 \cdot 5 \cdot 13 \cdot 47717$
161	199	199	14	3375480109	$2^2 \cdot 3 \cdot 7 \cdot 11 \cdot 13 \cdot 97 \cdot 2897$
163	163	163	46	1105235041	$2^5 \cdot 3 \cdot 5 \cdot 7 \cdot 13 \cdot 25303$
165	181	181	34	1522917901	$2^2 \cdot 3^2 \cdot 5^2 \cdot 7 \cdot 53 \cdot 4561$
167	167	2	2	492484381	$2^2 \cdot 3 \cdot 5 \cdot 29 \cdot 383 \cdot 739$
173	173	2	2	34534501	$2^2 \cdot 3 \cdot 5^3 \cdot 7 \cdot 11 \cdot 13 \cdot 23$
177	193	2	2	3553214701	$2^2 \cdot 3 \cdot 5^2 \cdot 7 \cdot 19^2 \cdot 43 \cdot 109$
179	179	179	62	1296499681	$2^5 \cdot 3^2 \cdot 5 \cdot 7 \cdot 128621$
181	181	181	24	3656862301	$2^2 \cdot 3 \cdot 5^2 \cdot 7 \cdot 13 \cdot 29 \cdot 31 \cdot 149$
183	227	227	26	2628596041	$2^3 \cdot 3 \cdot 5 \cdot 7 \cdot 19 \cdot 109 \cdot 1511$
185	193	193	148	899978641	$2^4 \cdot 3 \cdot 5 \cdot 11^2 \cdot 17 \cdot 1823$
191	191	2	2	924143221	$2^2 \cdot 3^2 \cdot 5 \cdot 7 \cdot 11 \cdot 13 \cdot 23 \cdot 223$
193	193	193	14	1623140821	$2^2 \cdot 3^2 \cdot 5 \cdot 7 \cdot 23 \cdot 56009$
197	197	197	194	7111268641	$2^5 \cdot 3^5 \cdot 5 \cdot 7 \cdot 17 \cdot 29 \cdot 53$
199	199	2	2	3113516701	$2^2 \cdot 3^2 \cdot 5^2 \cdot 7 \cdot 19^2 \cdot 37^2$
201	251	251	6	4364040781	$2^2 \cdot 3^3 \cdot 5 \cdot 11 \cdot 734687$
203	211	211	26	565093981	$2^2 \cdot 3^2 \cdot 5 \cdot 11 \cdot 41 \cdot 6961$
205	211	211	82	1968157129	$2^3 \cdot 3 \cdot 7^2 \cdot 43 \cdot 38921$
215	227	227	6	3418629061	$2^2 \cdot 3 \cdot 5 \cdot 7^2 \cdot 11 \cdot 37 \cdot 2857$
221	233	233	106	3421699681	$2^5 \cdot 3 \cdot 5 \cdot 7 \cdot 229 \cdot 4447$
223	223	223	6	5205777061	$2^2 \cdot 3 \cdot 5 \cdot 11 \cdot 17 \cdot 463973$
227	227	2	2	3129270901	$2^2 \cdot 3 \cdot 5^2 \cdot 7 \cdot 1490129$

Table 2

APPROXIMATE VALUES OF DENSITIES OF PRIMES p WITH $g(2p) = n$

n	$D_2^*(n,x)$	n	$D_2^*(n,x)$
3	0.373960	35	0.001349
5	0.231718	37	0.002539
7	0.133812	39	0.001078
11	0.086684	41	0.001492
13	0.055841	43	0.001062
15	0.025077	45	0.000038
17	0.029255	47	0.000746
19	0.019622	51	0.000321
21	0.008432	53	0.000454
23	0.010704	55	0.000146
29	0.007286	57	0.000169
31	0.005060	59	0.000248
33	0.002215		

3. CONCLUSIONS

Our computations show (see Fig. 1-17) that the densities of primes p for which the least primitive root modulo $2p$ is equal to a given positive integer n given by formula (2) tend very fast to some constants. Numerical values of these constants are collected in Table 2. It has to be pointed out that $g(2p) = 3$ for about 0.3739 of all primes (initial digits of Artin's constant). The average value expressed by (2) is approximately equal 7.456...

REFERENCES

1. K. Ireland, M. Rosen: *A Classical Introduction to modern Number Theory*, Springer-Verlag, New York, Heidelberg, Berlin, 1982, Graduate Texts in Mathematics, 87
2. A. Paszkiewicz, A. Schinzel: *On the least prime primitive root modulo a prime*, Math. Comp. v. 71, no. 239, pp. 1307–1321, 2002
3. A. Paszkiewicz: *On least primitive roots mod 2p for odd primes*, Electronics and Telecommunications Quarterly, 55, no. 1, pp. 57–69, 2009
4. A. Paszkiewicz: *A new prime p for which the lest primitive root (mod p) and the least primitive root (mod p2) are not equal*, Math. Comp., v.78, no. 266, pp. 1193–1195, Apr. 2009

ELECTRONICS AND TELECOMMUNICATIONS QUARTERLY, 2009, 55, no 4, pp. 659–668

Classification Criteria of Linearization Methods

PAWEŁ MYSZKOWSKI

Bialystok Technical University
Faculty of Electrical Engineering

Received 2009.10.19
Authorized 2009.11.16

The linearization of non-linear differential equations is a significant problem in analysis and synthesis of non-linear state equations. There are many methods of linearization, that leads to linear equation, which is an approximation of non-linear equation. Considering many different features of particular linearization methods a very important problem is how to choose a method to obtain the best results. In presented paper there are proposed criteria that make possible classifying of linearization methods. Considerations are illustrated by the example of non-linear model of electrical circuit.

Keywords: non-linear state equation, linearization, classification criteria, global linearization, optimal linearization

1. INTRODUCTION

The majority of physical phenomena, that take place in the nature, is described by non-linear mathematical models. There is applied for that reason the following equation, so called the state equation:

$$\dot{\mathbf{x}}(t) = f(\mathbf{x}(t), \mathbf{u}(t), t), \quad \mathbf{x}(0) = \mathbf{x}_0, \tag{1}$$

where $\mathbf{x}(t) \in R^n$ is a state vector, $\mathbf{u}(t) \in R^m$ is a input vector and $\mathbf{x}_0$ is a vector of initial conditions.

It could be said, that the non-linear character of these phenomena is an engine of all changes happening in the nature. Therefore the analysis of non-linear physical systems is very important in almost all branches of technology. Refering to problems from the electrotechnics, non-linearity appears both in description of elements or electrical systems and in transient states of electrical circuits. General rules of solving non-linear equations have not been elaborated so far. The analysis of the dynamics of non-linear

systems is a complicated problem from the mathematical point of view and ambiguous in many cases. Determining the stability area with the use of the Lyapunov function requires very complicated calculations [1,2]. In particular, it is difficult to obtain the solution for the large number of state variables. Numerical methods, which make possible to obtain an approximate solution in a discreet form, do not give general information about the uniqueness of the solution and stability area of the system.

Problems of the linearization of non-linear differential equations have been found in technical literature for many years [1-7]. Investigations into linearization involve equations both of common and partial derivatives. Theoretical basis of analysis and synthesis of linear equations were elaborated in XIX and XX century and they are perfectly known. In particular cases the linear approximation allows to describe a fundamental problems involved with the analysis of the non-linear system dynamics. Determining the stability area with the use of eigenvalues of the linear approximation matrix is a generally known problem and it is a first step in analysis of non-linear system stability. The next step is a stabilization of non-linear systems. Finally, the linearization enables the synthesis of non-linear system with the use of its linear approximation.

2. THE OVERVIEW OF LINEARIZATION METHODS

In technical literature many different linearization methods could be found. These methods make possible to obtain the linear approximation of non-linear state equation (1) [1-7]:

$$\dot{\mathbf{x}}(t) = \mathbf{A}\mathbf{x}(t) + \mathbf{B}\mathbf{v}(t), \quad \mathbf{x}(0) = \mathbf{x}_0, \tag{2}$$

where $\mathbf{v}(t)$ is a new excitation.

The most commonly known method is a linearization with the use of Taylor's series expansion around the equilibrium point [1], which does not require complicated transformations, however it determines a good approximation only for small deviations from the equilibrium point. Methods, that lead to the accurate linear approximation in the whole state space, are the optimal linearization [1,3,4,7] and the global linearization [5,6,7]. The first of these methods is based on the analysis of the mean-square error between right hand side of non-linear equation and its linear approximation. However this method is very expensive, particularly for higher number of state variables. The global linearization is based on the replacement of state variables, fulfilling conditions of the global diffeomorphism and introducing the non-linear feedback. There exist methods, like the method of optimal line [7] or the method of describing function [7], which do not refer directly to non-linear state equation, although they linearize non-linear characteristics of real elements, that occur in the system.

3. CLASSIFICATION CRITERIA OF LINEARIZATION METHODS

There are many methods of linearization and it is impossible to discuss them all. There have not been created neither their classification nor mechanisms allowing to choose for particular case a better method from compared set or pair so far. Methods differ from each other according to accuracy of obtained approximation, complexity and other features. This is the reason of introducing classification criteria, that allow to compare precisely linearization methods and describe their features with the use of numerical values.

In the paper there are presented four partial classification criteria for linearization methods and a global criterion, determined by partial criteria. The value of the norm defining the global criterion is a measure of a quality of the linearization method. It must be noted, that two of four partial criteria, and as a result – based on them the global criterion, are determined for the certain value of integration step-size.

3.1. ACCURACY OF LINEAR APPROXIMATION

The first and basic rating criterion of linearization method is an accuracy of linear approximation. It is expressed with the use of value of maximum difference ($\Delta_{i,\max}$) between the solution of non-linear model and the solution of its linear approximation or with the use of value of mean-square error in the defined time interval:

$$\Delta_{i,\max} = \max_{1 \le i \le N} \left| x_{i,NL} - x_{i,L} \right|. \tag{3}$$

The system obtained with the use of linearization is a system of linear differential equation. To solve this system it is used a Runge-Kutta method of 4^{th} order with constant integration step size [8]. The obtained solution is in the discreet form, in precisely defined points of time; it also refers to the non-linear equation. The approximation error (the accuracy of linear approximation) x^1 is defined on the base of analysis of maximum norm of difference between vectors of solution (linear and non-linear) and on the base of norm describing the mean-square error

$$x^1 = \frac{\sum_{i=1}^{N} \Delta_{i,\max} + \sqrt{\sum_{i=1}^{N} \Delta_{i,\max}^2}}{2}. \tag{4}$$

To standardize this criterion, the absolute value, calculated with the norm, is transformed into value from the range of [0, 1]. The relative value $x^1_{rel,i}$ refers to the accuracy for the biggest considered value of integration step-size $x^1_{\max}$. For this value the discrepancy between the solution of non-linear equation and its approximation is the most significant

$$x^1_{rel,i} = \frac{x^1_i}{x^1_{\max}}, \quad i \in [1, N]. \tag{5}$$

3.2. COST (COMPUTATION TIME)

The next criterion, characterizing the linearization method is the cost. It is a time necessary to perform computations with the use of linear model. The cost of computations is described by relative or absolute time of performing the algorithm at the same computer or at a computer with the same calculation efficiency. The absolute time x^2, expressed in seconds, could not be sufficient criterion considering different implementations of algorithms, different possibilities of resultant code optimizing or computations on different software platforms (Mathematica, Matlab, C language implementations, etc.). It is the main reason of introducing the relative measure x^2_{rel}, dependent from the calculation time for the smallest considered integration step-size $x^2_{\max}$

$$x^2_{rel,i} = \frac{x^2_i}{x^2_{\max}}. \tag{6}$$

3.3. COMPLEXITY OF LINEARIZATION PROCESS

The computational complexity is a term connected to computation theory [9]. The main aim of this term is defining the amount of resources needed to solve computational problems. Considered resources are such quantities as time, memory or number of processors. The complexity is being defined for the particular algorithm, describing the solution of particular problem. The complexity could be divided into time and memory. The measure of time complexity is a number of basic operations in dependence of entry size (i.e. size of matrix, number of state variables). The measurement of real time clock is not very useful for the sake of strong dependence from the way of algorithm realization, used compiler and hardware, which the algorithm is performed on. Therefore as the computation time the number of basic (dominant) operations is usually considered. Basic operations are for example: a substitution, a comparison or a simple arithmetical operation. The memory complexity is a measure of amount of used memory. The most often, it is the memory used by the abstract machine (i.e. number of cells of RAM) as a function of entry size. It is also possible to calculate the size of needed physical memory measured in bits or bytes. In general case the computational complexity characterizing the quality of code written by the programmer and generated by the compiler, the speed of the hardware, which the program is executed on, the size of entry data and the used algorithm.

However the computational complexity is not the idea of this classification criterion. Every method of linearization requires a certain amount of work, which should

be done in order to obtain a linear approximation. Therefore the numerical measure, describing the level of the method complexity, is introduced. This measure depends on:

- the number of transformations for the same number of state variables,
- the complexity of these transformations (i.e. calculation of partial derivatives or identity transformations are simpler than calculation of values of definite integrals, usually in numerical way).

The complexity of linearization process x^3 is defined with the use of value from the interval $(0, 1]$, chosen in heuristic way. It follows from the assumed method of linearization of non-linear model with the factor dependent on the accuracy of linear approximation and the calculation cost. The smaller value this criterion obtain, the less complex is the linearization process for considered method.

3.4. ABILITY TO INVESTIGATE DYNAMICS, STABILIZATION AND SYNTHESIS

The last partial criterion shows the rank of the linear approximation, obtained with the use of the particular method, to use it to investigate of system dynamics, stabilization of non-linear system and changing its dynamics (synthesis). The ability to stabilization and synthesis is defined with the use of value from the interval $(0, 1]$, chosen in heuristic way. It follows from the implementation of known numerical algorithms, designed for the analysis of linear systems. The smaller value this criterion obtain, the bigger is ability of considered method to stabilization and synthesis.

3.5. GLOBAL CLASSIFICATION CRITERION

The global criterion G determines the numerical value describing particular method of linearization. The measure of usability of the method is a norm of the vector, whose elements are values determined with the use of partial criteria:

$$\mathbf{X} = \left\{x^1, x^2, x^3, x^4\right\}^T. \tag{7}$$

The global calculation criterion G is defined with the use of the maximum norm $G_{\max}$ and the Euclides norm G_{euk}

$$G_{\max} = \|\mathbf{X}\|_{\max} = \max_i \left|x^i\right|, \tag{8}$$

$$G_{euk} = \|\mathbf{X}\|_{euk} = \sqrt{\sum_{i=1}^{4} (x^i)^2}, \tag{9}$$

$$G = \frac{G_{\max} + G_{euk}}{2}. \tag{10}$$

4. NUMERICAL EXAMPLE

To illustrate above considerations a model of electrical circuit with non-linear resistance R_1, presented in Fig.1 [10] will be used. State variables in this system are the current i in the branch of inductor and potential drops on both capacitors – u_1 and u_2.

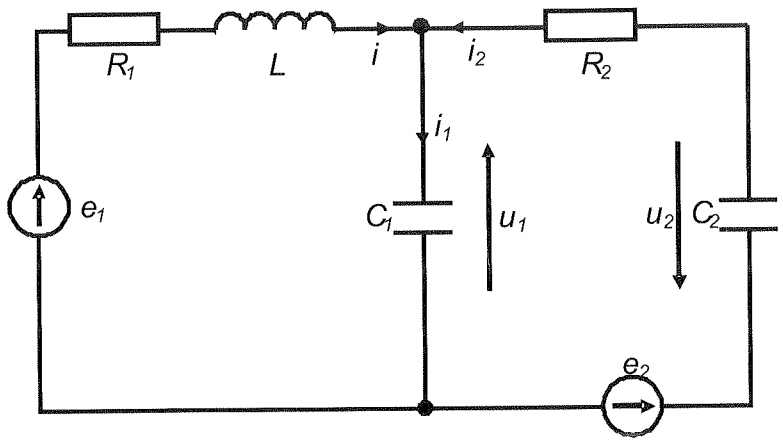

Fig. 1. A diagram of the electrical circuit with non-linear resistance R_1

The system is described with the following non-linear state equation:

$$\begin{aligned} \dot{x}_1 &= -a_1 x_1 - a_2 x_1^3 - a_3 x_2 + a_3 e_1 \\ \dot{x}_2 &= a_4 x_1 - a_5 x_2 + a_5 x_3 + a_5 e_2 \\ \dot{x}_3 &= -a_6 x_2 - a_6 x_3 + a_6 e_2 \\ x_1(0) &= 0, \quad x_2(0) = 10, \quad x_3(0) = 10 \end{aligned} \tag{11}$$

Coefficients a_1, a_2, a_3, a_4, a_5, a_6 depend on values of physical parameters of the circuit, like R, L, C. Courses of state variables for rated values of parameters are presented in Fig. 2.

Equation (11) is being linearized with the use of two methods: the optimal linearization and the global linearization.

As a result of applying the optimal linearization, the following homogeneous linear equation in the form of $\dot{\mathbf{x}}(t) = \mathbf{A}\mathbf{x}(t)$ is obtained:

$$\begin{bmatrix} \dot{x}_1 \\ \dot{x}_2 \\ \dot{x}_3 \end{bmatrix} = \begin{bmatrix} -55606.9 & -1000.16 & -0.207181 \\ 10^{-6} & -10000 & 10000 \\ -1.028 \cdot 10^{-7} & -10^{-7} & -10^{-7} \end{bmatrix} \begin{bmatrix} x_1 \\ x_2 \\ x_3 \end{bmatrix}, \tag{12}$$

$$x_1(0) = 0, \quad x_2(0) = 10, \quad x_3(0) = 10$$

The global linearization of non-linear model of above electrical circuit was presented in work [11]. Applying of general variant of global linearization method supplied the following linear approximation:

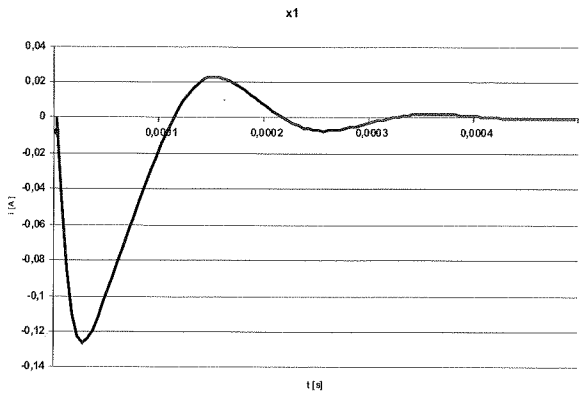

Fig. 2a. The graph of first state variable – x_1 – for rated values of parameters

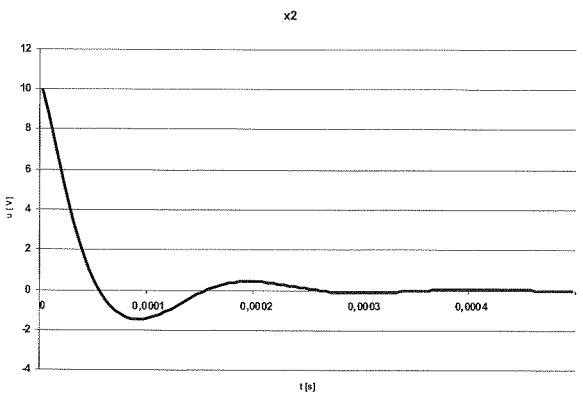

Fig. 2b. The graph of first state variable – x_2 – for rated values of parameters

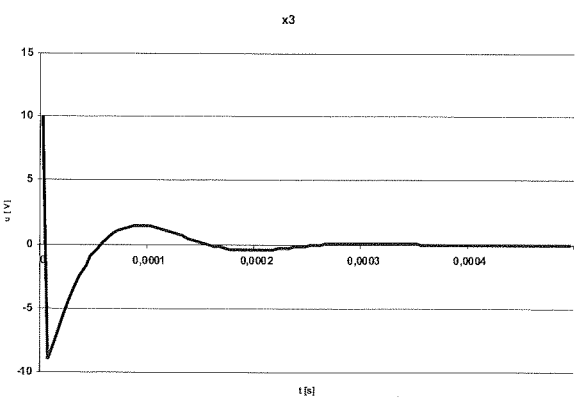

Fig. 2c. The graph of first state variable – x_3 – for rated values of parameters

$$\begin{bmatrix} \dot{z}_1 \\ \dot{z}_2 \\ \dot{z}_3 \end{bmatrix} = \begin{bmatrix} 0 & 1 & 0 \\ 0 & 0 & 1 \\ -a_3 & -a_2 & -a_1 \end{bmatrix} \begin{bmatrix} z_1 \\ z_2 \\ z_3 \end{bmatrix} + \begin{bmatrix} 1 & 0 & 0 \\ 0 & 1 & 0 \\ 0 & 0 & 1 \end{bmatrix} \begin{bmatrix} g_1(x,u) \\ \bar{g}_2(x,u) \\ \bar{g}_3(x,u) \end{bmatrix}, \qquad (13)$$

$$z_1(0) = 0, \quad x_2(0) = 10, \quad x_3(0) = -99990$$

where functions g_1, $\bar{g}_2$, $\bar{g}_3$ are new excitations [11].

State equations (12) and (13) were numerically solved with the use of Runge-Kutta method of 4^{th} order with the constant integration step-size and were compared with the solution of non-linear equation (11). Results for the first state variables and for different values of integration step-size are presented in Fig. 3.

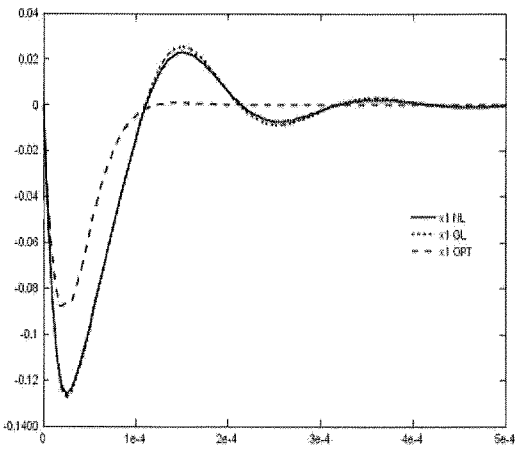

Fig. 3a. The graph of first state variable – x_1 – for both methods and integration step-size $h = 10^{-7}\ s$

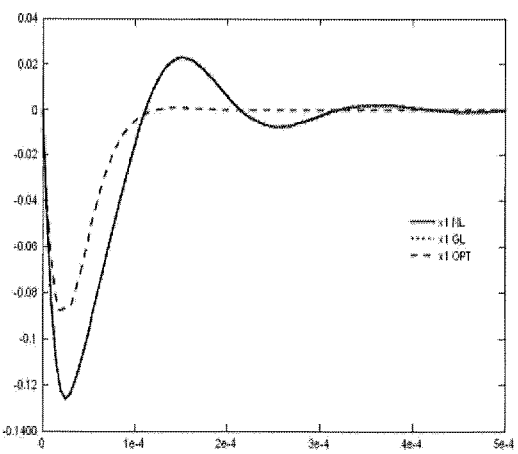

Fig.3b. The graph of first state variable – x_1 – for both methods and integration step-size $h = 10^{-11}\ s$

Values of partial criteria and as a result the value of global criterion for both linearization method were determined. Results are presented in Table 1.

Table 1

COMPARISON OF LINEARIZATION METHODS ON THE BASE OF DEFINED CRITERIA

Integration step-size	Accuracy x^1		Cost x^2		Complexity x^3		Usability x^4		Global criterion	
	GL	OPT	GL	OPT	GL	OPT	GL	OPT	GL	OPT
$h = 10^{-7}\,s$	1.732	1.732	0.0007	0.0012	0.2	0.1	0.1	0.5	**1.7464**	**1.8055**
$h = 10^{-8}\,s$	0.3035	1.732	0.0011	0.0027	0.2	0.1	0.1	0.5	**0.377**	**1.8055**
$h = 10^{-9}\,s$	0.1387	1.732	0.0109	0.0111	0.2	0.1	0.1	0.5	**0.2633**	**1.8055**
$h = 10^{-10}\,s$	0.1269	1.732	0.0951	0.1017	0.2	0.1	0.1	0.5	**0.2741**	**1.8054**
$h = 10^{-11}\,s$	0.1257	1.732	1	1	0.2	0.1	0.1	0.5	**1.0323**	**2.0639**

It must be noted, that values of partial criteria describing the complexity of linearization process and usability of the method for stabilization and synthesis were determined *a priori* on the base of results of previous works.

The comparison of global criterion for both methods, presented in Fig. 4, allows to point out in unique way, which method is better for considered example and what range of integration step-size allows to obtain optimal results. For better illustration of the character of changes, discrete values of the global criterion were approximated with the polynomial of 2^{nd} degree.

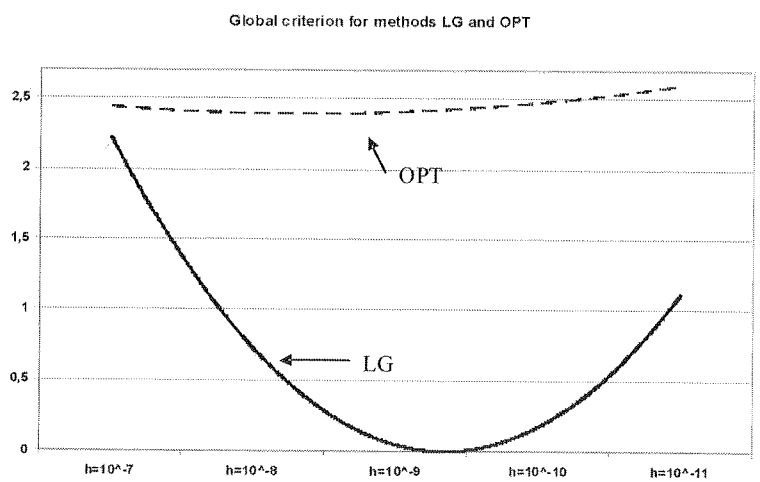

Fig. 4. Comparison of linearization methods on the base of global criterion

5. CONCLUSIONS AND FUTURE WORK

From the comparison of both methods results, that for all considered values of integration step-size the global linearization method gives better results than the optimal linearization. The range of changes of integration step-size is conditioned by remarks, that for $h > 10^{-7}\,s$ the solution obtained by the global linearization method is divergent and for $h < 10^{-11}\,s$ the cost of computations grows in linear way, do not give the supposed increasing of accuracy at the same time. During future works it must be considered a more precise way of determining values of partial criteria connected with the complexity of linearization process and the ability to stabilize and synthesis.

ACKNOWLEDGEMENTS

Author would like to thank prof. Andrzej Jordan, who has taken the time to help with suggestions for improvements in the idea of this paper. This work has been carried out within the dean's project no S/WE/3/08.

6. REFERENCES

1. T. Kaczorek, A. Dzieliński, W. Dąbrowski, R. Łopatka: *The basis of control theory*, WNT, Warszawa, 2004 (In Polish)
2. T. Kaczorek: *System and control theory,* PWN, Warszawa, 1999 (In Polish)
3. A. Jordan (et al): *Optimal Linearization of Non-Linear State Equations*, Rairo-Automatique, System Analysis and Control, Vol. 21, No 2, pp. 263–271, 1987
4. A. Jordan (et al): *Optimal linearization method applied to the resolution on non linear state equations*, Rairo-Automatique, System Analysis and Control, Vol. 21, No 2, pp. 175–185, 1987
5. A. Isidori: *Nonlinear control systems,* Springer Verlag, 1995
6. R. Marino, P. Tomei: *Nonlinear Control Design – geometric, adaptive, robust,* Prentice Hall, 1995
7. A. Jordan, T. Kaczorek, P. Myszkowski: *Linearization of non-linear differential equations,* Publishing of Białystok Technical University, Białystok, 2007 (In Polish)
8. A. Krupowicz: *Numerical methods of initial conditions of ordinary differential equations,* PWN, Warszawa, 1986 (In Polish)
9. Ch. H. Papadimitriou: *Computational complexity,* WNT, Warszawa, 2002 (In Polish)
10. T. Kaczorek: *Applying of polynomial and rational matrices in dynamical systems theory,* Publishing of Bialystok Technical University, Białystok, 2004 (In Polish)
11. P. Myszkowski: *Selected aspects of the global linearization of non-linear state equation,* Proceedings of SPIE vol. 6937, Wilga, Poland, 2007

ELECTRONICS AND TELECOMMUNICATIONS QUARTERLY, 2009, 55, no 3, pp. 669–682

Free Electron Laser in Poland

RYSZARD S. ROMANIUK

Institute of Electronic Systems, Warsaw University of Technology
e-mail: R.Romaniuk@ise.pw.edu.pl

Received 2009.09.05
Authorized 2009.11.09

The idea of building a new IVth generation of light sources of high luminosity, which use accelerators, arose in the 80ties of XXth century. Now, in a numerable synchrotron and laser laboratories in Europe, an intense applied research on free electron lasers has been carried out for a couple of years (FEL) [17,18]. Similarly, in this country, free electron laser in Poland – POLFEL [9] is in a design, a coherent light source of the IVth generation, characterized by very short pulses in the range of 10-100fs, of big power 0,2GW and UV wavelength of 27nm, of average power 1W, with effective high power third harmonic of 9nm. The laser consists of a linear superconducting accelerator 100m in length, undulator and experimental lines. It generates a monochromatic and coherent radiation and can be tuned from THz range via IR, visible to UV, and potentially to X-rays. The linac works in quasi-CW or real-CW mode. It is planned by IPJ [9,10] and XFEL-Poland Consortium [16] as a part of the ESFRI [1] priority EuroFEL infrastructure collaboration network [6], part of the European Research Area - ERA [2]. The paper discusses: FEL background in Poland as a part of EuroFEL infrastructure, FEL parameters and performance, FEL research and technical program and FEL networking in Europe and worldwide. Emphasis is put on the usage of superconducting RF TESLA technology and ties linking Polfel and the European X-Ray Free Electron Laser. The Polfel team of researchers is now dissipated worldwide among such projects as Flash and E-xfel in Desy, Cebaf in JLab, Alba in Barcelona, Elettra in Trieste, ILC in Fermilb, LCLS in SLAC. Polfel creates an unique, but quite transient chance to gather and solidly accumulate for a long time this expertise in this country again.

Keywords: photonics, THz, UV, IR, X-ray, photon beam, electron beam, FEL, free electron laser, XFEL, synchrotron, undulator, RF gun, Nb, high field magnets, super-conductivity, accelerator, linac, luminosity, brilliance (brightness), SASE, HGHG, SEED, e-bunch

1. FEL BACKGROUND IN POLAND AS A PART OF EUROFEL INFRASTRUCTURE

Recent developments of technology enabled a number of new fields of basic and applied research. One can mention such areas as: work on fundamental laws of physics, new materials engineering, more efficient semiconductors, quantum optics and chemistry, structural biology, biomedicine with targeted imaging, photo and radiotherapy, new medicines. Research methods in distant fields have common features. The research needs enormous sets of data and immense processing power for simulations and analysis. The researched objects vary from nano, via pico to femtometers. The objects are cells, molecules, micella, atoms, nuclei, elementary particles. Time spans of concern, for the observed dynamic processes like chemical reactions, are also femto and attoseconds. These advanced research methods require large infrastructures including accelerators of high energy particles, synchrotrons, free electron lasers, as well as, classical ones, but of high power and/or high intensity.

Poland has never had and till now has not got even one of such infrastructure. This is a serious obstacle in carrying out own advanced research in a number of the above mentioned fields. The national budget for research was far to small even to dream of such undertakings.

Now, the chance for this country to build its first big research infrastructures, including a synchrotron and FEL centres, has been recently multiplied. There are relevant funds available for building of the common European Research Area (ERA) basing on strong research infrastructures available equally to all participants. There are in this country appropriate research and technical institutions to undertake the effort to design, build, commission, maintain and exploit these infrastructures. There are ready designs of useful infrastructural projects. There is a considerable public demand for this country to enter into an exclusive club of owners of large research infrastructures, commonly exploited with other European Community countries inside ERA. There is a very positive political atmosphere around such undertakings in Poland and Europe. There is also a very positive obligation in this country to consume effectively the European funds designed just for these purposes of research infrastructures. The obtained European structural funds for 2007-13 include 1.3bln € for research infrastructures. These resources are enough to build a few big experiments in Poland fit to the physical and energy scale dimensions, geographical extent, scientific program, research and technical ambitions of the European Research Area scale and expectations.

The Polish research community of photonics, synchrotron radiation, FELs, attosecond and HP-HI lasers, organized in a number of associations like Photonics Society of Poland, Polish Committee of Optoelectronics – Association of Polish Electrical Engineers, Section of Optoelectronics – Polish Academy of Sciences, Polish Association of Synchrotron Radiation; as well as consortia – among them XFEL-Poland, Polish Platform of Nuclear Technologies and Femtophysics, participate actively in many European research networks, collaborations and projects like: ELI, HIPER, LaserLab, TESLA

FLASH, ILC, E-XFEL, EuroFEL. Access to the knowledge and experience of the whole European synchrotron and laser communities is available. This is a solid gate and background to building our own complementary laser infrastructures, using the newest, yet checked, technologies and avoiding too expensive, and out of reach, development phase of the project like building prototypes for early system commissioning.

The design documents of POLFEL were prepared in this way as to take advantage of these chances – political, financial, scientific, technical and ambitional – and settle, for the first time in history, a research project of the European size in Poland.

2. FEL COMPONENTS AND TECHNICAL DATA

A free electron laser is different in the principle of work and, thus, construction and exploitation from classical ones. It does not have an optical resonator confined at both sides by spectral mirrors, which provide the feedback and amplification to the generated photon beam. FEL is a laser with a single generation, buildup and passage of the beam along the machine, working without mirrors. It is tunable in a very wide spectrum of EM waves. It generates a photon beam, at such wavelengths, where conventional lasers do not, because of the lack of efficient technical solutions of appropriate mirrors. The basic equation of FEL is the following:

$$\lambda_{ph} = \lambda_u(1 + K^2)/2\gamma^2, \tag{1}$$

where λ_{ph} – wavelength of the first harmonic, spontaneous, on-axis FEL undulator photon emission beam, λ_u – undulator period, K – undulator parameter proportional to the periodic magnetic field, $\gamma=(1-\beta^2)^{-1/2}$ – classical electron relativistic factor. The FEL relation shows explicitly an extreme elasticity of the laser to all methods of tuning against the generated wavelength λ.

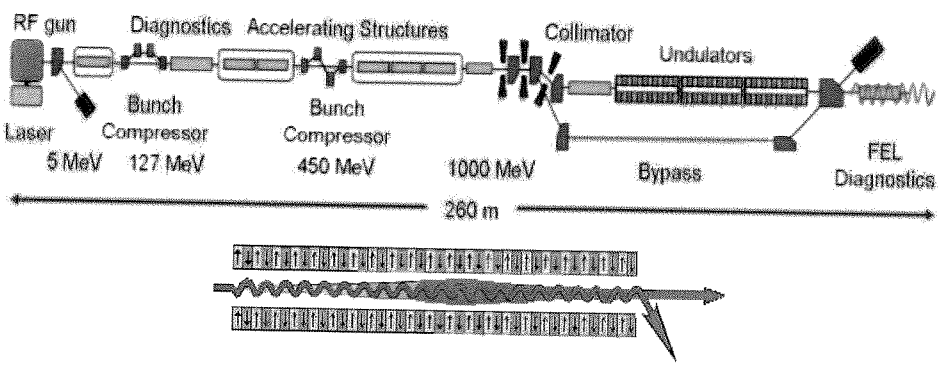

Fig. 1. Schematic diagram of FEL on the example of FLASH in DESY [7]

FEL consists of an electron injector, linear accelerator – a linac, undulator, electron beam dump (or energy recovery from the used e^- beam) and photon lines. Future FELs

will use superconducting (SC) injectors with Nb cavity. Conventional RF gun consists of a warm Cu cavity with a photocathode of Cs_2Te. The photocathode is excited with a UV pulse of λ = 266 nm, which is the 4th harmonic from a Nd:YAG laser. A superconducting RF gun has a photocathode covered with Pb, because Pb has lower exit energy for electrons at cryo-temperatures.

A single laser pulse, together with a presence of HV at a cathode, causes emission of an electron cloud of average charge $Q_e \approx 1$ nC. The pulse repetition rate is confined to f_{gun} = 1 kHz by thermal stability of the RF gun, caused by heat release in Cu. The Cu cavity and the following chain of Nb cavities is powered by a HP klystron or a klistrode (inductive output tube - IOT) of P_{RF}=10MW. The FEL processes require that the electron bunches have low normalized (transverse) emittance smaller than $\varepsilon_n < 2\mu$ rad and the charge in the range $Q_e \approx 0{,}2 \div 1$ nC. These are parameters for the RF electron gun, because the emittance during the acceleration process may only be increased. The predicted RF gun for Polfel would work in CW mode, possess alkali cathode or superconductive and would work in photoemission mode.

The electron cloud from the RF gun has to be magnetically compressed, spatially and energetically, after some pre-acceleration, to a coherent e^- bunch. The injector of e^- energy $E_{ini} \approx 120$ MeV, which consists of RF gun and pre-accelerator, gives electron bunches of $L_b \approx 1$ mm in length. The demands for the compact electron bunch of high quality stem from the requirements on the resulting photon pulse from the laser, and are as follows: high pulse current $I_e \approx 1 \div 10$ kA; average beam current I_b = 1 mA; high beam power $P_b \approx 350$ kW; beam power density $dP_b/ds \approx 3{,}5 \cdot 10^{11}$ W/cm^2, bunch separation $t_{sb} \approx 1\mu$s; short spatial, including longitudinal $L_b < 100\mu$m and transverse D_b=10μm, as well as temporal T_b < 1 ps dimensions; correlation of position-energy of electrons in the bunch (clear monotonic dispersion character of the bunch). The compressor of the beam consists of a magnetic chicane (4 H type dipole electromagnets of strong $B_H \approx 0{,}5$ T and homogeneous s_H = 300 mm field causing U bend of the e^- path), correction coils for each magnet, and three beam refocusing quadrupoles. The resulting e^- bunches from the first compressor, positioned after the injector, are very dense, short, coherent energetically $\Delta E < E_{coh}$, and of small transverse emittance $\varepsilon < 1\mu$rad. The second compressor (and beam corrector) is placed just before the undulator and the H field parameters of chicane dipoles are optimized for the incoming bunch energy $E_b \approx 0.5 \div 1$ GeV. The input energy of the undulator depends on the active length of the linac, i.e. the number of cryo-modules.

The linac uses a well established, and used widely around the globe, superconducting niobium TESLA cavities, organized in 9 cell structures (resonators) of $L_c \approx 1$ m (active length) and $L_{cc} \approx 1{,}2$ m (total length with collars and flanges for couplers, HOM suppressors and field probes), with 8 ones in a single cryo-module (cold mass). The purity of Nb is RRR > 300. Resonant frequency of the cavity is $f_c \approx 1.3$ GHz (L-band). Each of 9 cell resonators is supplied by RF power $P_{RF} \approx 100 \div 300$ kW via rectangular waveguides filled with SF_6. Field intensity in the cell is $E_{RF} \approx 20 \div 35$ MV/m. The fundamental mode is TM010. The unloaded/loaded Q of the structure is respectively

$Q_{ul} = 10^{10}$, $Q_{ld} > 10^7$. The work temperature of the structure is T_c=1,8K obtained in three levels, via 40÷80 K, and 5÷8 K shields to the state of super-fluid helium. The radiative shield is at 4.5 K. The cryogenic load of the structure is $P_{crl} \approx 3$ W.

Each cryo-module contains: 8 TESLA structures; 8 HP RF waveguide/coaxial line cryogenic fundamental mode couplers – FMC; 8 two-function, slow-fast, mechanical tuners of the cavity; 16 high order mode couplers – HOMC; HOM absorber; ion vacuum pump; correcting magnet and quadrupole lens; beam position monitor – BPM; helium vessel; cold mass package for reference positioning of components and thermal insulation; cryogenic cabling for measurements, diagnostics and control.

A natural resonant frequency of the i-th resonator is $f_{ci} \approx 1.3$ GHz and is statistically distributed around the average cavity frequency f_{ca} by a few hundred kHz. The average f_{ca} frequency should be as close to the required accelerating frequency f_{acc} as possible. Precise tuning of a cavity from the f_{ci} to the f_{acc} value is done by means of a static mechanical method. A set of pulling-squeezing vices is integrated with each structure. The tuning is static and off-line.

The resonator is subject to Lorentz force detuning (LFD) and microphonics (MP). LFD is a reaction of the Nb SC resonator, of the average wall thickness $d_w \approx 2.5 \div 3$ mm, thus, not very stiff, to filling with HP EM RF field. The resonators are stiffened with stiffening rings and collars and sealed titanium chambers for super-fluid He. The LFD, via the change in cavity dimensions L_c and D_c, results in the change in the resonant frequency f_c. Typical value of the frequency dynamic detuning Δf_{LFD} is equal to the cavity 3dB bandwidth $\Delta f_c \approx 200 \div 300$ Hz.

Each resonator is filled with accelerating field, via a power coupler, and then works in a pulse or CW mode. The coupler consists of: waveguide to coax transition; two vacuum – microwave windows, one ambient temperature $T_{w1} = T_a$, the second cold $T_{w2} = 70$ K; thermal insulation components from T_a to $T_c = 1.8$ K; Nb coaxial head ended with antenna of controlled coupling to the HP field of the FM in the accelerating structure.

Beam loading and acceleration at a cost of the accumulated field energy in the structure causes perturbation and excites longitudinal and/or transverse higher order modes (HOM) to propagate. The HOM have higher frequencies than the fundamental mode (FM), thus, can be filtered out by a low pass filter. The HOM distort e^- bunches via a disturbance to the FM field distribution. A HOM filter is an antenna situated on both ends of the structure and strongly coupled to higher frequencies (not coupled to FM).

Each structure is equipped in a two-level, slow and fast, mechanical tuner, with a piezoelectric converter (voltage-shift V-ΔL_c). The resonance f_{ci} of each i-th structure is individually fit to the accelerating frequency f_a by squeezing or stretching the cavity of ΔL_{cs}. Slow tuning, with reaction time $t_{st} = 1$ min, for static pre-detuning purpose, is done mechanically in a vice within typical margins $\Delta L_{cs} \approx \pm 1$ mm for $L_c \approx 1$ m, what corresponds to $\Delta f_{cs} \approx \pm 300$ kHz. This value is comparable to the difference $|f_a - f_{ci}|$. Fast tuning, for Lorentz force detuning, and microphonics compensation, as well

as dynamic pre-detuning, is done dynamically, during cavity filling, with the reaction time $t_{dLFD} \approx 1$ms and frequency tuning range $\Delta f_{cd} \approx \pm$ 0.5 kHz. The value of Δf_{cd} is comparable to Δf_c which guarantees a precise tuning tracking of the cavities.

HP RF supply system provides microwave power of $f_{acc} \approx$ 1.3 GHz to fill the accelerating cavities with the EM filled and then maintain the field intensity in the range of $E_{acc} \approx 25 \div 35$ MV/m. The HP RF system works in a pulse and CW modes and consists of: power amplifiers, modulators, inductive output tubes (IOT), HV HP supply units, control amplifiers, protection and safety circuits, power distribution via transmission waveguides with Y and T couplers, isolators and circulators from IOT to cavities, and auxiliary components.

The accelerator control system (ACS) consists of: low level RF (LLRF), including reference time distribution from the master oscillator, measurement, synchronization and fast control via FF/FB modes; slow control (SCt); e^- beam diagnostics, interlock and experiment diagnostics; and diagnostics of the whole machine and the experiment.

The LLRF system stabilizes the field in accelerating cavities, generates the accelerator clock and synchronizes all equipment with this clock. The SCt controls all FEL infrastructure including: vacuum, cryogenics, gases, HVs, power supplies, ambient parameters. The diagnostics localizes potential causes of system misbehaviour, failures and all unexpected departures from standardized procedures, defined by state machines (SM). Diagnostics has to be independent of other systems and highly reliable, similarly to interlocks. The interlock system traces many threshold values in FEL and reacts accordingly when the threshold is crossed, including full stop of the machine when the work parameter values are critical. All these subsystems are managed by SCADA – industrial supervisory control and data acquisition.

The LLRF system of fast control stabilizes the HP RF field using direct, predictive or adaptive feed forward (FF), feedback (FB) or a mixed method FF+FB. The FF compensates deterministic, systematic errors while FB nondeterministic ones (noise). The changes in the accelerating field amplitude and phase, as an error signal, are fed back in the loop to the modulator of the klystron (or IOT) causing relevant changes in the HP generator output. The requirements on the HP RF field stability are: 10^{-4} in amplitude and 10^{-1} in phase in degrees. The RF field in the cavity is probed by an antenna, down-converted from f_{acc} to f_{IF} (intermediate level), sampled by ADC, digitally processed for error, converted to analog in DAC and input to vector modulator, for control of the klystron.

Cryogenics for a single cold mass requires $P_{1cold} = 50$ W of cold power at $T_c = 2$ K. Accumulated output cold power from the cold plant for injector, six cold masses and helium transport lines in POLFEL is estimated for $P_{cold} \approx 500$ W. Superfluid helium II is extremely penetrable and has nearly ideal heat conduction. This requires maintaining low pressure in the He installation piping in cryo-modules $P_{HeCM} = 30$ mbar. The cold plant produces He in different thermodynamic states and in the following temperatures, required by successive thermal shields in the cold-mass: $T_{1TS} \approx 40 \div 80$ K, $T_{2TS} \approx 5 \div 8$ K, $T_c = 1.9$ K. The radiation shields work at $T_{RS} = 4.5$ K. The cold plant consists

of: warm He compressors, heat exchangers, turbine decompressors and Jule-Thomson choking walves. Cold compressors in the He return lines avoid flows of large gas volumes at ambient temperature.

The high quality UHV vacuum line, made of 316 LN steel, oil-less, dustless, at $p = 10^{-8}$ mbar, embraces RF gun, e^- beam path and photon paths. Part of the vacuum lines are cold T_c=2K in the cavities, and part ore warm $T_a = 20^oC$ in electron optics, undulators and photon diagnostics. The initial out-pumping is done by turbomolecular pumps and then the vacuum is maintained by geter-ion and sorption pumps.

Undulators, which are in series, periodic, linear stack of magnetic dipoles of opposite field direction, are tailored to the e^- energy. There are used in FEL planar hybrid undulator sections with steady NdFeB magnets. The undulator parameters are: slit $s_{und} = 5 \div 15$ mm, period $p_{und} = 5 \div 30$ mm, length $l_{und} = 2 \div 10$ m, magnetic induction $B_{und} = 0.5$ T. The e^- beam is monitored and focused inside the undulator, between sections, by quadrupole magnets. The undulator is protected against the stray synchrotron radiation generated inside.

There are two main mechanisms to generate THz-IR-V-UV-X coherent photon beam by the e^- beam in the undulator: SASE – self amplified spontaneous emission or HGHG – high gain harmonic generation and enhanced by SEED – seeding with a laser beam. SASE means that there is a self-modulating interaction between a train of highly relativistic e^- bunches and photons generated by the bunches. The bunches are self-sliced to flat micro-bunches of high density of local charge, and the process is a function of the undulator length. A sliced bunch generates photons coherently and intensely as a point source.

The e^- beam goes to an energy recovery circuit, instead to a dump, in a future FEL.

The distributed diagnostics of the whole length of the e^- beam consists of: toroids, beam position monitor BPM, optical transition radiation OTR, beam lost monitor BLM, beam inhibit system BIS, transversal deflecting structure TDS, laser heater for regeneration of the photocathode, collimators and quadrupoles.

The photon beam diagnostics measures (and reacts with a control feedback): pulse energy; beam intensity; wave spectra; direction, divergence and beam waist, transverse dimensions of photon beam; pulse duration; distribution of the wave front; polarization. Photon beam parameters are essential for the experiments.

The basic parameter to compare different FEL is their brilliance (brightness). For partially coherent light sources (wigglers and undulators) the brilliance BR, expressed in [photons(sec · mrad^2· mm^2· 0.1% BW)], may be calculated from the spectral flux SF, expressed in [photons/(sec · 0.1% BW)], divided by the photon beam rms radius r and divergence d obtained from convolution of the electron beam and photon diffraction parameters:

$$BR = SF/(2\pi rd)^2. \tag{2}$$

In the case of full transverse coherence the following relation is fulfilled rd = $\lambda_{ph}/4\pi$, thus:

$$BR = SF/(\lambda_{ph}/2)^2. \quad (3)$$

The brilliance is a spectral flux divided by the transverse photon phase space. Fig.2a presents the peak brilliance BR of different FEL families, working now and planned for the nearest decade, as a function of the generated photon energy E_{ph}[eV]. An analogous diagram of average brilliance $BR_{av}(E_{ph})$ for the same laser families has the same shape but the BR level is lower of 6÷8 orders of magnitude, depending on the photon energy, and changes in the range of $BR_{av} \approx 10^{24} \div 10^{27}$. These values BR_{max} and BR_{av} for FEL are higher than for the III^{rd} generation synchrotron light sources, respectively of 8÷10 and 4÷5 orders of magnitude. The peak brilliance is scaled to the length of a single pulse, while average brilliance is normalized to seconds at the highest possible repetition rate.

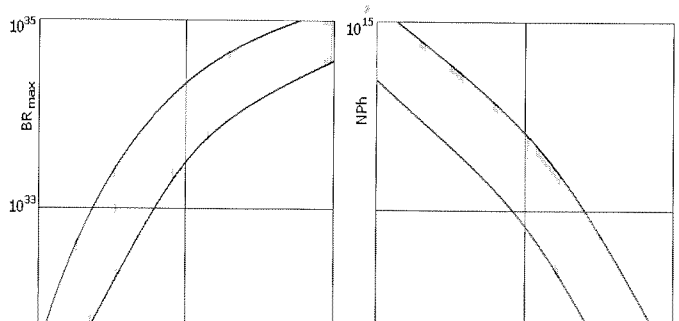

Fig. 2. Functions $BR_{max}(E)$, $BR_{av}(E)$, NPh(E) for FEL families. a) A schematic area of peak brilliance (brightness) BR of pulse FEL lasers, working now and planned during the coming decade, including superconductive FEL of TESLA type [5, 7, 8] and warm ones of LCLS type [12]; function BR_{av} has the same shape but different level; b) Number of photons (per mode) for SASE FEL families. Peak brilliance scaled to a bandwidth $\Delta\lambda/\lambda = 1$. Data: BW-bandwidth, NPh-number of photons, BR [NPh/s· mrad^2· mm^2· 0.1% BW], E[eV] = E_{ph} – photon energy

The number of photons generated by FEL per mode can be expressed as:

$$NPh = BR_{max}(\lambda_{ph}^3/4c) \quad (4)$$

where c-speed of light in vacuum. Fig.2b presents a function $NPh(E_{ph})$ for the same families of FEL as in Fig.2a.

The FEL is housed in a radiation shielded tunnel with a very stable, one piece floor along the whole length of the electron and photon beams. The quality of the external housing and support for the accelerator and photon lines are interferometer grade. The rest of the housing is technical, for auxiliary equipment, and laboratory for accommodating all experiments. The total power requirements for a FEL of the POLFEL size

are $P_{tel} \approx 3$ MW. The approximate price range for a machine of POLFEL size is 50÷100 M€ , depending on the assumed laser parameters and extent of infrastructure.

3. THE SCOPE OF BASIC AND APPLIED RESEARCH PROGRAM FOR FEL

FEL machines have a multiple role. They are strong drivers for technologies for their own development. They require new strong field magnet solutions, new effective undulators for high energy photons, new more compact architectures. On the other hand, a FEL laser enables new research, technologies and applications, among them in the following external – areas:

- research, ultra high field science, attosecond laser science, high energy beam facility, photon physics, two-photon absorption, pump-probe and photo thermal beam deflection PTBD spectroscopy, band edge spectroscopy,
- material processing and engineering, laser ablation and deposition, welding, adiabatic nano-melting, material structure modification, nanostructures formation, new semiconductors and glasses, meta-materials, formation of nano-morphous and nano--amorphous structures in materials, formation of corrosion resistant layers, lithography, organic crystals,
- biomedical and environmental, THz generation for imaging in the range of photon energy 10^{-2} eV, lens-less diffractive imaging, photon bio-probes, molecules imaging and spectroscopy, scalpels, lidars,
- chemical, fs scale time-resolved (TR) observations of chemical reactions, TR spectroscopy and holography, energy levels in strongly charged ions, probing of deep coulomb fields of atom nuclei (10^9 GV/m), energy probing of molecules.

Together with the increase in available photon energy (now this energy is close to 1keV in FLASH laser, and around 10keV in LCLS laser), FEL turns to a more and more effective tool of experimental research of highly charged ions. The deep level Coulomb field in a strongly charged ion is of the order of 1EV/m. Laboratory observations of deep transitions are performed to verify the quantum electrodynamics theory. Interaction of highly charged ions with strong EM field decides of the state of dense plasma. This phenomena is a subject of investigation in astrophysics (till now indirectly, only by means of telescopes) and thermonuclear fusion (in tokamacs) in order to generate energy. The FLASH research project included investigations of a cloud of trapped Fe^{+23} ions, and absorption spectra of strongly ionized Co [20].

FEL is a tool to investigate material ablation processes in different conditions than those available for classical lasers. These conditions allow to omit partly the nonlinear effects caused by non-equilibrium, abrupt surface phase changes in the material, high temperature and pressure, long wavelength interaction with the material, multiple phonon absorption and absorption on free carriers. The wavelength of FEL, to enable deeper penetration, may be tuned individually to a particular material, in the spectrum between the frequency edge of own plasma resonance and the absorption edge of deep

electrons excitation. FLASH laser was used for ablation experiments with Si and GaAs. There were measured penetration depths as function of wavelength and nonlinear effects [20]. The used experimental method was pump-probe with differential time resolved measurement of 100 fs resolution. The VUV pump signal was from FEL, while the delayed probe beam was from classical optical lasers, working in IR and visible.

The method of femtosecond spectroscopy with optical pump and probes, from FEL and optical laser, is used for investigations of interactions of optical beam of changing wavelength and high intensity with matter. Photoelectrons excited by a FEL pulse emit or absorb photons of the probing optical laser. The spectrum of photoelectrons consists of two symmetric lines at both sides of the main line. The intensity depends on the time difference between the pump and probe.

Biological macromolecules of noncrystalline structure, like viruses, do not give Bragg diffraction images, while X-rayed. An efficient method of imaging, of an isolated delicate, structurally and mechanically, object, is registration of the distribution of the dissipated light intensity. To register an image, good and useful for object reconstruction, it is necessary to fulfill a number of technical conditions: coherent lighting with a laser beam, the pulse strong enough to give light dissipation of measurable intensity in the full space angle, the pulse short enough not to allow the molecule to denaturize during the interaction and image registration, necessary multiple registrations of the same image in the same conditions and the same object – which is very complex geometrically, to avoid the influence of accidental object orientation on single image and to enable object reconstruction in 3D. The real object image is reconstructed by software basing on the analysis and combination of multiple dissipation and diffraction images. The FLASH laser was successfully used for reconstruction of given nanometer drawings.

The FEL, as a precision tunable IR source, for photon energy range of deV, turns to a research tool of the structure of complex semiconductors. It enables the following measurements of: optical properties, relaxation dynamics, charge carrier dynamics in super-nets, absorption in quantum wells, width of emission lines, dispersion, coherent excitations of resonant effects. These energy levels are characteristic for excitations in such objects and quantum structures as: vibrons, phonons, polarons, polaritons, plasmons, binding energies of dopants, energies of discrete levels in quantum wells, dots and wires.

FEL is an effective, tunable source of THz radiation. The THz spectroscopy, as opposite to optical one, a direct measurement is possible for time dependencies of the field. It means that the amplitude and phase of the field is available for the electrical field E. There is no need to use indirect method with Kramers-Kronig relations as in optics. The THz radiation range is characteristic for vibrations of particles in liquids and many molecules, what is used for identification of chemical compounds. Phototermal spectroscopy PTBD, with usage of a pulsed FEL as a source, allows to selectively excite metal atoms containing compounds created at the surface of minerals. These

compounds are characteristic to natural environment pollution, even with very small amounts $10^{-6} \div 10^{-8}$ of heavy metals.

FEL radiating in the range of the, so called, water window, i.e. between the K absorption thresholds for C atoms ($\lambda \approx$4,4nm; E$\approx$ 284 eV) and O atoms ($\lambda \approx$ 2.3 nm; E$\approx$ 543 eV), enables building systems of imaging of biological objects in water with exceptionally good contrast. C atoms absorb, in this energy range, much stronger than O atoms.

4. EuroFEL NETWORK AND OTHER RELATIONS OF POLFEL

A coordinated development of free electron lasers in Europe was defined in the ESFRI – European Strategy Forum on Research Infrastructures document – on 11th June 2004. FELs were defined there as 'technology drivers'.

EuroFEL consortium is a network of complementary European FEL infrastructures. It is a part of ERA, accepted by ESFRI. The members of the EuroFEL, apart from the already mentioned ones E-XFEL and FLASH in DESY and POLFEL (Świerk), are: Fermi at Elettra (Turyn), Bessy FEL (Berlin), SPARX at ENEA/INFN (Frascati), 4GLS at Daresbury, Orsay FEL, Grenoble FEL, MAX-IV in MaxLab. A serious hope of the EuroFEL consortium is to build an effective, research and technical, partnership network, in the pan-European scale, according to the assumptions by ERA, in which, after some short time, the laser laboratories will be specializing and slowly transferring to units oriented to the technical and industrial users.

POLFEL is closely related to E-XFEL build in DESY, predicted for commissioning in 2013, and its predecessor FLASH. The essential solutions for these lasers base on superconducting RF TESLA technology. The main European project concerning FEL machine is E-XFEL. It is an international project. The host is DESY Hamburg. The cost of the whole E-XFEL infrastructure is estimated for 2mld €. The demonstrator of TESLA technology, serving the E-XFEL, is under preparation in DESY, since more than a decade. Initially this was TESLA Test Facility – TTF and now it is FLASH laser. The power supply for FLASH and then for E-XFEL is a superconducting electron linac. The pulsed linac in FLASH is 200m long, and generates electrons of E=1GeV energy. The E-XFEL linac will be 2km in length. FLASH generates now EM wave of $\lambda \approx$5nm. Biomedical and material engineering experiments use, effectively generated, the fifth harmonic of the fundamental wavelength. E-XFEL is expected to generate sub-nanometre wavelengths and of very high intensity, bigger than 10^{35}[Phot/s mrad^2 mm^2 0,1%BW]. Smaller FEL machines are build, tested or designed in Europe, in Italy, France, Sweden, England and Germany.

On the domestic scene, POLFEL is closely related to the Polish Consortium of European X-Ray Free Electron Laser and to the National Center of Synchrotron Radiation, under construction in Kraków.

The biggest FEL now working is FLASH in DESY, generating $\lambda_5 \approx 1{,}5$nm in the fifth harmonic and LCLS commissioned in 2009 working in SLAC. The SLAC-LCLS (Linac Coherent Light Source) laser is a sort of the American counterpart and competitor to E-XFEL. It uses 3km of classical, warm, copper cavity liniac. Out of this length, 1 km is used to inject the e^- beam into the undulator. In April 2009 the laser generated for the first time the wavelength 0,15nm. A further perspective of very high energy FEL development is the ILC experiment in Fermilab with a linac of the accumulated length around 30km. The increase in electron beam energy is now not an obstacle in FEL development, since there are constructed in Europe a few big linacs of relevant energies.

The directions of research work on FEL now are the following, and depend on the working energy range. In the range of big energies of electron beam E_e [multi-GeV], or big photon energy E[MeV], or small sub-angstrom optical wavelengths:

$$\lambda[\text{Å}] = 12.4/E[keV], \tag{5}$$

there are searched new material solutions, new constructions, designs and methods leading better undulators and higher quality of the beams. In the range of IR and THz waves there are researched compact waveguide FEL machines, especially safe ones, radiating below a so called, neutron threshold ($E \approx 10$MeV). Such FEL machines may find very numerable industrial applications.

The European and world research and technical community of FEL i quite big and well organized. It is integrated, among others, by an annual global FEL conference: 2011 open, 2010 Malmo (32 conf. in series), 2009 Liverpool, 2008 Korea, 2007 INFN, etc.

5. CONCLUSIONS AND CLOSING REMARKS

There is a number of important consequences of taking the decision to build a big FEL machine in this country. It is not only a problem of building a single research and industrial infrastructure center. This is rather a problem of general political approach and consequent, long term decisions concerning the development of innovative, high-tech industries in Poland. High-tech industries base, in practice, on a big number of small innovations, which have comparatively easy way from the idea, applied research, through the design and tests to the technical solutions. However, without big technical research centers and big enough technical potential, accumulated in industrial parks around them, it is impossible to overcome a certain critical threshold of really self generated innovativeness. The opposite solution is just to adapt and use the innovativeness of others.

Below there are gathered some relevant remarks concerning the decision of building a FEL in Poland. This decision is combined with building the National Synchro-

tron Center in Kraków and the National Center of Hadron Therapy, also in Kraków. All these undertakings use similar, accelerator based, technologies.

- Construction of a FEL laser in this country, related on the international level to EuroFEL network, and on the national level with XFEL-Poland and National Center of Synchrotron Radiation is a big chance to create advanced research and technical infrastructure of the European class.
- The conditions favoring the FEL project in this country are: relevant political atmosphere, available funds for building a FEL, there is accessible the required basic infrastructure, there are experts ready to undertake the effort of the project, there are formal institutions taking initiatives in this direction, the project is strongly embedded in international collaboration.
- POLFEL may be realized with a full usage of E-XFEL components, which has several advantages: the most modern, yet checked technology; avoiding costly and long-lasting research phase of the project; purchase of components in serial production price instead of individual; 'retrieval' of Polish experts working for FEL – mainly in Germany and USA; usage of the know-how of the whole international E-XFEL consortium.
- The conditions which do not favor realization of FEL project in this country: Poland has never had a really big research and technical project; there is a big risk of the lack of complementary character of the project and big competition with similar machine infrastructures build in Europe in such countries as: Italy, UK, Germany, France; in this country there is a strong opposition against big investments in science infrastructures.
- Building of a FEL in this country will considerably strengthen high class engineers and physicists, experts in such fields like: cryotechnology; high vacuum technology; superconductivity; high power RF circuits; precise distributed clock networks for time, frequency and phase; distributed measurement systems; advanced electronic and photonic systems; precision mechanics and microsystems, mechatronics, specialized laboratory systems;
- FEL in this country will strengthen national research in material engineering, electronics, chemistry, biology and medicine, environment protection;

- POLFEL seems to be a chance for a large part of the national research, technical and industrial communities. POLFEL may initiate a number of new advanced, hi-tech industries in this country. It is a chance not to be omitted.

REFERENCES

1. The ESFRI Roadmap [cordis.europa.eu/esfri]
2. ERA [cordis.europa.eu/era]
3. XFEL Poland Consortium; [xfel.pl]
4. POLFEL [polfel.pl]
5. E-XFEL [xfel.eu]
6. EuroFEL [eurofel.eu]
7. FLASH [flash.desy.de]
8. TESLA [tesla.desy.de]
9. POLFEL Project description, IPJ Świerk, 2008/09
10. G.Wrochna, Private Information, IPJ Świerk, 2009
11. ELETTRA [elettra.trieste.it]
12. SLAC LCLS [lcls.slac.stanford.edu]
13. Japan FEL SCSS [www-xfel.spring8.or.jp]
14. CEA FEL [iramis.cea.fr/phocea]
15. INFN FEL [www.infn.it]
16. XFEL Polska [www.xfel.pl]
17. FEL [sbfel3.ucsb.edu/www/vl_fel.html]
18. Lightsources [lightsources.org/cms]
19. JLab FEL [jlab.org/fel]
20. W. Ackerman, K. T. Poźniak, R. S. Romaniuk, (et al.): (TESLA Collaboration), Operation of a free-electron laser from the extreme ultraviolet to the water window, Nature Photonics, vol. 1, no. 6, 2007, pp. 336–342.
21. R. Romaniuk: *European work on FEL*, presentation at IXth Symposium on Laser Technology (STL), Świnoujście, Sept. 2009.

ELECTRONICS AND TELECOMMUNICATIONS QUARTERLY, 2009, 55, no 3, pp. 683–692

Development of laser technology in Poland

JERZY GAJDA[1], RYSZARD S. ROMANIUK[2]

[1] *West Pomeranian University of Technology,*
[2] *Warsaw University of Technology*
e-mail: Jerzy.Gajda@zut.edu.pl,
R.Romaniuk@ise.pw.edu.pl

Received 2009.10.08
Authorized 2009.11.09

The paper presents chosen development threads of laser technology and associated branches of optoelectronics in this country. An occasion to summarize the work and show their current status is the 50 th anniversary of construction of the first laser. The first laser in Poland was launched successfully in 1969, almost simultaneously at WAT and PW. Domestic achievements in this area are summarized every three years by Symposium on Laser Technology held traditionally in Świnoujście. The work carried on in Poland concerns technology of laser materials, construction of new lasers and associated equipment as well as laser applications. Many technical teams participate in laser oriented European structural and framework projects.

Keywords: laser technology, lasing materials, optoelectronics, laser theory, laser design, kinds of lasers, semiconductor lasers, laser applications, photonics

1. LASERS AND LASER TECHNOLOGY

Laser technology is an important practical tool, and simultaneously a driving force of development for many branches of science, technology, medicine and industry. It embraces optical and lasing material technology, laser construction and laser applications. The materials are optical, optoelectronic, passive, active, nonlinear, crystals, semiconductors, glasses, and many more. Laser construction concerns optimization of existing solutions as well as searching for novel ones. There are researched materials, components, laser devices, manufacturing technologies and measurement techniques for laser parameters. The kinds of researched lasers include: semiconductor, photonic, gas, ion, solid state, excimer, free-electron and others. Optical wave in laser technology is subject to generation, amplification, synchronization, mixing, frequency multiplication

up and down, forming into pulse shape. Applications of lasers concern such areas as: material processing, biology, industry, environment monitoring and protection, safety, etc.

This year, there is the 50 th anniversary of laser discovery. Lasing phenomenon itself was predicted a few years earlier. Laser technology has been intensely developing in this country since the sixties. The first laser was launched in Poland in 1969. The first research teams were formed at Military Academy of Technology WAT (prof. Z. Puzewicz) and at Warsaw University of Technology PW (prof. W. Woliński), as well as at the Adam Mickiewicz University in Poznań (prof. F. Kaczmarek). The domestic research and technical community of laser technology have been meeting for 25 years at the national laser symposia. These symposia are organized traditionally in Świnoujście, under the auspices of Committee of Electronics and Telecommunications, Polish Academy of Sciences (PAN), Polish Committee of Optoelectronics, Association of Polish Electrical Engineers, Photonics Society of Poland, by the West Pomeranian University of Technology (formerly Szczecin University of Technology), in cooperation with Military University of Technology and Warsaw University of Technology. The ninth symposium was organized during the last week of September 2009. The paper contains a debate on chosen topical threads presented by national laser technology centers in Kraków, Wrocław, Poznań, Warsaw, Kielce, Gliwice and others.

2. NEW LASER MATERIALS

The researched laser materials include crystals like double wolframides doped with ytterbium, wanadides doped with lanthanides and glasses, in particular glass optical fiber lasers of particular properties like high power ones. The researched materials that are pumped with a semiconductor laser, are subject to measurements of spectroscopic characteristics, in order to determine the conditions for light generation. The active cross sections for absorption of pump light and respective active cross sections for light emission are determined. There are observed relaxation processes for energy states of active ions and analysed parasitic processes. Possibilities for energy up-conversion from the IR spectrum to the visible are researched. The influence of dopant concentration on lasing characteristics is also evaluated. The work is carried in the Institute of Low Temperature and Structure Research of the Polish Academy of Sciences in Wrocław (INTiBS PAN).

Thin garnet layers are doped with transitional metal ions (Cr, Ni, Co). These ions possess broad emission spectral lines, that allow tunable generation in a wide spectrum. They are also used as sensitizers in systems doped with lanthanides. Tunable lasers based on transitional metal ions can potentially find application in amplifiers and optical generators and Q modulators of laser resonators.

Oxide crystals having stoichiometric Nd^{3+}ions, doped with Yb^{3+}ions, and illuminated with optical pump, exhibit photo-thermal phenomenon. Energy is exchanged between Nd and Yb ions. This effect can be maximized via the choice of the matrix

material and concentration of active ions. The external result of the effect is a shift of the luminescence wavelength, which may be used for optical switching. The work is carried in Institute of Electronic Materials Technology (ITME).

3. SEMICONDUCTOR LASERS

Semiconductor lasers are used as optical pumps in many devices and assemblies, as in the construction of hybrid lasers, for building of optical fiber lasers for numerable telecommunication applications. The lasers for telecommunications are strictly standardized because of costs and direct cooperation with standardized telecom oriented optical fibers. The parameters of optical pumps are as follows: single emitter, edge emitting, laser diodes, of the stripe width smaller than 100 μm, with a considerable length of the resonator, of maximum energy efficiency and high emitted power, with the biggest possible brightness or the smallest possible beam divergence. The beam divergence is critical because of small values of numerical apertures in telecom optical fibers. Semiconductor optical pumps are optimized for losses in the resonator and increase of the effective waveguide width and stabilization of the threshold current, which in turn stabilizes electrical and thermal laser parameters.

Semiconductor lasers are bipolar components with a p-n junction, directly polarized. This junction is an active region of a laser. Lasing action bases on inter-band transitions of carriers. The length of generated wave depends on kind of material and width of the energy band. Quantum cascade lasers are a new class of semiconductor unipolar components (as opposite to bipolar). Lasing is a result on intra band transitions of electrons (as opposite to inter-band ones). The active region is a multiple quantum well. The generated wavelength depends on the geometry of the quantum wells. Materials such as AlGaAs and InP give the possibility to generate waves from IR to THz. There are investigated pulse components, working with Peltier stack, for MIR. They generated 1W of optical power in 240K. The work is carried in Institute of Electron Technology in Warsaw(ITE).

Gallium nitrides GaN,InGaN, AlGaN are used to build semiconductor lasers, for the following applications, that require high optical power: writing optical information and data, printing, optical laser projectors, laser displays. To obtain high optical power, at not very big exciting current densities, and at not very high requirements for beam quality, laser matrices with multi-emitter construction are used. Individual lasers in the matrix may couple together via the optical field in the substrate, which leads to the work mode in a single transverse mode of the resonator and results in a high power emission of a very narrow spectral line. A coherence of the emitters is obtained when they are positioned close enough to each other in the matrix. The work is carried in Institute of High Pressure Physics of the Polish Academy of Sciences (IWC PAN).

4. PHOTONIC CRYSTAL LASERS

Semiconductor and glass lasers are also built of structural materials – photonic crystals. For photonic crystal optical fibers (passive and active) the matrix is glass, while for semiconductor lasers from photonic crystals the matrix is AlGaInAs/InP. Photonic crystals for lasers have several advantages for telecommunications applications like wide work area in a single mode regime (theoretically endless, non-confined), possible reduction of threshold current, possible increase in emitted optical power in the fundamental mode, narrowing of the spectral linewidth, possible increase in the rate of digital modulation.

5. OPTICAL FIBER LASERS

Fast optical fiber lasers development was due to progress in technology of ultra-low--loss active fibers with double cladding, which facilitates optical pumping, and due to spectrally and geometrically fit optical semiconductor pumps. Optical fiber lasers have different characteristics from a family of volume lasers. The lengths of active optical fiber made of glass or photonic crystal vary from a few tens of centimeters to a few tens of meters. The aggregated volume of active material is small. The transverse dimension of fundamental mode is also small, which results in critically low power levels leading immediately to nonlinear effects and then to the destruction of the structure. Now, optical fiber lasers radiate approximately 10 kW of continuous wave (CW) optical power at the beam quality factor $M^2 \approx 2$. For pulsed wave (PW) lasers, the radiated energy in a ns pulse is around 10 mJ, thus relatively not large. The work on optical fibers and fundamental confinements concerning the quality of the beam are carried out at Military Academy of Technology and Warsaw University of Technology (WUT).

Optical fiber lasers find broad applications in photovoltaics, optical fiber communications, medicine, cosmetics, material processing, welding, industry, imaging systems, and in research. Optical fiber lasers can work in single-wave and multi-wave modes, fit for optical communications WDM standard. Shaping of the multi-wave spectrum is done via a change in the mutual polarization states of the emitted and pumping signals.

Optical fiber lasers are built in a cascade geometry, the master oscillator and power amplifier configuration (MOPA). The cascade is used for pulse work mode. It is easier to control low power semiconductor or optical fiber laser starting the cascade, than a high power laser finishing the cascade. The parameters to be controlled are pulse repetition frequency, time duration and shape of the pulse and wavelength. The cascade consists of a source (semiconductor or optical fiber) and two or three optical fiber amplifiers. The first stage of the cascade is a preamplifier of very high amplification and optimized very low noise. The second stage uses optical fiber with a double cladding for maximal pumping. The third stage of the cascade is either a multimode fiber or a single mode with very large effective modal area.

6. HYBRID, ION AND GAS LASERS

This not very single meaning term 'hybrid' is used for a serial connection of two or more different lasers where the first one pumps the next one. The pump is usually an optical fiber laser (or a number of lasers), and the output beam of the hybrid cascade is generated by a volume laser. Hybrid lasers emitting in this part of the NIR spectrum which is safe for human eye, i.e. 1.4-2.2 μm are used for pulse atmospheric lidars, tuned spectrally for particular absorption lines of substances in the atmosphere like water vapor, carbon dioxide, hydrocarbons. The mentioned wavelengths are generated in matrices doped with thulium and holmium (optical fibers and crystals YLF, YAG). A tunable laser Ti:Al_2O_3 pumped with a pulsed neodymium laser may possess internal resonator conversion to the second harmonic.

There is also carried work on gas lasers: He-Xe excited by RF method and ion lasers Ar-Kr.

7. EYE SAFE LASERS

Various types of a laser equipment work with an open, free space accessible beam. These are the following applications of lasers: distance meters, goniometers, level meters, area confiners, area protection. Working with an open beam, the devices have to protect the safety of the user and accidental persons coming into the working area. The highest radiation intensity, not causing damage to human eye is in the spectral range 1.6-1.65 μm. This range is usually called a "eye safe". The radiation is totally stopped at the surface of cornea and does not penetrate deeper. Eye safe lasers embrace: glass:Nd^{3+} pumped by semiconductor laser diode, Nd lasers with Raman shifter in a form of methane gas chamber, and new solutions – optical parametric oscillators (OPO) from KTP crystal positioned inside Nd Laser, and hybrid lasers Er:YAG pumped with optical fiber laser doped with erbium. The work is carried in Military Academy of Technology (WAT).

8. TERAHERTZ LASERS

Generation of THz wave by lasers can be achieved now using two essential methods, respectively in time and frequency domains. Time domain method uses optical rectification effect, while the frequency method uses optical frequency mixing. The basic problem is construction of a laser generating a double single mode beam of tuned frequency. The biggest application perspective in this area has quantum cascade laser with external resonant cavity, which generates two tunable beams in the MIR spectral range. Increasing the wavelengths subject to generation of differential frequency by optical mixing, leads to increase of this process due to the increase of mutual coherence path. The quantum cascade lasers are built with a double amplifier and

inbuilt, in the laser structure, an optical, resonant, nonlinear component. The lasers generate and mix internally two longitudinal frequency modes in the MIR range, what as a result of mixing gives an output THz wave. The obtained beam power is now around tens of μW in the temperature of 80 K and around 1 μW in 300 K.

Terahertz photo mixer is a nonlinear photonic component, in which optical switching in optical material is performed by means of two interfering laser beams, with THz frequency. Periodic intensity of the interfering beams switches the optical key. The effect is amplified by a THz dipole resonant antenna. The generated THz beam is collimated in the material by a silica lens of high resistivity. The radiated beam out of the material (into the free space) is collimated by a polymer lens or by parabolic mirrors. The beam, after penetrating through the investigated object, is detected by a dedicated semiconductor or bolometric matrix, or by an analogous terahertz photo-mixer – excited by identical two laser beams, as in the transmitter. The photo-mixer receiver is an analog to homodyne coherent detection in the radio frequency (RF) range. One of the materials, where the photo-mixing is realized is low temperature GaAs.

9. OPTICAL MASTER CLOCKS

To measure time with high accuracy, optical and optical-atom effects are utilized. Optical atom clock, similarly to microwave cesium master oscillator, consists of three major components: atom master resonator for reference frequency, a laser tuned to the frequency of master oscillator and optical frequency comb. The atom reference clock uses cold μK, trapped, slowed down optically and magnetically strontium atoms. The expected accuracy of the optical reference clock is in the order of 10^{-18}, thus bigger than obtained in the cesium clock. The optical frequency of 300 THz is measured with accuracy of mHz. This work is carried at Jagiellonian University in Kraków (UJ).

10. LASER BASED REMOTE SENSING

Laser driven teledetection (remote sensing) is an area of double usage, in the safety and defence technology, as well as in monitoring and protection of the environment. The remote detection methods perform simultaneously data acquisition and analysis. To monitor remotely threats such as gases, aerosols, fumes, dust, there are used two methods with either a remote or a local sensor. The measurement without a contact with the polluted threat area is realized by an active or passive way. There are used lidars or multispectral thermovision. Narrow band optical filters are adjusted to the absorption ranges of expected gases or other pollutants. The measurement system estimates the changes in beam transmission along the analyzed path inside the polluted area. The measuring characteristics of the lidar depend on the range of the penetrating beam, extension of the monitored area, field of view, and the rate of beam scanning.

The measurement technique with usage of the local sensor (or a network of sensors) requires data readout by a wired or wireless method. The work is carried out in Military Academy of Technology (WAT).

11. LASER DEFENCE AND WEAPON

The European Defence Agency (EDA), under the management of Javier Solana, has turned recently to a very considerable and effective disposition center of the increased European funds in the area of safety. The logistics of the EDA projects and grants is similar to the framework FP system. WAT participates in a number of laser projects embracing laser, directed beam, weapon for destroying rackets and shells, discovery of a sniper, building of a modern helmet with passive and active sensors, building of an individual safety and protection system for a soldier, tele-detection of improvised explosives, detection of biological weapon by means of laser induced fluorescence, detection of molecularly modified polymers combined with explosive materials.

The sniper discovery system is a hybrid one, consisting of an active laser lidar to find the components of sniper aiming optics, infrared and thermo vision sub-system, miniature radar of low range and acoustic data acquisition and imaging. The system is capable of creating a composite image of the analysed scene. The methods with the creation of a composite image of a very noisy and complex scene are very efficient.

12. INTERFEROMETRIC POSITIONING

The systems of an automatic positioning of masks and inspection of semiconductor wafers, based on laser interferometry, will require, during the next decade, a resolutions better than 0.1 nm. The respective lithography will use a standard dimension in the order of a few nm. It requires intense research on stable metrological lasers, of ultra-low noises, with precise control systems, detectors and interpolation methods. The work is carried in Lasertex in cooperation with Wrocław University of Technology (PWr).

13. LASER LAYER DEPOSITION

Laser technology enables a precise deposition, by ablation or evaporation methods, of multilayer films on the surface of heavy loaded machine parts. At the total thickness of approximately 1 μm, the layer can be built of a few hundred of nanometer sub-layers (now a few tens). Interlaced thin layers of different hardness create a monolith layer of great adhesion and much more resistant to cracking. The used material systems are for example Ti/TiN, Cr/CrN, TiN/CrN, but also may consist of polymer, ceramics and metal layers mutually interlaced. There are researched and optimized mechanical

properties of such meta-material super layers for applications in the machine industry. Apart from increased mechanical ruggedness, they exhibit a property of self lubrication.

14. PHOTODYNAMIC DIAGNOSIS AND THERAPY

For diagnosis and therapy laser radiation and an active dye like porphyrine can be used. The dye is gathered via complexing reaction with the lipoproteins in pathological places. The diagnosis seeks for these places via activating illumination of the skin, body cavities or using endoscopic techniques. The therapy uses higher illumination power to release single oxygen atoms from the dye, which poison very locally the changed tissue. The method is used in dermatology, ophthalmology and other disciplines of medicine.

15. EUROPEAN INFRASTRUCTURAL LASER PROJECTS

The extremal light infrastructure (ELI) project concerns building of a system with exawatt laser generating ultrashort pulses of 10 fs, and power as high as 10^{23} W/cm^2. The laser will be used for: research of light interaction with matter, generation of high energy charged particles, generation of X-ray pulses, relativistic compression of optical pulses in order to obtain the light intensities above 10^{25} W/cm^2 and light pulse durations in the range of atto- and zepto- seconds (10^{-21} s).

The project LaserLab Europe is a research network grouping laboratories possessing infrastructures with pulse lasers of high power. The aim is to coordinate the research efforts and cost spending to obtain synergy effect. The subjects of relevance are: attosecond lasers and their applications, high power and medium energy lasers, laser acceleration of particles, lasers in medicine, femtosecond X-ray sources.

HIPER project concerns construction of the European laser infrastructure for thermonuclear fusion and extreme states of matter. The aim is to build a laser demonstrator capable of producing power from fusion of deuterium and tritium to helium, which is a highly exothermic reaction. The project is complementary to ITER which uses superconducting pulse plasma tokomak. The test system for fusion consists of two lasers: multibeam nanosecond laser of around 1 MJ energy, and picosecond laser of 100 kJ energy and 10 PW power. The laser set is supplemented by a femtosecond research laser of 1 TW power.

The E-XFEL project concerns construction of an European X-ray laser FEL. Test precursor for this machine is FLASH laser. The laser is under construction in DESY and will start operation in 2013. The shortest wavelength in the fundamental mode will be around 0.05 nm. There is predicted an efficient work of this machine at least in the fifth harmonic. The laser is powered by a 3 km superconducting electron linac of TESLA type, 1.3 GHz, with niobium resonators. The resonators work with 35 MV/m EM accelerating field.

The EuroFEL project is an European FEL infrastructures network. The network is built now around the E-XFEL project. The idea is to build a network of smaller FELs, complementary with E-XFEL. The smaller machines would create preparatory community for E-XFEL experiments. The network would multiplicate access to FELs in Europe.

PolFEL project is, from assumption a part of the EuroFEL network, devoted to building a national FEL complementary with the E-XFEL. The predicted localization of PolFEL machine is The Andrzej Soltan Institute for Nuclear Studies (IPJ) in Świerk. The work mode would be CW and PW. Machine tuning would cover THz to vacuum ultraviolet (VUV) regions.

EuLasNet is an European laser network organized inside the Eureka initiative. It gathers laser businesses in Europe. It is oriented to applications of lasers in research, industry, metrology, medicine, environment protection, protection of high cultural values. EuLasNet groups national laser networks. In Poland the relevant organization is PolLasNet.

16. CONCLUSIONS AND CLOSING REMARKS

There are around 20 bigger research teams localized in academic centers, governmental institutes and firms, which carry out research and technical work on the construction and applications of lasers. A few of these teams possess bigger research and technical potential. Most of them participate in the European infrastructural and framework projects and/or have international cooperation. The work has current character, and with the exception of only a few examples, these are local actions of relatively low budget.

The major topical areas in the laser technology, of relatively bigger funding, with the involvement of national teams are: technology of semiconductor lasers, solid state lasers and gas lasers, construction of laser components; and in the area of laser applications, these are remote sensing, safety, environment monitoring and protection, medicine and cosmetics, material processing.

The laser technology is slowly but systematically developing. Active teams enter into European networks and projects, gaining access to big laser infrastructure creating the system of ERA – European Research Area. As far, the critical threshold of building own big national laser infrastructure of European dimensions, combined with international laser centers was not overcome. It seems that the national research and technical laser community should insist on building such a large infrastructure in this country. A number of national laser centers seem to be ready to undertake this initiative and withstand the effort.

Building of a big laser infrastructure in Poland is closely combined with participation of a bigger and bigger number of Polish teams in such projects like: ELI, HIPER, E-XFEL, FLASH, ALBA and similar. One of the most interesting and promising po-

ssibilities is building of POLFEL. A modern technological park may be built around this large laser.

Large research infrastructure (here laser) fulfills a number of important global and local functions. Confining the considerations to domestic aims, one may mention: amplification of national laser centers, focusing of national and European expert power, possibility to build technological park around big infrastructure of unique character, training of young experts and specialists, and many more. Lack of such large infrastructure of European extent (and even plans for its building) clearly shows that Poland consciously surrenders in this area and resigns from ambitions to belong to the class of nations contributing to the common pool of laser research. Such an infrastructure is to be shared inside ERA system. We have nothing to share actively. The strength of positive values to possess large infrastructure is so big that it is a duty of the national laser community to keep trying to build one in this country. These efforts should be coordinated at various levels.

REFERENCES

1. Sympozjum Techniki Laserowej [http://www.stl.zut.edu.pl].
2. Sieć POLLASNET [http://www.pollasnet.org.pl].
3. Projekt POLFEL [http://www.polfel.pl].
4. Projekt FLASH [http://flash.desy.de].
5. Projekt E-XFEL [http://www.xfel.desy.de].
6. Projekt ELI [http://www.extreme-light-infrastructure.eu].
7. Projekt HIPER [http://www.hiper-laser.org].
8. IO WAT [http://www.io.wat.pl].
9. Sieć EuroFEL [http://eurofel.org].
10. Laser LCLS [http://www.slac/lcls].

POLISH ACADEMY OF SCIENCE
COMMITTEE FOR ELECTRONICS AND TELECOMMUNICATIONS

ELECTRONICS AND TELECOMMUNICATIONS QUARTERLY

CONTENTS OF VOLUME 55/2009

WARSAW 2009

ELECTRONICS AND TELECOMMUNICATIONS QUARTERLY, 2009, 55 z.1-4

CONTENTS

No 1

CONTENTS

No 2

CONTENTS

No 3

CONTENTS

No 4

THE LIST OF THE REVIWERS
ELECTRONICS AND TELECOMUNICATIONS QUARTERLY

Dr inż. ***Adam Abramowicz***
Politechnika Warszawska
Instytut Systemów Elektronicznych

Dr inż. ***Jarosław Arabas***
Politechnika Warszawska
Instytut Systemów Elektronicznych

Prof. dr hab. inż. ***Jerzy Baranowski***
Politechnika Warszawska
Instytut Systemów Elektronicznych

Dr inż. ***Andrzej Bąk***
Politechnika Warszawska
Instytut Telekomunikacji

Dr hab. inż. ***Zbigniew Bielecki***
Wojskowa Akademia Techniczna
Warszawa

Dr inż. ***Piotr Bora***
Wojskowa Akademia Techniczna
Warszawa

Dr inż. ***Michał Borecki***
Politechnika Warszawska
Instytut Mikro i Optoelektroniki

Dr inż. ***Tomasz Buczkowski***
Politechnika Warszawska
Instytut Radioelektroniki

Dr hab. inż. ***Bohdan Butkiewicz***
Politechnika Warszawska
Instytut Systemów Elektronicznych

Dr hab. inż. ***Grzegorz Ciesielski***
Politechnika Łódzka
Instytut Elektrotechniki Teoretycznej,
Metrologii i Materiałoznawstwa

Dr hab. inż. ***Witold Czarnecki***
Politechnika Warszawska
Instytut Telekomunikacji

Dr inż. ***Krzysztof Czerwiński***
Politechnika Warszawska
Instytut Radioelektroniki

Prof. nzw. dr hab. ***Andrzej Dąbrowski***
Politechnika Warszawska
Instytut Telekomunikacji

Dr inż. ***Henryk Dobrowolski***
Politechnika Warszawska
Instytut Informatyki

Prof. dr hab. inż. ***Janusz A. Dobrowolski***
Politechnika Warszawska
Instytut Systemów Elektronicznych

Dr inż. ***Jarosław Domaszewicz***
Politechnika Warszawska
Instytut Telekomunikacji

Dr inż. ***Przemysław Dymarski***
Politechnika Warszawska
Instytut Telekomunikacji

Prof. dr hab. inż. ***Jerzy Frączek***
Politechnika Śląska
Instytut Automatyki

Dr hab. inż. ***Piotr Gajewski***
Wojskowa Akademia Techniczna
Instytut Telekomunikacji

Dr inż. ***Zbigniew Gajo***
Politechnika Warszawska
Instytut Systemów Elektronicznych

Prof. dr hab. inż. ***Bogdan Galwas***
Politechnika Warszawska
Instytut Mikroelektroniki i Optoelektroniki

Mgr inż. ***Marcin Golański***
Politechnika Warszawska
Instytut Telekomunikacji

Dr hab. inż. ***Konrad Hejn***
Politechnika Warszawska
Instytut Systemów Ele3ktronicznych

Prof. dr hab. inż. ***Ewa Hermanowicz***
Politechnika Gdańska
Wydział Elektroniki i Telekomunikacji
i Informatyki

Prof. dr hab. inż. ***Ryszard Jachowicz***
Politechnika Warszawska
Instytut Systemów Elektronicznych

Dr hab. inż. ***Andrzej Jakubiak***
Politechnika Warszawska
Instytut Telekomunikacji

Prof. dr hab. inż. ***Andrzej Jakubowski***
Politechnika Warszawska
Instytut Mikroelektroniki i Optoelektroniki

Dr inż. ***Stanisław Jankowski***
Politechnika Warszawska
Instytut Systemów Elektronicznych

Dr hab. inż. ***Swietlana Januszkiewicz***
Politechnika Szczecińska
Wydział Informatyki

Dr inż. ***Jacek Jarkowski***
Politechnika Warszawska
Instytut Systemów Elektronicznych

Dr inż. ***Krzysztof Jasiński***
Politechnika Warszawska
Instytut Telekomunikacji

Prof. dr hab. inż. ***Janusz Jaworski***
Politechnika Lubelska
Katedra Automatyki

Prof. dr hab. inż. ***Wojciech Kabaciński***
Politechnika Poznańska
Instytut Elektroniki i Telekomunikacji

Prof. dr hab. inż. ***Zbigniew Kaczkowski***
Polska Akademia Nauk, Warszawa
Instytut Fizyki

Mgr inż. ***Andrzej Kalinowski***
Politechnika Warszawska
Instytut Telekomunikacji

Dr inż. ***Ryszard Kisiel***
Politechnika Warszawska
Instytut Mikroelektroniki i Optoelektroniki

Dr inż. ***Tomasz Kosiło***
Politechnika Warszawska
Instytut Radioelektroniki

Dr ***Ryszard Kossowski***
Politechnika Warszawska
Instytut Telekomunikacji

Dr inż. ***Zbigniew Kowalczyk***
Przemysłowy Instytut Telekomunikacji
Gdańsk-Wrzeszcz

Mgr inż. ***Henryk Kowalski***
Politechnika Warszawska
Instytut Informatyki

Prof. dr hab. inż. ***Andrzej Kraśniewski***
Politechnika Warszawska
Instytut Telekomunikacji

Prof. dr hab. inż. ***Jacek Kudrewicz***
Politechnika Warszawska
Instytut Systemów Elektronicznych

Prof. dr hab. inż. ***Małgorzata Kujawińska***
Politechnika Warszawska
Instytut Mikromechaniki i Fotoniki

Dr inż. ***Sławomir Kukliński***
Politechnika Warszawska
Instytut Telekomunikacji

Dr inż. ***Sławomir Kula***
Politechnika Warszawska
Instytut Telekomunikacji

Dr inż. ***Krzysztof Kulpa***
Politechnika Warszawska
Instytut Systemów Elektronicznych

Prof. dr hab. inż. ***Zygmunt Kuśmierek***
Politechnika Łódzka
Instytut Elektroniki Teoretycznej,
Metrologii i Materiałoznawstwa

Dr hab. inż. ***Wiesław Kuźmicz***
Politechnika Warszawska
Instytut Mikroelektroniki i Optolelektroniki

Prof. dr hab. inż. ***Juliusz Lech Kulikowski***
Polska Akademia Nauk, Warszawa
Instytut Biocybernetyki i Inżynierii
Biomedycznej

Prof. dr hab. inż. ***Zygmunt Kuśmierek***
Politechnika Łódzka
Instytut Elektroniki Teoretycznej,
Meteorologii i Materiałoznawstwa

Dr inż. ***Lech Lewandowski***
Politechnika Warszawska
Instytut Systemów Elektronicznych

Prof. dr hab. inż. ***Tadeusz Łuba***
Politechnika Warszawska
Instytut Telekomunikacji

Mgr inż. ***Grzegorz Mazur***
Politechnika Warszawska
Instytut Informatyki

Prof. dr hab. inż. ***Marian Miłek***
Politechnika Zielonogórska
Instytut Metrologii Elektrycznej

Prof. dr hab. inż. ***Józef Modelski***
Politechnika Warszawska
Instytut Radioelektroniki

Prof. dr hab. inż. ***Tadeusz Morawski***
Politechnika Warszawska
Instytut Radioelektroniki

Prof. dr hab. inż. ***Jan Mulawka***
Politechnika Warszawska
Instytut Systemów Elektronicznych

Prof. dr hab. inż. ***Andrzej Napieralski***
Politechnika Łódzka
Katedra Mikroelektroniki
i Technik Informatycznych

Dr inż. ***Leszek Opalski***
Politechnika Warszawska
Instytut Systemów Elektronicznych

Dr inż. ***Andrzej Pacut***
Politechnika Warszawska
Instytut Automatyki

Prof. dr ***Wincenty Pajewski***
Polska Akademia Nauk, Warszawa
Instytut Podstawowych Problemów Techniki

Dr hab. inż. ***Zdzisław Papir***
Akademia Górniczo-Hutnicza, Kraków
Katedra Telekomunikacji

Dr inż. ***Andrzej Paszkiewicz***
Instytut Telekomunikacji

Dr hab. inż. ***Jan Petykiewicz***
Politechnika Warszawska
Politechnika Warszawska
Instytut Fizyki

Prof. dr hab. inż. ***Andrzej Pfitzner***
Politechnika Warszawska
Instytut Mikroelektroniki i Optoelektroniki

Prof. dr hab. inż. ***Stanisław J. Piestrach***
Politechnika Wrocławska
Instytut Cybernetyki Technicznej

Prof. dr hab. inż. ***Marian Piekarski***
Politechnika Wrocławska
Instytut Telekomunikacji i Akustyki

Prof. dr hab. inż. ***Anna Piotrowska***
Instytut Technologii Elektronicznej
Warszawa

Prof. dr hab. inż. ***Kazimierz J. Pluciński***
Wojskowa Akademia Techniczna
Instytut Podstaw Elektroniki, Warszawa

Prof. dr hab. ***Włodzimierz Pogribny***
Akademia Techniczno-Rolnicza
Instytut Telekomunikacji, Bydgoszcz

Dr inż. ***Artur Przelaskowski***
Politechnika Warszawska
Instytut Radioelektroniki

Dr inż. ***Mariusz Rawski***
Politechnika Warszawska
Instytut Telekomunikacji

Dr inż. ***Mirosław Rajewski***
Politechnika Gdańska
Instytut Systemów Informacyjnych

Prof. nadzw. dr hab. ***Stanisław Rosłaniec***
Politechnika Warszawska
Instytut Radioelektroniki

Dr hab. ***Krzysztof Sacha***
Politechnika Warszawska
Instytut Automatyki i Informacji Stosowanej

Prof. dr hab. inż. ***Jerzy Siuzdak***
Politechnika Warszawska
Instytut Telekomunikacji

Prof. nadzw. dr hab. ***Władysław Skarbek***
Politechnika Warszawska
Instytut Radioelektroniki

Dr inż. ***Andrzej Skorupski***
Politechnika Warszawska
Instytut Informatyki

Mgr inż. ***Krzysztof Skowroński***
Politechnika Warszawska
Instytut Systemów Elektronicznych

Prof. zw. dr hab. ***Wojciech Sobczak***
Politechnika Gdańska
Katedra Systemów Informacyjnych

Prof. dr hab. inż. ***Waldemar Soluch***
Instytut Technologii Materiałów
Elektronicznych, Warszawa

Prof. dr hab. inż. ***Marek Stabrowski***
Politechnika Warszawska
Instytut Elektrotechniki Teoretycznej
i Miernictwa Elektrycznego

Dr hab. inż. ***Witold J. Stepowicz***
Politechnika Gdańska
Wydział Elektroniki, Telekomunikacji
i Informatyki

Prof. dr hab. inż. ***Jerzy Szabatin***
Politechnika Warszawska
Instytut Systemów Elektronicznych

Prof. dr hab. inż. ***Paweł Szczepański***
Politechnika Warszawska
Instytut Mikroelektroniki i Optoelektroniki

Dr hab. ***Jan Szmidt***
Politechnika Warszawska
Instytut Mikroelektroniki i Optoelektroniki

Prof. dr hab. inż. ***Mieczysław Szustakowski***
Wojskowa Akademia Nauk
Instytut Optoelektroniki, Warszawa

Dr inż. ***Jacek Szymanowski***
Politechnika Warszawska
Instytut Automatyki i Informatyki
Stosowanej

Dr inż. ***Lech Śliwa***
Politechnika Warszawska
Instytut Systemów Elektronicznych

Dr inż. ***Marek Średniawa***
Politechnika Warszawska
Instytut Telekomunikacji

Prof. dr hab. inż. ***Leszek Trybus***
Politechnika Rzeszowska
Katedra Automatyki i Informatyki

Prof. dr hab. inż. ***Aleksander Urbaś***
Politechnika Wrocławska
Instytut Telekomunikacji i Akustyki

Prof. dr hab. inż. ***Krzysztof W. Wawryn***
Politechnika Koszalińska
Katedra Teorii Obwodów
i Układów Elektronicznych

Mgr inż. ***Krzysztof Włostowski***
Politechnika Warszawska
Instytut Telekomunikacji

Dr ***Piotr Witoński***
Politechnika Warszawska
Instytut Mikroelektroniki i Optoelektroniki

Płk. dr hab. inż. ***Marian Tadeusz Wnuk***
Wojskowa Akademia Techniczna
Instytut Telekomunikacji, Warszawa

Prof. dr hab. inż. ***Jacek Wojciechowski***
Politechnika Warszawska
Instytut Systemów Elektronicznych

Prof. nzw. Dr hab. inż. ***Andrzej Wojtkiewicz***
Politechnika Warszawska
Instytut Systemów Elektronicznych

Prof. dr hab. inż. ***Waldemar Wójcik***
Politechnika Lubelska
Katedra Elektroniki

Dr hab. inż. ***Zygmunt Wróbel***
Uniwersytet Śląski
Instytut Problemów Techniki

Prof. dr hab. inż. ***Janusz Zarębski***
Akademia Morska
Katedra Radioelektroniki Morskiej, Gdynia